UNIVERSITY OF SOUTHAMPTON

FACULTY OF ENGINEERING AND APPLIED SCIENCE

DEPARTMENT OF ELECTRONICS AND COMPUTER SCIENCE

NOVEL OPTICAL FIBRE DEVICES BASED ON THE MCVD METHOD

by

Liang Dong

A thesis submitted for the degree of
Doctor of Philosophy

January 1992

Acknowledgement

I would like to thank my supervisor professor W.A. Gambling and professor D.N. Payne for the guidance that they gave in the process of my PhD course. I am also indebted to Dr. P.St.J Russell for his many valuable discussions in the process of this lengthy, tiresome, and, sometimes, exciting (very limited occasions) experience, and for his guidance in the preparation of the thesis. My thanks also go to Drs. J. Pinkstone, G. Wylangowski, P.J. Wells, D.P. Hand, L.Poyntz-Wright, J.E. Townsend, and S.B. Poole. A complete list would be endless. Without their help and encouragement, I can not imagine that I would have been able to go through this PhD course. I would also like to take this opportunity to thank many other people who I have not named but who made my PhD life sufferable. Finally, I would like to express my gratitude to my parents, who have almost suffered the loss of a son in the last four years.

Content

UNIVERSITY OF SOUTHAMPTON

ABSTRACT

FACULTY OF ENGINEERING AND APPLIED SCIENCE

ELECTRONIC AND COMPUTER SCIENCE

Doctor of Philosophy

Novel Optical Fibre Devices Based on the MCVD Method

by Liang Dong

In this thesis, several new optical fibre devices are described. These devices are based on fibres with special structures or materials, fabricated by the MCVD technique.

Light propagation and intermodal coupling in twin-core (TC) fibres are investigated both theoretically and experimentally. A cascaded TC fibre filter is demonstrated and so are TC fibre intermodal couplers using both mechanical gratings and fibre acoustic flexural waves, which can be used as filters, wavelength-division-multiplexing (WDM) taps and frequency shifters.

Photosensitivity in both transition-metal-doped fibre and cerium-doped fibre with applications for making fibre in-core gratings are also studied. UV-induced absorption and refractive index change are investigated. A large absorption change occurs when fibre is exposed to pulsed UV. The fibre IR loss eventually recovers to its original level. The UV-induced refractive index change in cerium fibre is found to be the same order of magnitude as that reported in germanosilicate fibres.

Some other devices and effects, including a gold-implanted fibre polariser, excitation poling in second harmonic generation and a spatial model converter, are also studied. The gold-implanted polariser is much easier to be mass-produced and spliced to an ordinary fibre with a low loss than its liquid-metal-implanted counterpart. Excitation poling gives an improved efficiency in second harmonic generation. The spatial model converter provides an easy low-loss connection for waveguides with different spatial modes.

Chapter One Introduction

1.1 General introduction

Optical fibre is still a growing technology. It is only twenty-five years since Kao and Hockham's first proposal for using dielectric fibre waveguides for transmitting optical pulses over long distances[1]. It took about ten years for the first optical fibre system to appear[2,3], and now optical fibre systems are widely used for long-haul telecommunications. The coming of wide-band local optical fibre networks is also inevitable. The loss of a single-mode fibre can be as low as 0.2dB/km. The last decade also saw the rapid appearance of optical fibre amplifiers, first demonstrated in Southampton[4], providing an optical means for regenerating optical signals for telecommunications over long distances. Optical amplifiers, together with the newly developed soliton technology (which utilises nonlinear effects to compensate the pulse dispersion caused by the material and the waveguide), have made up an optical fibre system able to transmit light pulses over 12,000km at 2.4Gbit/s[5]. This is bound to have an impact on telecommunications.

Apart from telecommunications, optical fibres have also been used in sensors in many areas. Optical fibre gyroscopes have reached a very high standard[6,7]. Optical fibre temperature sensors are capable of monitoring distribution of temperature over a long distance with a single optical fibre[8]. Optical fibre sensors can also measure magnetic field to a very high accuracy[9].

With the fast development in optical fibres, there is a need for a total optical fibre system, a system without electronic devices to slow it down and narrow its bandwidth, and a system without bulk optical devices, so that it can become rigid, compact, cheaper and more efficient. Optical fibre devices such as modulators, filters, switches, frequency shifters and optical sources are thus required. These devices will be able to generate, process, and combine and separate optical signals, and are therefore vital to achieve a fully optical fibre system. In this thesis, we will discuss some of these optical devices made from novel optical fibres.

1.2 Thesis summary

Chapter two describes the theory of twin-core (TC) fibres, which have the potential for devices such as switches, filters, and frequency shifters. TC fibres are analyzed using coupled-mode theory. Periodically-perturbed-nonidentical-core TC fibre is investigated theoretically by the perturbation method. Light propagation in TC fibres with gain in one core, is derived also by the perturbation method. At end of the chapter, measurement of coupling in identical-core TC fibres are compared with predications of the theory.

Chapter three describes photorefractive effects in optical fibres. These fibres have been used to make in-core fibre gratings, which can be used as filters in optical communication systems and reflectors in narrow-band optical fibre lasers. Investigations into the effect of blue light on transition-metal-doped optical fibres, the possibility of iron-doped fibre as a saturable absorber in a fibre laser, and photosensitivity in cerium-doped optical fibres are also described.

Chapter four describes the fabrication of various novel optical fibres. Three different fibre types are discussed: liquid-metal-implanted fibres for fibre modulators and excitation poling during second harmonic generation; gold-implanted optical fibre for fibre polarisers; and double waveguide optical fibre for cladding pumping optical fibre lasers.

Chapter five discusses intermodal coupling in non-identical-core TC fibres with mechanical gratings and fibre flexural acoustic waves. This phenomenon can be used in filtering, modulation, and shifting optical frequencies. Intermodal coupling is investigated experimentally in both cases and results are compared with theoretical predications.

Chapter six describes a cascaded-TC-fibre filter, and a gold-implanted fibre polariser. Excitation poling during second harmonic generation is also discussed, and, finally, a spatial mode converter is described.

Chapter seven summarises the thesis and gives a description of possible future work in these optical fibre devices.

References

1 K.C. Kao and G.A. Hockham: "Dielectric-fibre surface waveguide for optical frequencies", Proceedings of the IEE, **133**, (7), 1966, pp.1151-1158.

2 J.E. Midwinter and J.R. Stern: "Propagation studies of 40km of graded-index fibre installed in cable in an operational duct route", IEEE Transactions on Communications, **com-26**, (7), 1978, pp.1015-1020.

3 R.W Bery, D.J. Brace and I.A. Ravenscroft: "Optical fibre system trials at 8Mbit/s and 140Mbit/s", IEEE Transactions on communications, **com-26**, (7), 1978, pp.1020-1027.

4 D.N. Payne, L. Reekie, R.J. Mears, S.B. Poole, I.M. Jauncey, J.T. Lin: "Rare-earth doped single-mode fibre lasers, amplifiers and devices", Technical Digest of CLEO/IQEL, 1986, SanFrancisco, USA.

5 L.F. Mollenauer, B.M. Nyman, M.J. Neubelt, G. Raybon and S.G. Evangelides: "Demonstration of soliton transmission at 2.4Gbit/s over 12,000km", Electronic Letters, **27**, 1991, pp.178-199.

6 R.A. Bergh, H.C. Leferere and H.J. Shaw: "All-single-mode-fibre-optic gyroscope" Optics Letters, **16**, 1981, pp.198-200.

7 K. Bohm, P. Martin, K. Petermann, E. Weidel, and R. Ulrich: "Low-drift fibre gyro using a superluminiscent diode", Electronic Letters, **17**, 1981, pp.352-353.

8 M.C Farries, M.E. Fermann, R.I. Laming, S.B. Poole, D.N. Payne and A.P. Leach: "Distributed temperature sensor using Nd^{3+} doped optical fibre", Electronic Letters, **22**, 1986, pp.418-419.

9 S.C. Rashleigh: "Magnetic field sensing with a single mode fibre", Optics Letters, **6**, 1981, pp.19-21.

Chapter Two Twin-core Fibres

2.1 Introduction

Twin-core (TC) fibres have two parallel cores embedded in a common cladding. The two cores can be identical, have a difference in radii or refractive indices, or be made of different material, with a separation varying from few core radii to tens of core radii. There are two fundamental modes at each polarisation in such a waveguide and they can be easily perturbed by introducing a small optical difference between the two cores. The fibre also has a wavelength-dependent coupling characteristic and the advantage of being a four port device, in which lights of different properties can be separated spatially. The unique properties of TC fibres has attracted many researchers for their applications in optical fibre switches, filters, frequency shifters, modulators, interferometers and sensors[1,2,3,4,5,6,7,8]. They are also very important in understanding fundamental physics of modal coupling in optics.

In this chapter, the theories for analyzing TC fibres such as identical-core TC fibres, nearly-identical-core TC fibres, periodically-perturbed TC fibres and doped-TC fibres are introduced. The design and fabrication of TC fibres are outlined, and characterisation of TC fibres described.

2.2 Theoretical analysis of TC fibres

2.2.1 Coupled-mode theory

To obtain an analytical solution for the fields in a TC fibre, some approximations have to be made to simplify the problem. A TC fibre can be treated as one core being perturbed by the presence of the other one. The combined structure supports a set of modes which are, in general, not a linear combination of the modes of the isolated cores[9,10]. However, in a TC fibre with sufficient large core-to-core separation, the modes of the TC fibre can be described by the superposition of modes in the isolated cores with a good accuracy[11,12]. This way of using superposition of unperturbed modes to simulate the true modes of a structure is commonly referred as the coupled-mode theory.

If we define E_{pm} as the fields of the m-th mode in a set of bound and radiation modes of the isolated core p (p=1,2), the field in the TC fibre can be written as

$$E = \sum_{p=1,2} \sum_{m=-\infty}^{m=\infty} V_{pm}(z)\, E_{pm} \tag{1}$$

If the field expansion for a TC fibre is substituted into Maxwell's equations, an infinite set of first order differential equations is acquired for the axially varying amplitude, V_{pm}, of each mode, in the case that modal amplitude is slowly varying. This set of equations forms the coupled-mode equations which describe the distribution of the field among the modes of the two isolated cores. However, a simple solution of the coupled-mode equations can be found when two modes are involved. For the fundamental modes in a TC fibre, this requires that the TC fibre modal field can be well approximated by a superposition of the fundamental modes in the two isolated cores, i.e.

$$E = V_1(z)\, E_{10} + V_2(z)\, E_{20} \tag{2}$$

This is only the case when the two cores are well separated (core separation is at least three times the core radius).

2.2.2 Coupled-mode equations

Light coupling in a TC fibre has been dealt with theoretically by various authors using coupled-mode theory[13,14,15,16,17]. A superposition of the isolated fibre modes is used to replace the real modes in the TC fibre in Maxwell's equations. Coupled-mode equations which determine the amplitudes of different modes in the superposition can then be derived from Maxwell's equations.

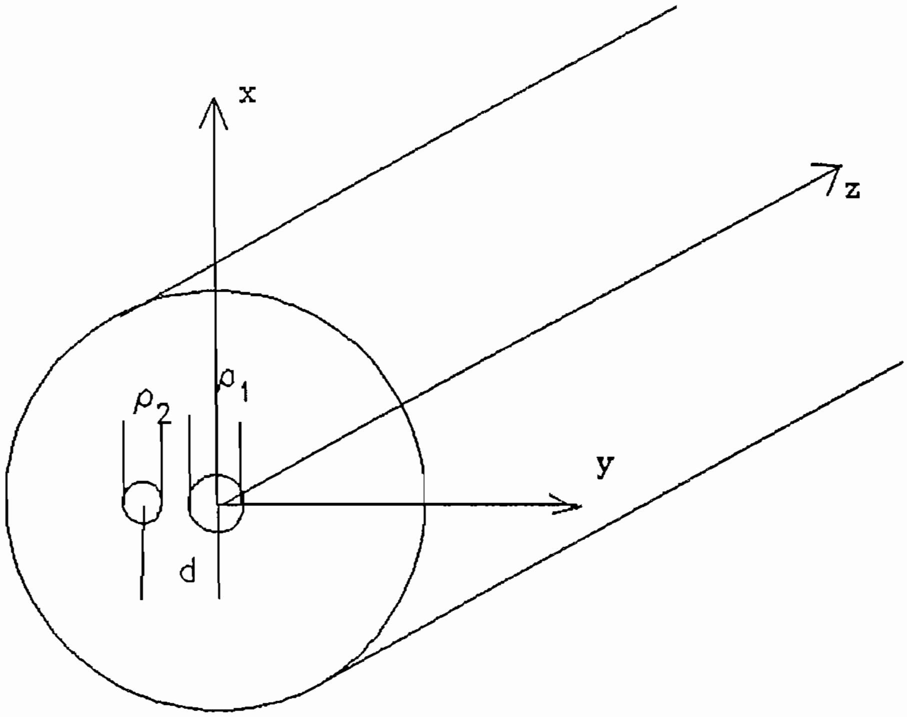

Figure 2.1 Parameters and configuration for TC fibre analysis

In this chapter, a slightly different approach has been taken to derive the coupled-mode equations. The relation among various modal overlap integral has been followed up, thus a better physical understanding can be achieved. This derivation will be limited to weakly guiding fibres with sufficiently large core-to-core separation and to fundamental modes of the TC fibres. Fibres are assumed to have step-index profiles with cladding index matched to that of silica glass. For convenience, we also limit our discussion to modes with x polarisation. The orientation of the chosen coordination and definitions of parameters for the analysis are shown in figure 2.1.

The field of the fundamental modes in the two isolated cores can be described as

$$E_{p0} = a_p(x,y)\, e^{j\beta_p z} \tag{3}$$

where a_p and β_p are the transverse field distribution and propagation constant for core p (=0,1) respectively. They satisfy Maxwell's equation, therefore

$$[\nabla^2 + (n_{cl}k)^2(1+2\Delta_p(x,y))]\, E_{p0} = 0 \tag{4}$$

where n_{cl} is cladding refractive index and k is vacuum wave number. $\Delta_p(x,y)$ is defined as the relative index difference profile of the isolated core p, i.e. $\Delta_p(x,y)=(n_{cop}(x,y)-n_{cl})/n_{cl}$ over core p and $\Delta_p(x,y)=0$ elsewhere (n_{cop} is refractive index of core p). Δ_p is very small in weakly guided fibres and Δ_p^2 term is therefore neglected.

In a TC fibre with cores well separated, the field is approximated by equation 2.2 and it satisfies Maxwell's equation.

$$[\nabla^2 + (n_{cl}k)^2(1+2\Delta(x,y))]\,(V_1E_{10}+V_2E_{20}) = 0 \tag{5}$$

In equation 2.5, $\Delta(x,y)$ is relative index difference profile of the TC fibre, i.e. $\Delta(x,y)=(n_{co1}-n_{cl})/n_{cl}$ over core 1, $\Delta(x,y)=(n_{co2}-n_{cl})/n_{cl}$ over core 2 and $\Delta=0$ elsewhere. From equations 2.2 and 2.5, we obtain (see Appendix A).

$$\frac{dV_1}{dz}+\kappa_{12}^{(2)}e^{j(\beta_2-\beta_1)z}\frac{dV_2}{dz}-j\kappa_{11}V_1-j\kappa_{12}e^{j(\beta_2-\beta_1)z}V_2=0 \tag{6}$$

$$\frac{dV_2}{dz}+\kappa_{21}^{(2)}e^{j(\beta_1-\beta_2)z}\frac{dV_1}{dz}-j\kappa_{21}e^{j(\beta_1-\beta_2)z}V_1-j\kappa_{22}V_2=0 \tag{7}$$

where

$$\kappa_{11}=\frac{(n_{cl}k)^2}{\beta_1}\frac{\int_{A\infty}\Delta_2 a_1 a_1 dA}{\int_{A\infty}a_1 a_1 dA} \tag{8}$$

$$\kappa_{12}=\frac{(n_{cl}k)^2}{\beta_1}\frac{\int_{A\infty}\Delta_1 a_1 a_2 dA}{\int_{A\infty}a_1 a_1 dA} \tag{9}$$

$$\kappa_{12}^{(2)}=\frac{\beta_2}{\beta_1}\frac{\int_{A\infty}a_1 a_2 dA}{\int_{A\infty}a_1 a_1 dA} \tag{10}$$

$$\kappa_{22}=\frac{(n_{cl}k)^2}{\beta_2}\frac{\int_{A\infty}\Delta_1 a_2 a_2 dA}{\int_{A\infty}a_2 a_2 dA} \tag{11}$$

$$\kappa_{21}=\frac{(n_{cl}k)^2}{\beta_2}\frac{\int_{A\infty}\Delta_2 a_1 a_2 dA}{\int_{A\infty}a_2 a_2 dA} \tag{12}$$

$$\kappa_{21}^{(2)}=\frac{\beta_1}{\beta_2}\frac{\int_{A\infty}a_1 a_2 dA}{\int_{A\infty}a_2 a_2 dA} \tag{13}$$

where A∞ is cross-section of the fibre. $\kappa_{12}^{(2)}$ and $\kappa_{21}^{(2)}$ are the second-order coupling coefficients and are very small comparing with the rest of the coefficients in equations 2.6 and 2.7. They are neglected in the following analysis. Since the cores are well separated, a_p (p=1,2) is small over the other core. The self-coupling coefficients, κ_{11} and κ_{22}, are therefore negligible comparing with the cross-coupling coefficients, κ_{12} and κ_{21}. Hence equations 2.6 and 2.7 can be simplified as

$$\frac{dV_1}{dz} - j\kappa_{12} e^{j(\beta_2-\beta_1)z} V_2 = 0 \tag{14}$$

$$\frac{dV_2}{dz} - j\kappa_{21} e^{j(\beta_1-\beta_2)z} V_1 = 0 \tag{15}$$

2.2.3 Identical-core TC fibres

In an identical-core TC fibre, the symmetrical structure makes

$$\kappa_{12} = \kappa_{21} = \kappa_a \tag{16}$$

$$\beta_1 = \beta_2 = \beta_a \tag{17}$$

V_1 and V_2 can be readily solved from equations 2.14 and 2.15, we have

$$V_1 = Ae^{-j\kappa_a z} + Be^{j\kappa_a z} \tag{18}$$

$$V_2 = -Ae^{-j\kappa_a z} + Be^{j\kappa_a z} \tag{19}$$

where A and B are constants determined by initial modal amplitude distribution. The field in the TC fibre can be obtained from equations 2.2 and 2.3.

$$\begin{aligned} E = {} & A(a_1(x,y) - a_2(x,y))\, e^{j(\beta_a-\kappa_a)z} \\ & + B(a_1(x,y) + a_2(x,y))\, e^{j(\beta_a+\kappa_a)z} \end{aligned} \tag{20}$$

The two fundamental modes of the TC fibre can be identified as in equations 2.21 and 2.22.

$$E_{even} = (a_1(x,y) + a_2(x,y))\, e^{j(\beta_z+\kappa_a)z} \tag{21}$$

$$E_{odd} = (a_1(x,y) - a_2(x,y))\, e^{j(\beta_z-\kappa_a)z} \tag{22}$$

$a_1(x,y)$ and $a_2(x,y)$ have the same distribution profile over core 1 and core 2 respectively. The first mode thus has a symmetrical distribution over the two cores of the TC fibre and is referred as an even mode. The second mode has the same field strength distribution over the two cores, but opposite phases and is referred as an odd mode. Also can noted in equations 2.21 and 2.22 is that the propagation constants differ by $2\kappa_a$ between the two modes. A plot of the field distribution of the two modes is given in figure 2.2.

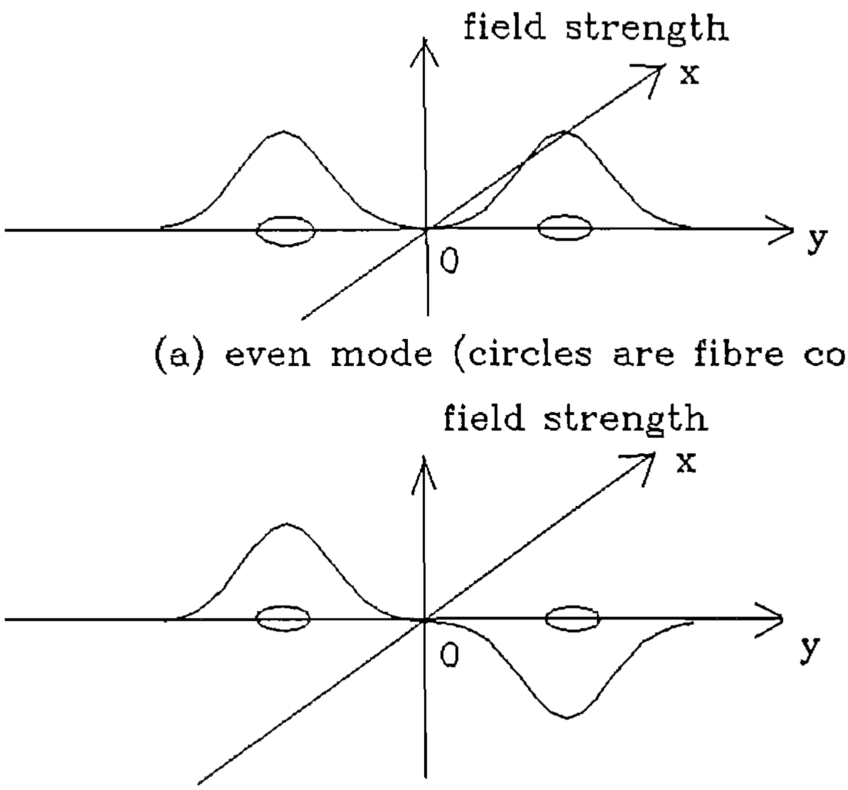

(a) even mode (circles are fibre cores)

(b) odd mode

Figure 2.2 Fundamental modes in an identical TC fibre

Equation 2.20 can also be written as

$$E = (Ae^{-j\kappa_a z} + Be^{j\kappa_a z})\, a_1(x,y)\, e^{j\beta_a z} + (-Ae^{-j\kappa_a z} + Be^{j\kappa_a z})\, a_2(x,y)\, e^{j\beta_a z} \qquad (23)$$

If the cores are well separated, $a_1(x,y)$ and $a_2(x,y)$ are small over the other core. Therefore the first and second terms in the equation 2.23 give the field in core 1 and 2 respectively. This approximation breaks up in the case of TC fibres with a small core separation (core separation smaller than 3 times the average core radius). The fields in the two cores can be described as

$$E_1 = b_1(z)\, a_1(x,y) \qquad (24)$$

$$E_2 = b_2(z)\, a_2(x,y) \qquad (25)$$

In the case of unit power launched into core 1, i.e. $b_1(0)=1$ and $b_2(0)=0$, we get A=B=1/2 from equation 2.20. We therefore have

$$b_1(z) = \cos(\kappa_a z)\, e^{j\beta_a z} \qquad (26)$$

$$b_2(z) = j\sin(\kappa_a z)\, e^{j\beta_a z} \qquad (27)$$

The power in the two cores can be calculated to be

$$p_1(z) = |b_1(z)|^2 = \cos^2(\kappa_a z) \qquad (28)$$

$$p_2(z) = |b_2(z)|^2 = \sin^2(\kappa_a z) \qquad (29)$$

Hence the power in the composite waveguide oscillates from one core to another, and a fibre length, z_b, is taken for power to complete an oscillation cycle. z_b is defined as the beat length of the identical-core TC fibre, and $z_b=\pi/\kappa_a$. The power in the two cores of an identical-core TC fibre, when unit power is launched into core 1, is plotted in figure 2.3. A coupling length is also defined in a TC fibre, $z_c=z_b/2$.

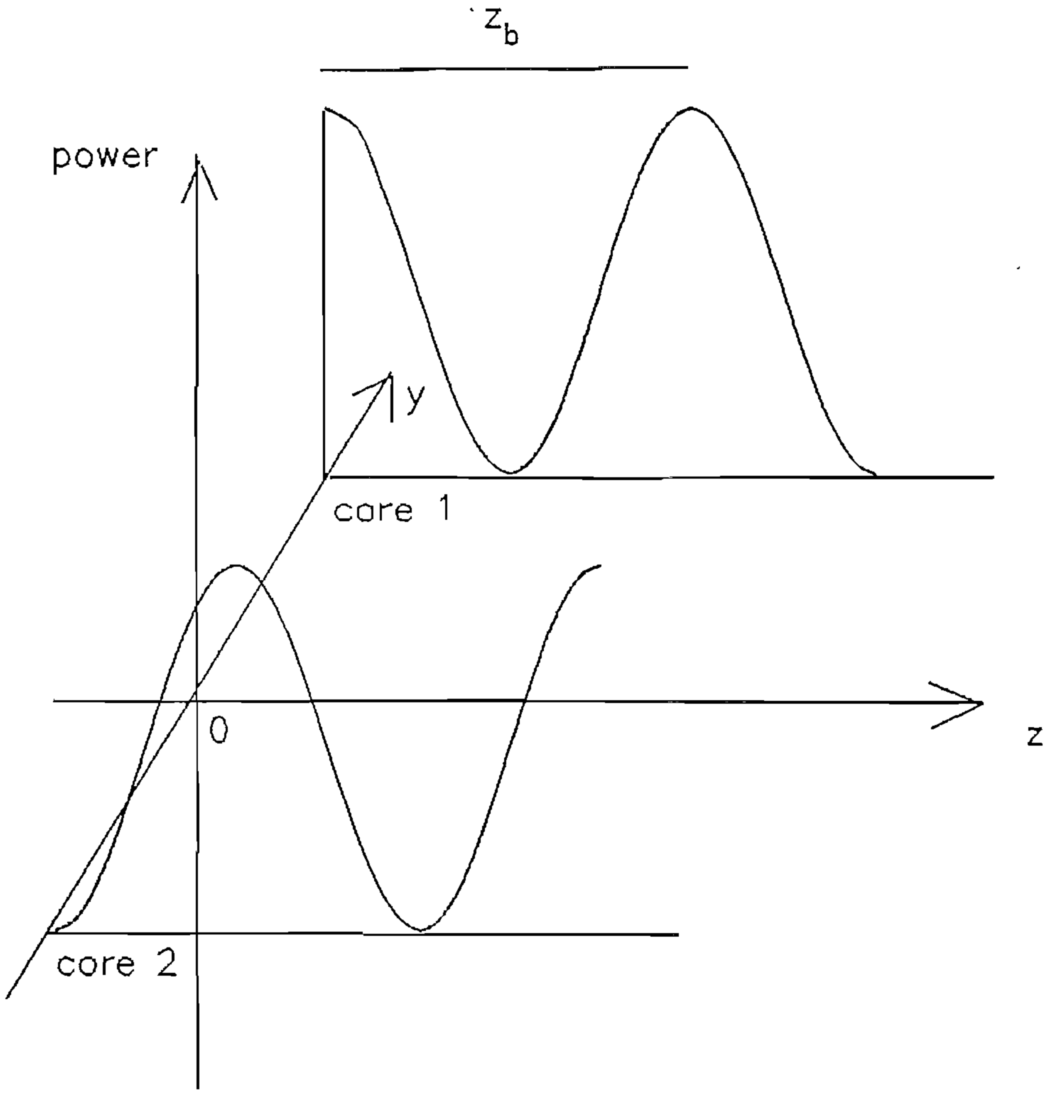

Figure 2.3 Power coupling in an identical TC fibre

For a step-index profile identical-core TC fibre, a_1 and a_2 can be solved analytically from Maxwell's equations and an analytical form for coupling coefficient can be obtained from equations 2.9, 2.12 and 2.16[11].

$$\kappa_a = \frac{\sqrt{2\Delta}}{\rho} \frac{U^2}{V^3} \frac{K_0(Wd/\rho)}{K_1^2(W)} \tag{30}$$

where Δ is relative refractive index difference and ρ is core radius. K_0 and K_1 are modified Bessel functions of the second kind. V, U and W are as normally defined in a fibre. In identical-core TC fibres, normalised coupling coefficient are plotted in figure 2.4 against V value for

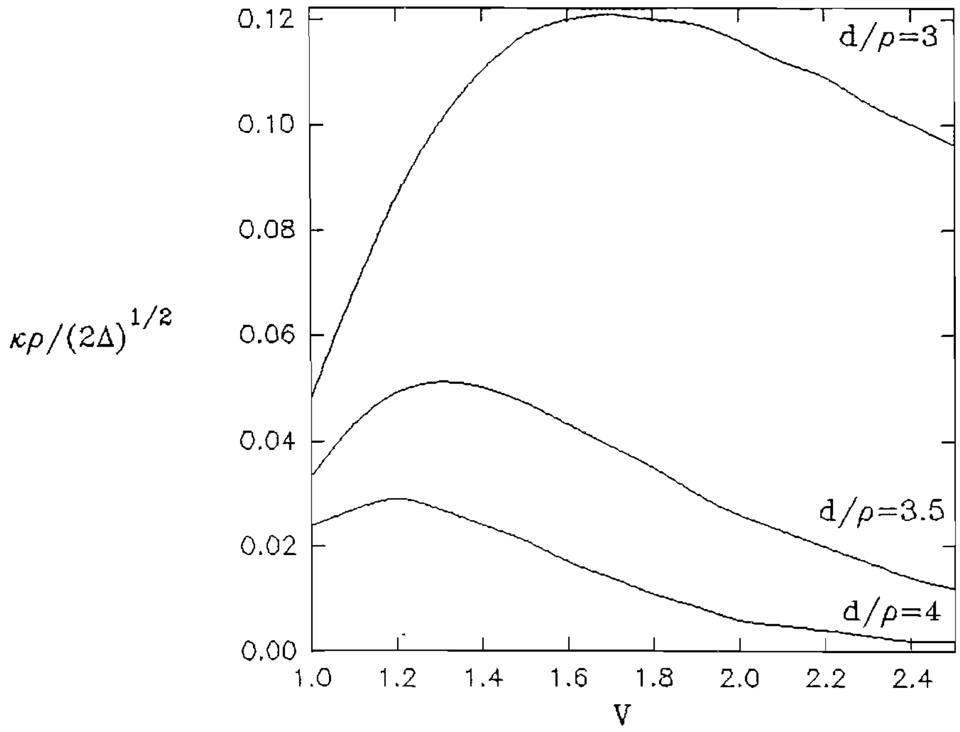

Figure 2.4 Normalized coupling coefficient in an identical-core TC fibre against V value

various core separations. It can be seen that coupling coefficient decreases dramatically when the core separation increases from three times the core radius to 4 times the core radius. It can also be seen that the coupling coefficient reaches a maximum at a certain V value. This is due to the fact that, when the V value gets smaller, the modal fields spread out so that the field strength of one core over the other core increases, but in the meantime, the field strength over its own core decreases. When the first factor dominates, the overlap integral of the modal fields of the two cores, which determines the coupling coefficient, grows and so does the coupling coefficient. When the second factor starts to dominate, the overlap integral begin to decrease and the coupling coefficient decreases too.

2.2.4 Nearly-identical-core TC fibres

In a non-identical-core TC fibre, equations 2.14 and 2.15 can be solved to give

$$V_1 = Ae^{j(\beta_2-\beta_1-\sqrt{(\beta_1-\beta_2)^2+4\kappa_{12}\kappa_{21}})\frac{z}{2}}+Be^{j(\beta_2-\beta_1+\sqrt{(\beta_1-\beta_2)^2+4\kappa_{12}\kappa_{21}})\frac{z}{2}} \quad (31)$$

$$V_2 = \frac{A}{2\kappa_{12}}(\beta_1-\beta_2-\sqrt{(\beta_1-\beta_2)^2+4\kappa_{12}\kappa_{21}})\,e^{j(\beta_1-\beta_2-\sqrt{(\beta_1-\beta_2)^2+4\kappa_{12}\kappa_{21}})\frac{z}{2}}+ \frac{B}{2\kappa_{12}}(\beta_1-\beta_2+\sqrt{(\beta_1-\beta_2)^2+4\kappa_{12}\kappa_{21}})\,e^{j(\beta_1-\beta_2+\sqrt{(\beta_1-\beta_2)^2+4\kappa_{12}\kappa_{21}})\frac{z}{2}} \quad (32)$$

Following the same vein as in the last section, we have

$$E = A(a_1-a_2\frac{\beta_b+\frac{\kappa_a}{F}}{\kappa_{12}})\,e^{j(\beta_a-\frac{\kappa_a}{F})z}+B(a_2+a_1\frac{\beta_b+\frac{\kappa_a}{F}}{\kappa_{21}})\,e^{j(\beta_a+\frac{\kappa_a}{F})z} \quad (33)$$

where

$$\beta_a = \frac{\beta_1+\beta_2}{2} \quad (34)$$

$$\beta_b = \frac{\beta_2-\beta_1}{2} \quad (35)$$

$$\kappa_a = \sqrt{\kappa_{12}\kappa_{21}} \quad (36)$$

$$F = \frac{1}{\sqrt{1+\frac{(\beta_1-\beta_2)^2}{4\kappa_a^2}}} \quad (37)$$

The two fundamental modes of a TC fibre, odd and even modes, are represented by the first and second term in equation 2.33 respectively. Over the two cores, the amplitude distribution has the same sign for the even mode but changes sign for the odd mode; however, the modal

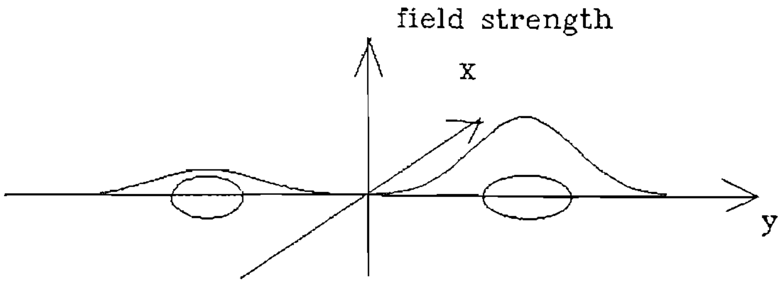

(a) even mode

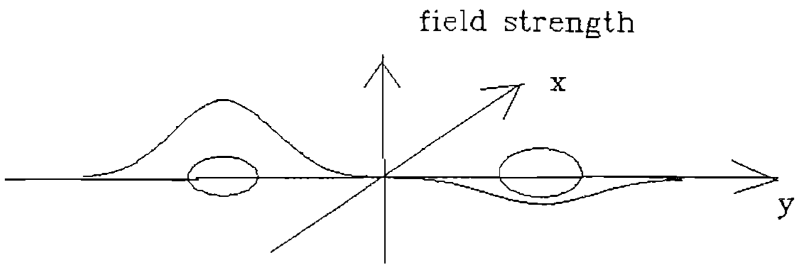

(b) odd mode

Figure 2.5 Fundamental modes in a nearly–identical–core TC fibre

strength over the two cores is no longer the same. A plot of the even and odd mode distributions is given in figure 2.5. It can be seen that the two modes are no longer strictly odd and even modes as in an identical TC fibre and are quasi-even and quasi-odd modes.

The field in the two cores can be derived the same way as in the last section. The following can be obtained

$$b_1(z) = [b_1(0)\cos(\frac{\kappa_a z}{F}) + jF(b_2(0)\frac{\kappa_{12}}{\kappa_a} + b_1(0)\frac{\beta_b}{\kappa_a})\sin(\frac{\kappa_a z}{F})]\, e^{j\beta_a z} \qquad (38)$$

$$b_2(z) = [b_2(0)\cos(\frac{\kappa_a Z}{F}) + jF(-b_2(0)\frac{\beta_b}{\kappa_a} + b_1(0)\frac{\kappa_a}{\kappa_{12}})\sin(\frac{\kappa_a Z}{F})]\,e^{j\beta_a z} \tag{39}$$

If light of unit power is launched into core 1, i.e. $b_1(0)=1$ and $b_2(0)=0$, then equations 2.40 and 2.41 express the field strength of the two cores.

$$b_1(z) = (\cos(\frac{\kappa_a Z}{F}) + j\frac{\beta_b F}{\kappa_a}\sin(\frac{\kappa_a Z}{F}))\,e^{j\beta_a z} \tag{40}$$

$$b_2(z) = jF\sqrt{\frac{\kappa_{21}}{\kappa_{12}}}\sin(\frac{\kappa_a Z}{F})\,e^{j\beta_a z} \tag{41}$$

The power in the two cores are described in equations 2.42 and 2.43.

$$p_1(z) = 1 - F^2\sin^2(\frac{\kappa_a Z}{F}) \tag{42}$$

$$p_2(z) = \frac{\kappa_{21}}{\kappa_{12}}F^2\sin^2(\frac{\kappa_a Z}{F}) \tag{43}$$

To satisfy the condition of total energy conservation in a lossless waveguide, the sum of $p_1(z)$ and $p_2(z)$ has to be equal to 1, the total input power. It can be seen from equations 2.42 and 2.43 that this is only true when $\kappa_{12}=\kappa_{21}$. Under the assumption that there is only a slight difference between the two cores and a large core separation, we have $\kappa_{12}\approx\kappa_{21}$, thus the energy is roughly conserved and the equations 2.42 and 2.43 are a good approximation of the power in the cores. Hence

$$p_2(z) = F^2\sin(\frac{\kappa_a Z}{F}) \tag{44}$$

The breakdown of power conservation in equations 2.42 and

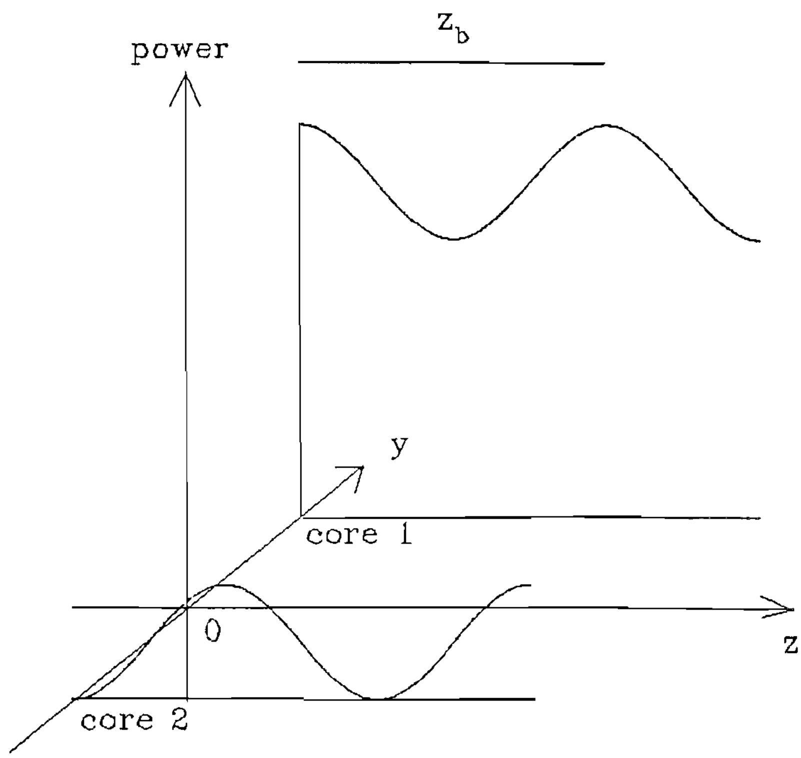

Figure 2.6 Power coupling in a nearly-identical-core TC fibre

2.43 is due to the approximation we made in deriving the field amplitudes in the two cores (equations 2.38 and 2.39). We took the modal power, $|V_1E_{10}|^2$ and $|V_2E_{20}|^2$, as the power in the two cores and neglected modal field overlap. This is especially not true if the two cores are very closely separated, when the difference between κ_{12} and κ_{21} is large. Besides, the normal modes of the TC fibre cannot be accurately described by a superposition of the fundamental modes of the two isolated fibres in this situation. A much more complicated analysis has to be used, in which extra terms in the modal superposition have to be added to get a better simulation of the normal modes.

In the equations above, F is always less than 1. Therefore equations 2.42 and 2.44 show only a fraction of the total power oscillating between the two cores. The beat length is defined as the fibre length taken to complete such a partial power oscillation.

$$z_b = \frac{\pi F}{\kappa_a} \tag{45}$$

A plot of the power in the two cores of a nearly-identical TC fibre is give in figure 2.6.

In a step-index profile TC fibre with slight difference between core indices and radii, δn_{co} and $\delta \rho$ respectively, the propagation-constant difference between the cores can be obtained[11].

$$\delta\beta = \frac{1}{\rho}\frac{U^2}{V}\frac{1}{\sqrt{2\Delta}}\left(\frac{W^2}{U^2}+\frac{K_0^2(W)}{K_1^2(W)}\right)\frac{\delta n_{co}}{n_{co}}+2\Delta\frac{K_0^2(W)}{K_1^2(W)}\frac{\delta\rho}{\rho} \tag{46}$$

Plot of F^2 against $\delta n_{co}/n_{co}$ and $\delta\rho/\rho$ are given in figures 2.7 and 2.8. It can be seen that, in an identical-core TC fibre with $d/\rho=4$ and $V=2.4$, the coupling power will reduce to 27% with a radius difference of 1%, or reduce to 16% with a relative index change of 0.005% (a typical value for a fibre is 0.5%). This indicates a strict parameter control has to be maintained during fabrication.

2.2.5 Periodically-perturbed TC fibres

In this section, a TC fibre with periodic perturbation along fibre axis is analyzed. In practice, such a perturbation can be applied by fibre flexural wave excited

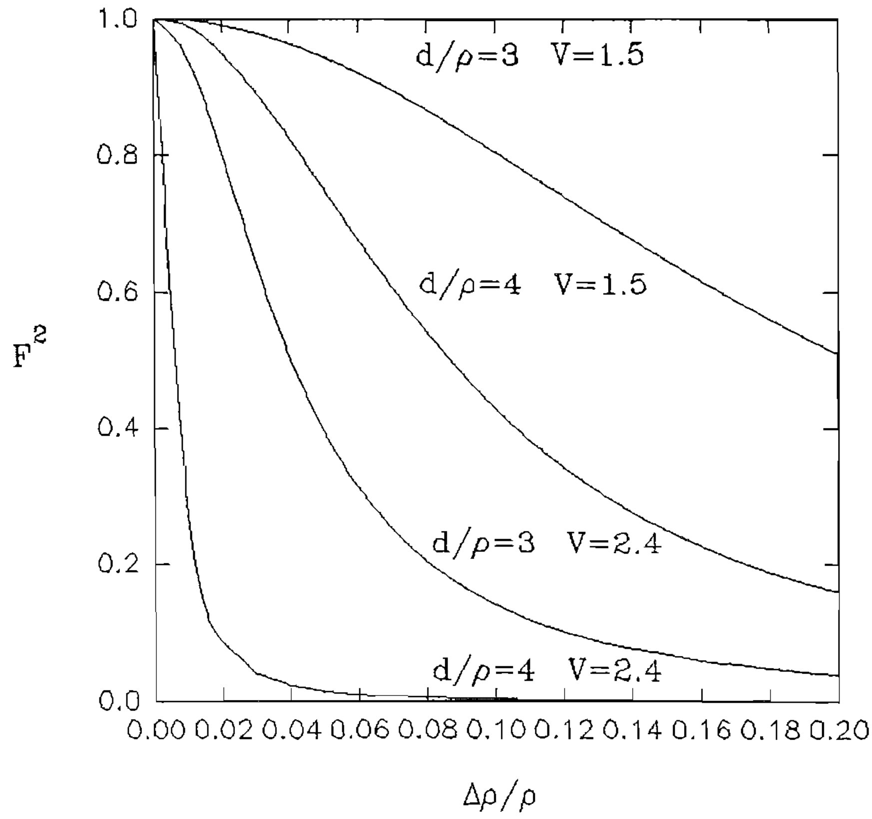

Figure 2.7 F^2 against $\Delta\rho/\rho$ in a nearly-identical-core TC fibre

by an acoustic modulator, fibre micro-bending and photon-induced photosensitivity, and produces intermodal coupling, hence devices such as fibre modulators, frequency shifters and filters. We use the normal modes derived in the last two sections in this analysis. This gives a clearer insight into the coupling between the real modes of the TC fibre. The two normal modes can be written as

$$E_q = a_q(x,y)\, e^{j\beta_q z} \tag{47}$$

where q=e or o. In the periodically perturbed TC fibre, the field can be described by a superposition of the unperturbed fibre modes with slow axially varying amplitudes.

The perturbed relative refractive index distribution can be

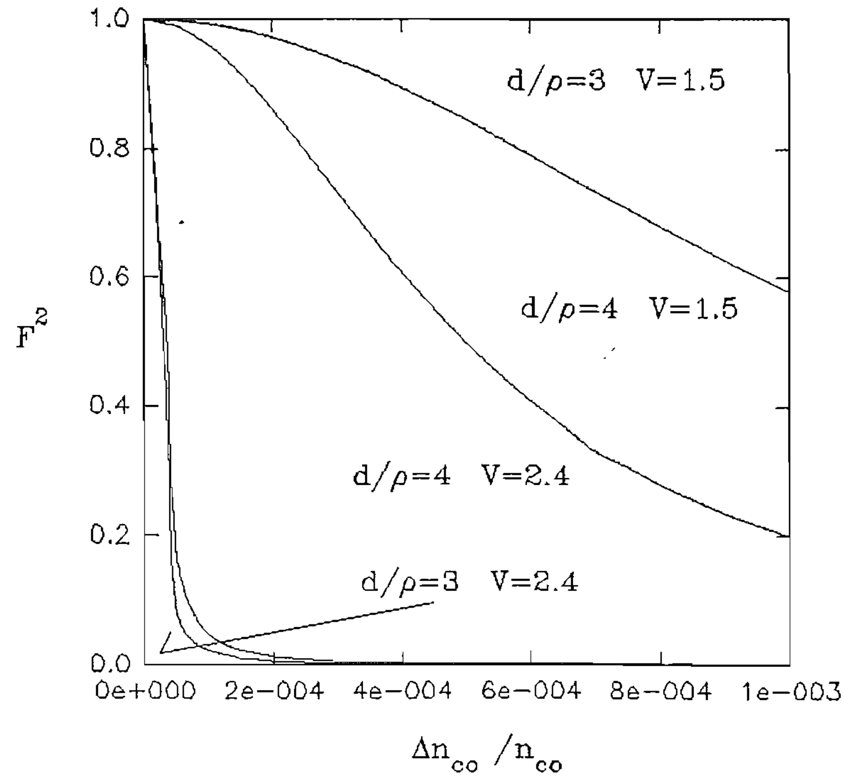

Figure 2.8 F^2 against $\Delta n_{co}/n_{co}$ in a nearly-identical-core TC fibre

$$E = V_e(z)E_e + V_o(z)E_o \tag{48}$$

represented as

$$\Delta(x,y,z) = \Delta_0(x,y) + \Delta^p(x,y)\cos(k_p z) \tag{49}$$

where $\Delta_0(x,y)$ is the relative refractive index distribution of the unperturbed fibre and $\Delta^p(x,y)\cos(k_p z)$ is the perturbation applied. E satisfies the Maxwell equation

$$[\nabla^2 + (n_{cl}k)^2(1+2\Delta)]E = 0 \tag{50}$$

The two normal modes in equation 2.48 satisfy the Maxwell equation for the unperturbed TC fibre, therefore

$$[\nabla^2 + (n_{cl}k)^2(1+2\Delta_0)]E_q = 0 \tag{51}$$

where q=e or o. The following equations can thus be derived from equations 2.50 and 2.51 (see appendix B).

$$\frac{dV_e}{dz} - j\kappa_{ee}\cos(k_p z)V_e - j\kappa_{eo}\cos(k_p z)e^{j(\beta_o-\beta_e)z}V_o = 0 \tag{52}$$

$$\frac{dV_o}{dz} - j\kappa_{oo}\cos(k_p z)V_o - j\kappa_{oe}\cos(k_p z)e^{j(\beta_e-\beta_o)z}V_e = o \tag{53}$$

where

$$\kappa_{ee} = \frac{(n_{cl}k)^2}{\beta_e}\frac{\int_{A\infty}\Delta^p a_e^2 dA}{\int_{A\infty} a_e^2 dA} \tag{54}$$

$$\kappa_{eo} = \frac{(n_{cl}k)^2}{\beta_e}\frac{\int_{A\infty}\Delta^p a_e a_o dA}{\int_{A\infty} a_e^2 dA} \tag{55}$$

$$\kappa_{oo} = \frac{(n_{cl}k)^2}{\beta_o}\frac{\int_{A\infty}\Delta^p a_o^2 dA}{\int_{A\infty} a_o^2 dA} \tag{56}$$

$$\kappa_{oe} = \frac{(n_{cl}k)^2}{\beta_o}\frac{\int_{A\infty}\Delta^p a_o a_e dA}{\int_{A\infty} a_o^2 dA} \tag{57}$$

An asymptotic solution for equations 2.52 and 2.53 can be obtained by taking out the slowest varying components in the equation (see appendix B).

$$\frac{dV_e}{dz} - \frac{j}{2}e^{-j(\beta_e-\beta_o-k_p)z}\kappa_{eo}V_o = 0 \tag{58}$$

$$\frac{dV_o}{dz} - \frac{j}{2}e^{j(\beta_e-\beta_o-k_p)z}\kappa_{oe}V_e = 0 \tag{59}$$

If unit power is launched into core 1, the power in the two cores are expressed in equations 2.60 and 2.61.

$$p_1(z) = 1 - F_p^2 \sin^2\left(\frac{\kappa^p z}{F_p}\right) \tag{60}$$

$$p_2(z) = F_p^2 \sin^2\left(\frac{\kappa^p z}{F_p}\right) \tag{61}$$

where

$$F_p = \frac{1}{\sqrt{1+\frac{\sigma^2}{4\kappa^p}}} \tag{62}$$

$$\kappa^p = \frac{\sqrt{\kappa_{oe}\kappa_{eo}}}{2} \tag{63}$$

$$\sigma = \beta_e - \beta_o - k_p \tag{64}$$

The light will be coupled from one core to the other and back at a beat period $z_b=\pi F_p/\kappa^p$. If higher order components are considered, small ripples of much higher frequency will appeared on the asymptotic solution. The perturbed coupling coefficient, κ^p, is maximised when the perturbation has a different sign over the two cores. If an uniform perturbation is applied to both cores, the perturbed coupling coefficient will be zero, due to the modal orthogonality in the modal overlap integral in equations 2.55 and 2.57. For $\Delta^p(x,y)=\Delta^p$ over core 1 and $\Delta^p(x,y)=-\Delta^p$ over core 2, κ^p can be calculated easily if a Gaussian approximation is used for the modes. Figure 2.9 gives the result of the analysis for a TC fibre with $\Delta_1=\Delta_2=0.00521$, $\rho_1=1.93\mu m$, $\rho_2=1.66\mu m$, and $d=6.5\mu m$ (TC9 in appendix D). The normal coupling of the fibre is also plotted on figure 2.10. In this fibre with an index perturbation of 10^{-4}, only about 0.1 metre of perturbation length is needed to cause a 100% intermodal coupling around a wavelength of $1.1\mu m$.

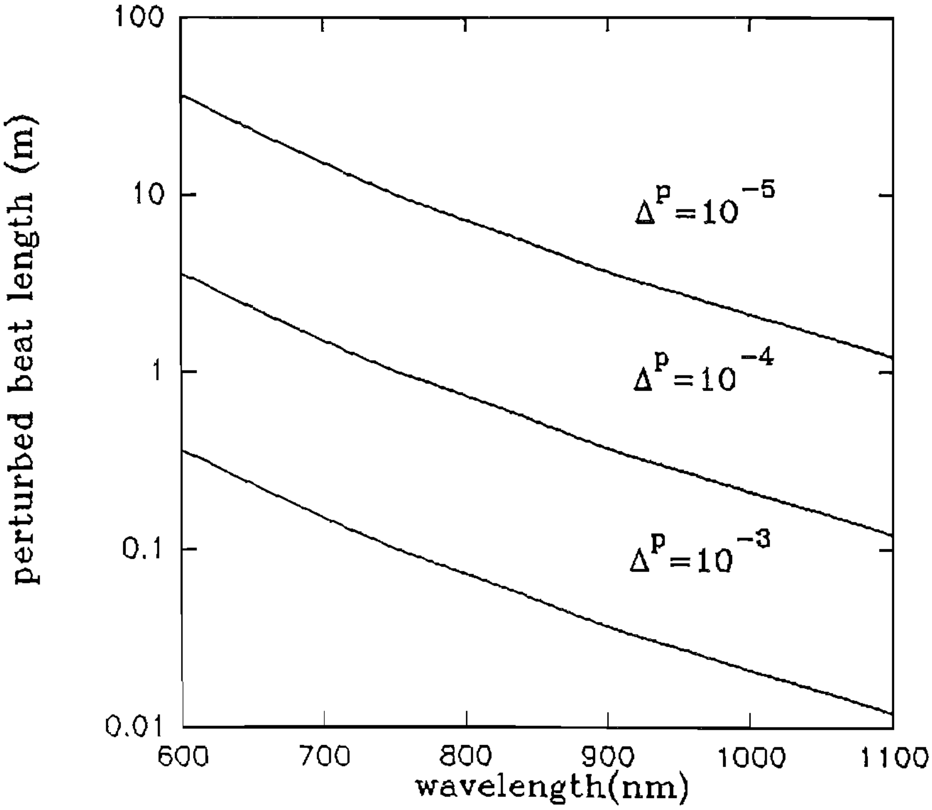

Figure 2.9 Perturbed beat length in a fibre with $\rho_1=1.93\mu m$, $\rho_2=1.66\mu m$, $\Delta_1=\Delta_2=0.00521$ and $d=6.5\mu m$.

2.2.6 Doped TC fibres

One core of a TC fibre can be doped with rare-earth ions, and therefore, if appropriate pump light is used, light at certain wavelength in that core will experience a gain during propagation. Reduced switching power is possible in a TC fibre switching device constructed this way. In this section, a theoretical analysis of such a TC fibre is given and analytical solution obtained.

We introduce a complex refractive index for the case of transmission media with gain. The following analysis is equally applied in the case of loss experienced in the fibre.

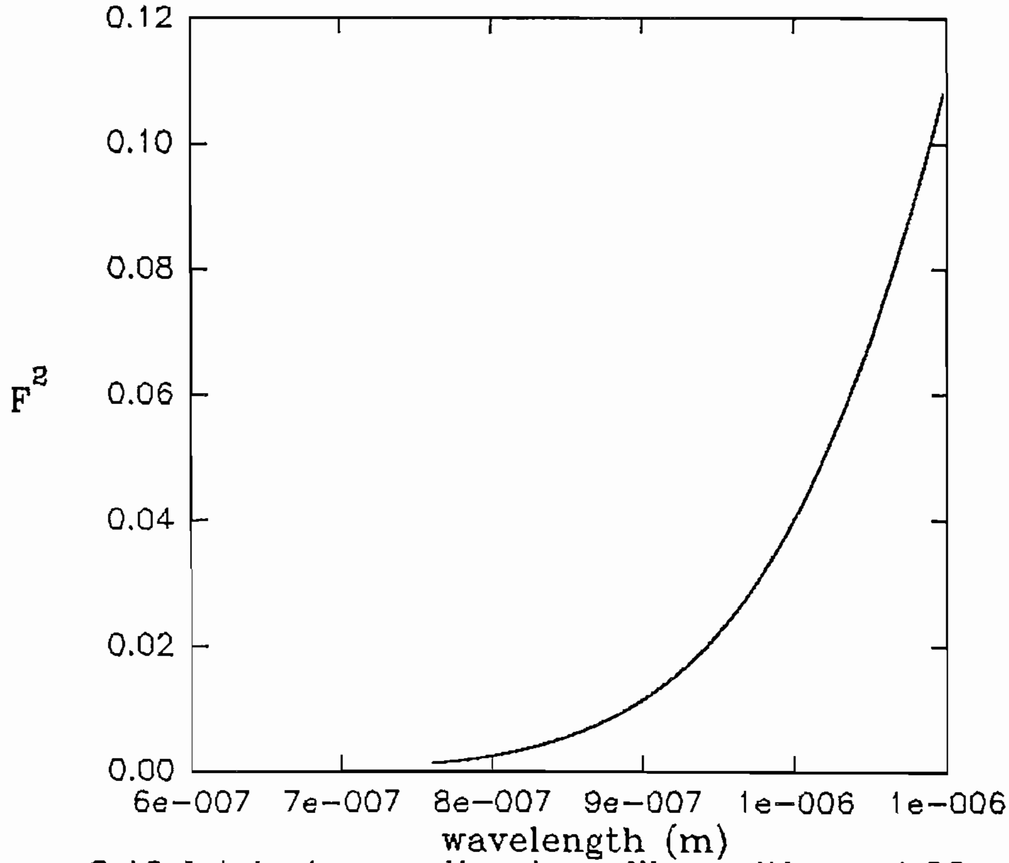

Figure 2.10 Intrinsic coupling in a fibre with ρ_1=1.93μm, ρ_2=1.66μm, Δ_1=Δ_2=0.00521 and d=6.5μm.

$$\eta = n(1+j\chi) \tag{65}$$

where n and $n\chi$ are the real and imaginary parts of the refractive index respectively. For a weakly guided fibre, we define the relative refractive index distribution as

$$\Delta(x,y) = \Delta_0(x,y) + j[1+\Delta_0(x,y)]\chi(x,y) \tag{66}$$

We use the normal modes of the fibre again in the following analysis. The normal modes of the TC fibre without gain are

$$E_q = a_q(x,y)\, e^{j\beta_q z} \tag{67}$$

where q=e or o. They satisfy the Maxwell equation for the TC fibre without gain, therefore

$$[\nabla^2+(n_{cl}k)^2(1+2\Delta_0)]E_q=0 \tag{68}$$

where q=e or o. The field in the TC fibre with gain is expressed as the superposition of the two normal modes.

$$E=V_e(z)E_e+V_o(z)E_o \tag{69}$$

It satisfies the Maxwell equation for the TC fibre with gain.

$$[\nabla^2+(n_{cl}k)^2[1+2\Delta_0+2j(1+\Delta_0)\chi]]E=0 \tag{70}$$

We can derive the following equations from equations 2.68 and 2.70 if we ignore the second order derivative terms of $V_q(z)$ (q=e,o) on the ground that it is slowly varying (see appendix C).

$$\frac{dV_e}{dz}+\kappa_{ee}V_e+\kappa_{eo}e^{j(\beta_o-\beta_e)z}V_o=0 \tag{71}$$

$$\frac{dV_o}{dz}+\kappa_{oo}V_o+\kappa_{oe}e^{j(\beta_e-\beta_o)z}V_e=0 \tag{72}$$

where

$$\kappa_{ee}=\frac{(n_{cl}k)^2}{\beta_e}\frac{\int_{A\infty}(1+\Delta_0)\chi a_e^2dA}{\int_{A\infty}a_e^2dA} \tag{73}$$

$$\kappa_{eo}=\frac{(n_{cl}k)^2}{\beta_e}\frac{\int_{A\infty}(1+\Delta_0)\chi a_e a_o dA}{\int_{A\infty}a_e^2dA} \tag{74}$$

$$\kappa_{oe}=\frac{(n_{cl}k)^2}{\beta_o}\frac{\int_{A\infty}(1+\Delta_0)\chi a_o a_e dA}{\int_{A\infty}a_o^2dA} \tag{75}$$

$$\kappa_{oo}=\frac{(n_{cl}k)^2}{\beta_o}\frac{\int_{A\infty}(1+\Delta_0)\chi a_o^2dA}{\int_{A\infty}a_o^2dA} \tag{76}$$

$V_q(z)$ (q=e,o) can be solved from equations 2.71 and 2.72 and

E can be obtained from equation 2.69 (see appendix C).

$$E = E_1\left(a_e + j\frac{a_o}{2l}\sqrt{\frac{\kappa_{oe}}{\kappa_{eo}}}\right)e^{\left(-\kappa_{ee}+j\beta_e-j\frac{\kappa_x}{2l}\right)z} + E_2\left(a_o - j\frac{a_e}{2l}\sqrt{\frac{\kappa_{eo}}{\kappa_{oe}}}\right)e^{\left(-\kappa_{oo}+j\beta_o+j\frac{\kappa_x}{2l}\right)z} \tag{77}$$

where E_1 and E_2 are constants determined by the initial conditions, and

$$\kappa_x = \sqrt{\kappa_{oe}\kappa_{eo}} \tag{78}$$

$$l = \frac{j(\kappa_{ee}-\kappa_{oo}) + (\beta_e-\beta_o)}{2\sqrt{\kappa_{oe}\kappa_{eo}}} \tag{79}$$

The normal modes for the TC fibre with gain are represented by the first and the second term in the equation 2.77. The new transverse modal distributions have deviated away from $a_e(x,y)$ and $a_o(x,y)$ of the original TC fibre to become

$$a_e + j\frac{a_o}{2l}\sqrt{\frac{\kappa_{oe}}{\kappa_{eo}}} \tag{80}$$

and

$$a_o - j\frac{a_e}{2l}\sqrt{\frac{\kappa_{eo}}{\kappa_{oe}}} \tag{81}$$

The introduction of an imaginary part in the refractive index has caused the two normal modes in the original TC fibre to couple. In fibres with gain<100dB/m, χ is two orders of magnitude smaller than Δ_0. κ_x is therefore two order of magnitude smaller than $(\beta_e-\beta_o)/2=\kappa_a/F$, and $|l|>100$. The two new normal modes of the TC fibre with gain are well approximated by the two normal modes of the original TC fibre. The real parts in the exponents in equation 2.77 give the gain coefficients for the even and odd modes. The $\pm j\kappa_x/2l$ terms in the exponents are again due to the coupling between the two original normal modes. These terms can again be neglected in the case where the fibre gain is smaller than 100dB/m. The field can therefore be approximated as

$$E = E_1 e^{-\kappa_{ee} z} E_e + E_2 e^{-\kappa_{oo} z} E_o \tag{82}$$

In the case where the gain is distributed non-uniformly over the two cores and the two cores are dissimilar, different gain coefficients will result for the two TC fibre modes.

2.3 Fabrication of TC fibres

2.3.1 Background

The most straight-forward TC fibre fabrication technique is the rod-in-hole method, involving insertion of two rods into two parallel holes drilled in a much larger cladding rod. The core rods have higher refractive indices than the cladding rod. The preform is then pulled in a conventional way. The radii and refractive indices of the two rods can be selected individually to satisfy specific design requirements. The distance between the two parallel holes can also be controlled. This method is simple and versatile, so it is used by many researchers. The disadvantages of this technique are chiefly that it is difficult to precisely control the core radius and core separation during fibre pulling. This is because a tight fit between the core rods and holes is usually difficult to obtain, leading to unpredictable collapse conditions during the pulling process. This causes that the two holes to collapse differently. As mentioned in section 2.2.4, the core radius has to be controlled very precisely (« 1%); this renders the method inadequate for precisely controlled fabrication. The unpredictable collapse process can also lead to uneven stress around the core rods and thus misshapen cores. This is also very undesirable, especially for making strongly coupled TC fibres. Another disadvantage of this method is high loss due to poor cladding quality and imperfection at the core and cladding interface. However this is not very important for device applications in which only a short length of fibre is normally required.

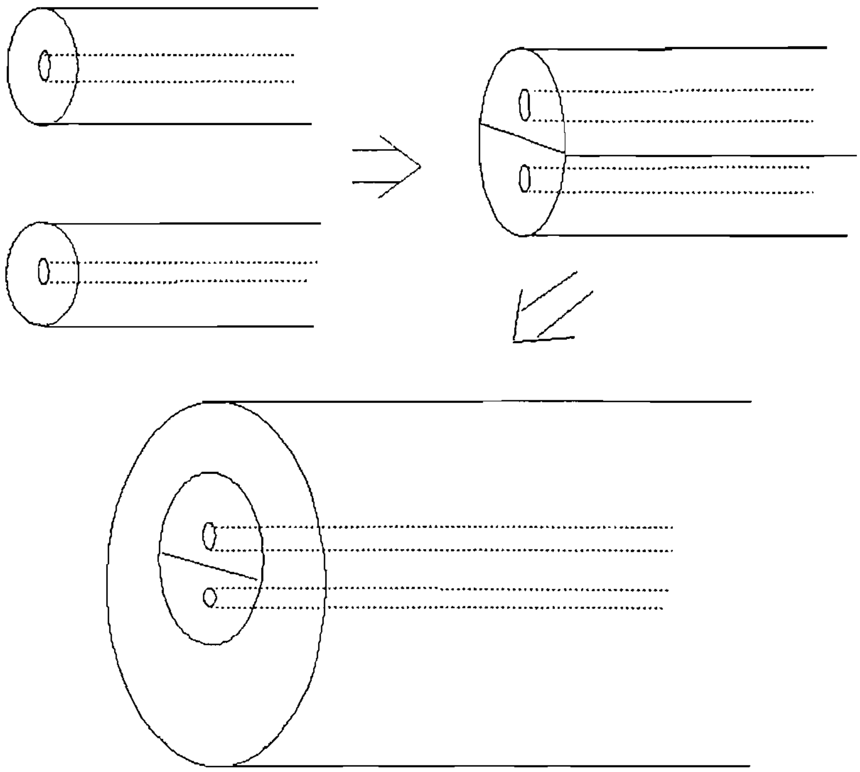

Figure 2.11 TC preform preparation

The technique used in the thesis is an improved method. The TC preform preparation involves making two ordinary MCVD (Modified Chemical Vapour Deposition) preforms, milling off one side of each of the preforms (see figure 2.11), then putting the milled surfaces of the preforms together and inserting them into two overlapping holes drilled in a large glass rod with slight larger diameters than those of the preforms. The TC preform is then pulled in a conventional way.

In an MCVD preform the core radius and refractive index profile have good uniformity over a reasonably long length. The preforms can also be made with different characteristics to meet different designs. The depth of milling determines the core-to-core separation, which can be scaled down to obtain an accurate core-to-core separation in the fibre.

This method guarantees the proper cladding layer surrounding both cores and better core and cladding interface, ensuring a lower loss than the rod-in-hole method. Most of all, this method enables the core radii and separation to be determined from the preform, thus permitting precise control over these parameters. TC fibres with loss in the region of 10 dB/km are obtained routinely (the loss is measured with light launched into both cores and detection of overall output). The imperfection formed from the interfaces in a TC preform is partially due to the irregularity of the interface and partially trapping of air bubbles. These imperfections cause scattering which can give rise to high loss and may also disturb coupling in the fibre. The new technique restricts interface irregularities to the flat interface between the cores, thus reducing the loss and risk of disturbance to the coupling. With this method, fibres with 100% coupling are achieved routinely.

2.3.2 Overview of MCVD method

As many fibre preforms mentioned in this thesis are made by the MCVD method, a brief description of this technique is necessary at this point. The MCVD method is based on the high temperature oxidation of reactant gases in a rotating tube. The chemical reagents, $SiCl_4$, O_2 and suitable glass-forming dopants, which control the refractive index of the deposited glass, flow inside a rotating silica substrate tube mounted in a glass working lathe and are heated by an external burner traversing in the same direction as the gas flow. Gas-phase oxidation in the burner's hot zone results in the formation of soot particles which are deposited further downstream by thermophoresis process, and subsequently, when the burner passes, the deposited soot is fused to form a glassy layer by viscous sintering. The refractive index of the deposited glass is controlled by altering the relative amount of glass-forming dopants, for example, GeO_2 and P_2O_5, in the soot. Several glass layers of required refractive indices are deposited and then the tube is collapsed by heating to over 2000°C. The preform is then pulled into a fibre of the required refractive index profile.

2.3.3 TC preform preparation and pulling

The milling and drilling are done on an ultrasonic glass mill. Errors in milling depth can be as large as 100μm and are mainly due to the visual judgement of the initial contact between the preform and milling head. The smoothness of the milled surface is normally satisfactory. Before insertion of the milled preform, the drilled glass rod and the milled preforms are thoroughly cleaned by soaking in glass-cleaning solution and rinsing with demineralised water. Fibre is pulled on a conventional fibre-pulling tower. During the pulling process, a higher temperature is normally used to further polish the preform interface.

2.3.4 TC fibres

A variety of TC fibres, shown in figure 2.12, have been

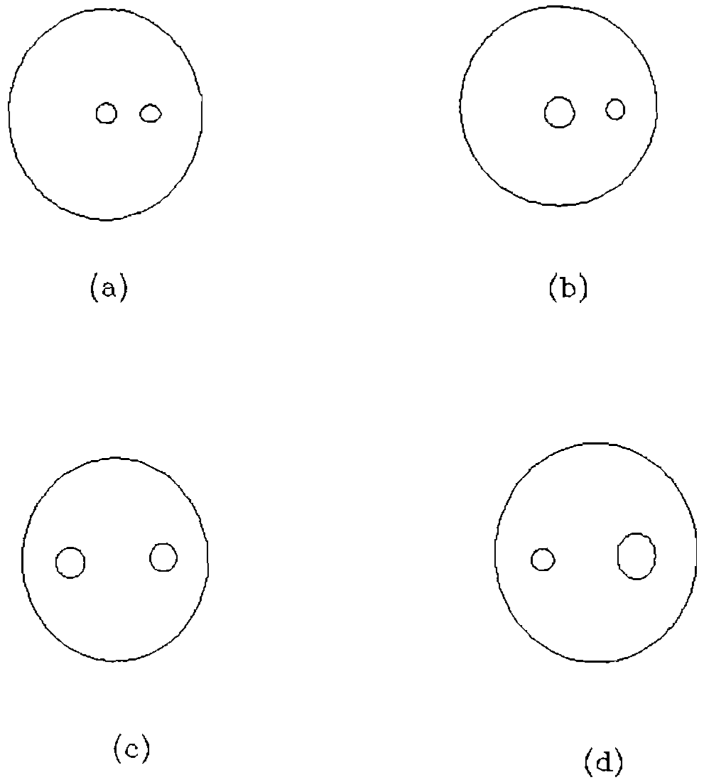

Figure 2.12 Different TC fibres

made for different applications. The identical-core TC fibre with a core in the centre of the fibre, which eases the splicing with another single-core fibre, is made for nonlinear switching and the cascaded TC filter (figure 2.12(a)). The non-identical-core TC fibre with the larger core in the centre is designed for demonstrating intermodal coupling in TC fibres (figure 2.12(b)). The non-identical-core TC fibre in figure 2.12(c) is used for a special interferometer design in which the non-coupled cores are used as two arms of a stable interferometer. Figure 2.12(d) shows an identical-core TC fibre with a very large core separation for a polarisation maintained coupler, in which four polarisation-maintained fibres are spliced to the two cores of the TC fibre on both ends with polarisation axis being appropriately aligned and the TC fibre is then tapered down to a much smaller diameter to caused coupling between the cores.

2.4 Characterisation of TC fibres

The main parameters of a TC fibre are coupling coefficient κ_a and coupling ratio F. Experimental determination of the two parameters will define the coupling characteristic of the fibre. The parameters of fibres used in this section are listed in table 2.1.

Table 2.1 TC fibre parameters

Name	$\rho_1(\mu m)$	$\rho_2(\mu m)$	$\Delta_1=\Delta_2$	$d(\mu m)$
TC1	1.76	1.76	0.00233	10
TC2	2.5	2.5	0.00233	14
TC3	4.22	4.22	0.00245	21

2.4.1 Coupling coefficient

The coupling coefficient can be calculated from the spectral transmission of a TC fibre. One example is given in figure 2.13. Light is launched into one core by splicing the core with an ordinary fibre and light transmission from different cores is detected by splicing the core with another ordinary fibre. The curve is measured from a 340.5mm length of TC2. The transmission is governed by equations 2.28 and 2.29, thus the phases at the peaks and troughs can be identified after the first peak ($\kappa_a z=\pi/2$ or π) is determined. The coupling coefficient is then calculated using the known fibre length from the equations. The results for TC1 and TC2 are given in figures 2.14 and 2.15 respectively. The three sets of data in figure 2.14 are measured from three TC1 samples with

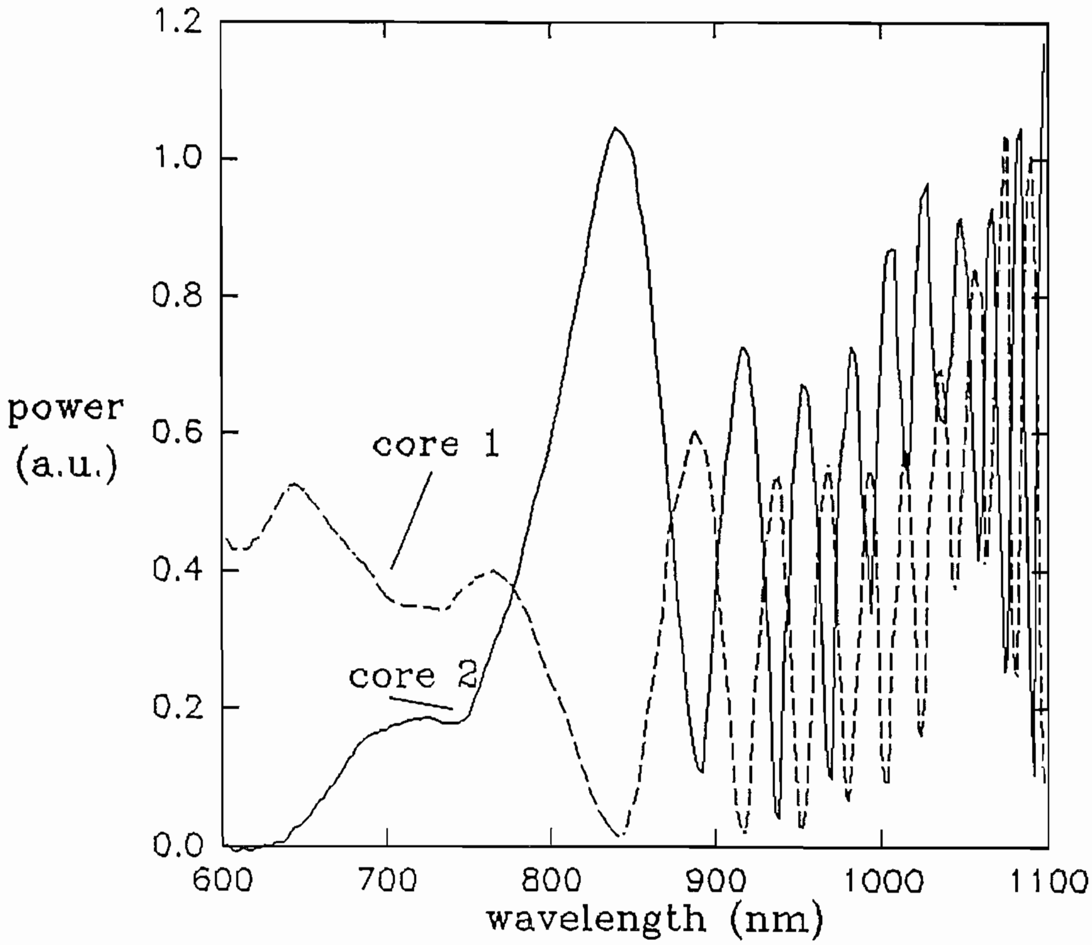

Figure 2.13 Transmission of TC2 (340.5mm)
Light is launched into core 1

lengths of 20.5mm, 16.5mm and 7.5mm. The three sets of experimental data are very consistent. The solid curve is calculated from equation 2.30. At stronger coupling (longer wavelength), the theoretical curve deviates away from the experimental data and gives a much smaller value. This is due to the fact that, when the modal field spreads further into the cladding, the summation of the two fundamental modes of the isolated cores (equation 2.2) is no longer a good approximation. The modal fields are less strongly contained to the cores than the theory predicts, therefore a much larger coupling coefficient than predicted by the theory results. Figure 2.15 gives the experimental and theoretical data on a fibre with smaller coupling (TC2). The lengths of fibre used are 340.5mm, 173mm and 93mm. The experimental data are more scattered than in the

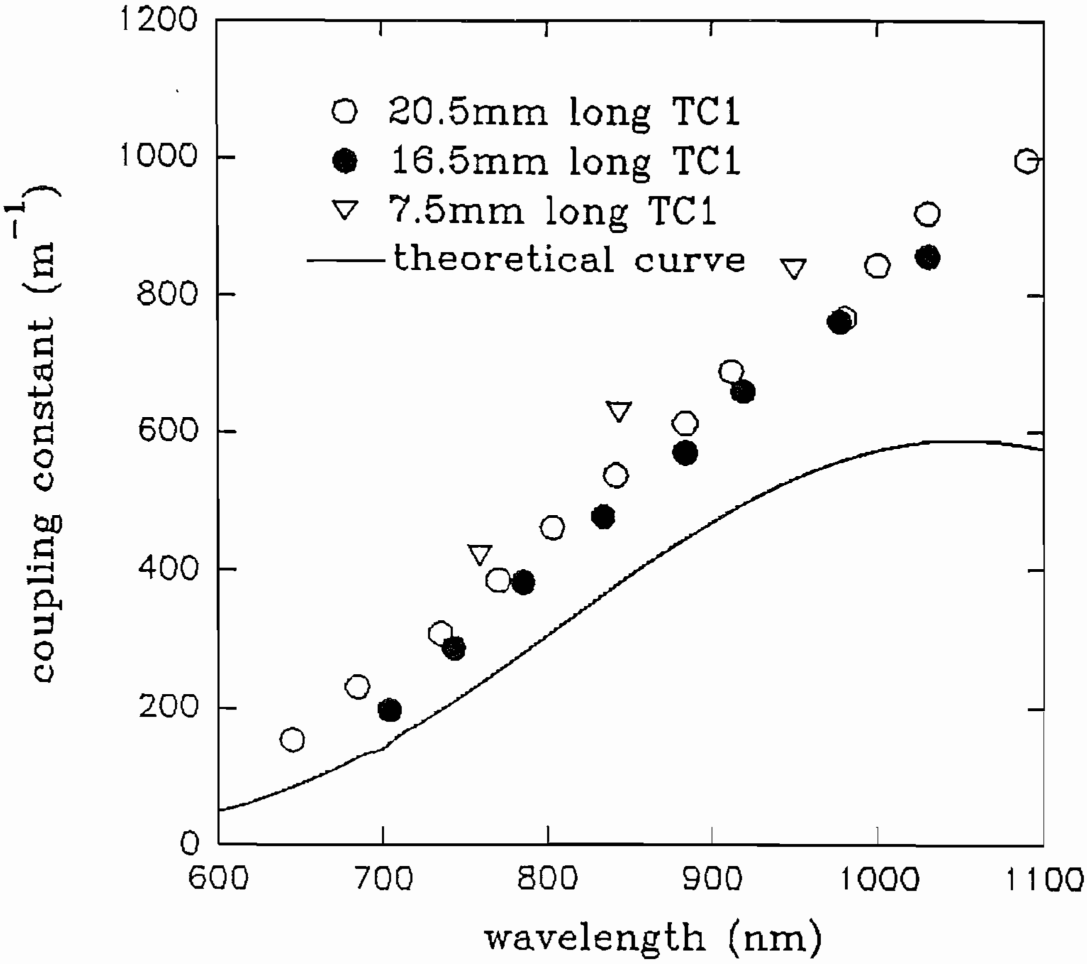

Figure 2.14 Coupling constant for TC1

previous figure; this is due to the weak coupling and longer fibre length used, which will be discussed later in this section. Nevertheless, the experimental data agrees with the theoretical curve reasonably well in this weak coupling case.

2.4.2 Bending sensitivity

Similar sensitivity to slight bends is found among all the TC fibres drawn from four different preforms. Here we report the result obtained with TC3. A bending radius of 5 to 10 meters is usually applied in the measurements. Figure 2.16 shows the transmission from the launching core

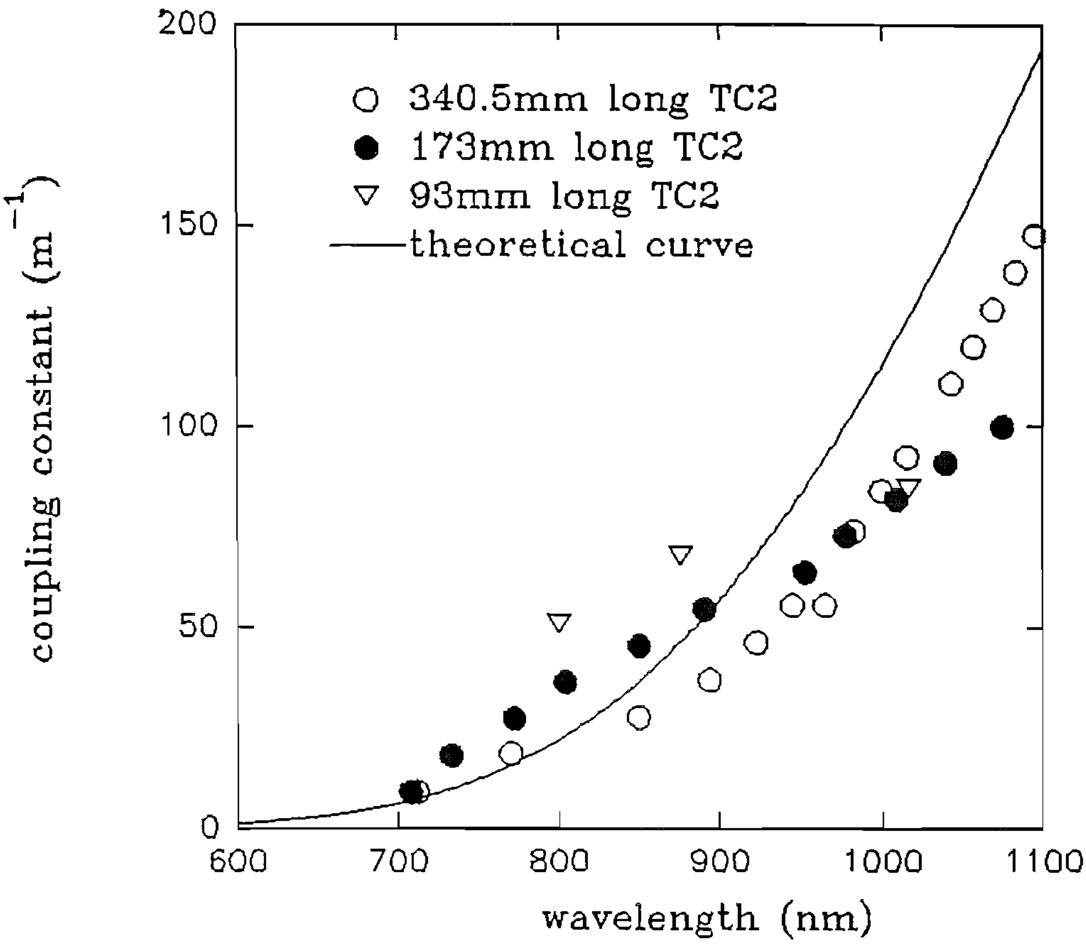

Figure 2.15 Coupling constant for TC2

from a fibre of 928mm long. The randomness in peak amplitudes and positions in the straight fibre suggests a large deviation from the expected coupling characteristics, indicating the coupling is severely disturbed by the small deviation from perfect straightness of the fibre. The transmission with the slight curved fibre also proves this. The result with a shorter length of 364mm shows some improvement (figure 2.17). The slight curved fibre shows a dramatic decrease in the coupling. The coupling in a fibre with a much shorter length (235mm) is not very much changed by the slight curvature in the fibre (figure 2.18). However the shift of the peaks suggests that modal phase is perturbed. The theoretical coupling coefficient and beat length of the fibre are also given in figure 2.19.

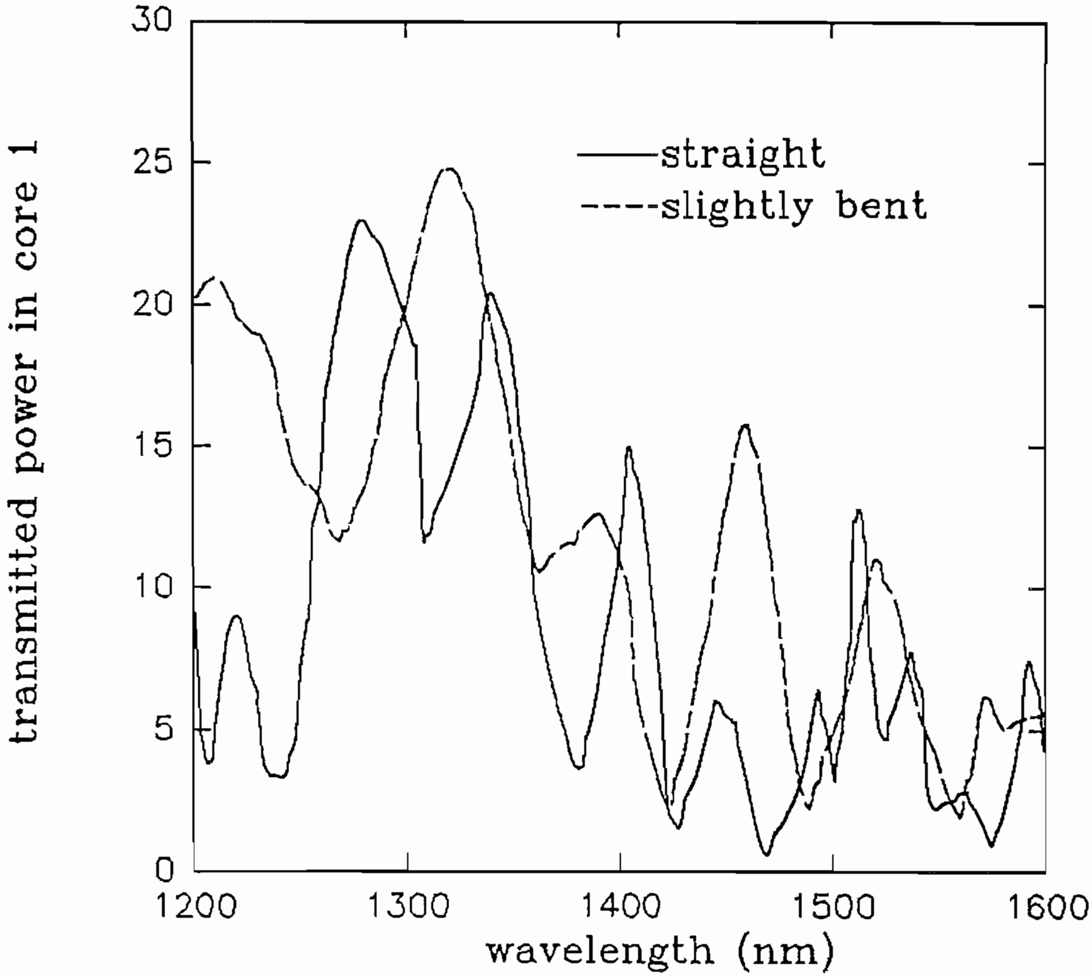

Figure 2.16 Transmission of 928mm TC3
Light is launched into core 1

2.4.3 Discussion

The theory on identical-core TC fibres given in this chapter performed reasonably well in weakly coupled TC fibre (κ<200m^{-1}). However the approximation in equation 2.2 breaks down in strongly coupled fibres. The sensitive response of TC fibre transmission to slight fibre bends is expected from the fact that a bend of few meter radius in the plane of two cores will theoretically produces a large phase difference between the two modes in the fibre. The measurements suggest that any fibre with a beat length longer than 10cm will be impractical unless special attention is given to stabilise it. Fibre with beat length up to 5cm is reasonably stable for a fibre length up to

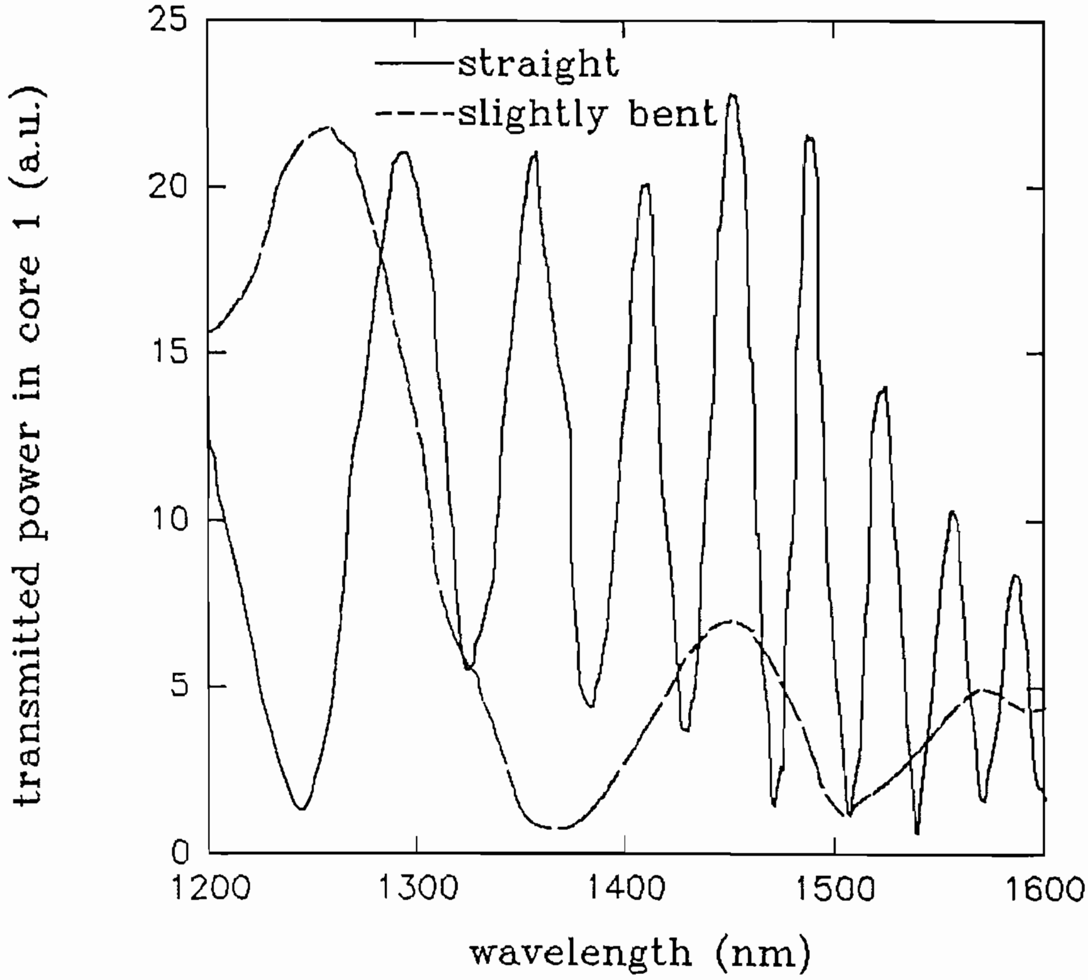

Figure 2.17 Transmission of 364mm TC3
Light is launched into core 1

20cm.

2.5 Conclusions

A new technique for fabrication of TC fibres with low loss and better controlled parameters has been outlined. TC fibres with many different configurations have been fabricated. The theory on identical TC coupling agrees well with experimental data in weakly-coupled fibres (κ<200m^{-1}). In strongly-coupled fibres, the theory predicts rather smaller level of coupling, due to the fact that the

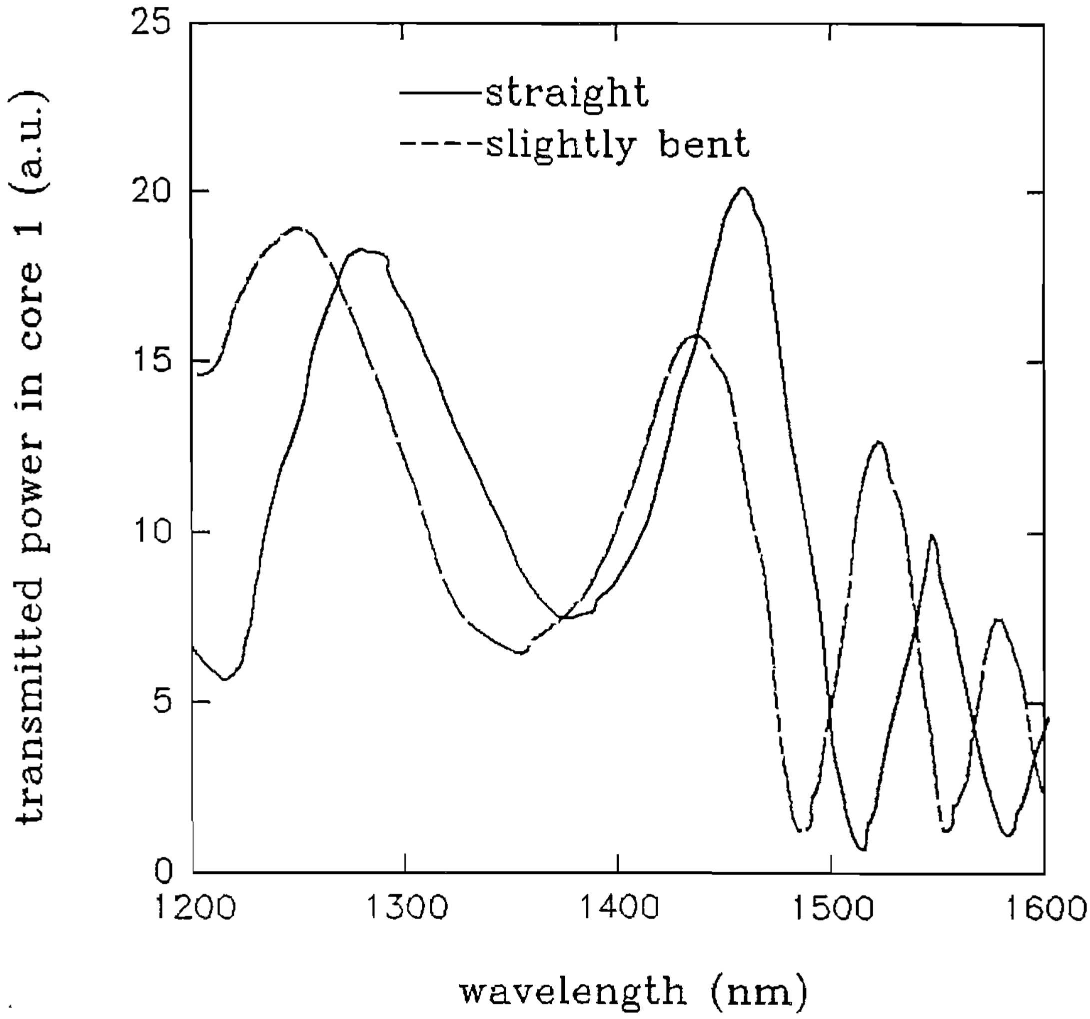

Figure 2.18 Transmission of 235mm TC3
Light is launched into core 1

summation of two fundamental modes of the isolated cores is no longer a good approximation to the TC fibre modes. Weakly-coupled TC fibres of long length are very sensitive to slight bending. Short lengths of strongly-coupled TC fibres are therefore preferred in TC fibre devices.

References

1 S.R. Friberg, A.M. Weiner, Y. Silberg, B.G. Sfez, and P.S. Smith: "Femtosecond switching in a dual-core-fibre nonlinear coupler", Optics Letters, **13**, 1988, pp.904-

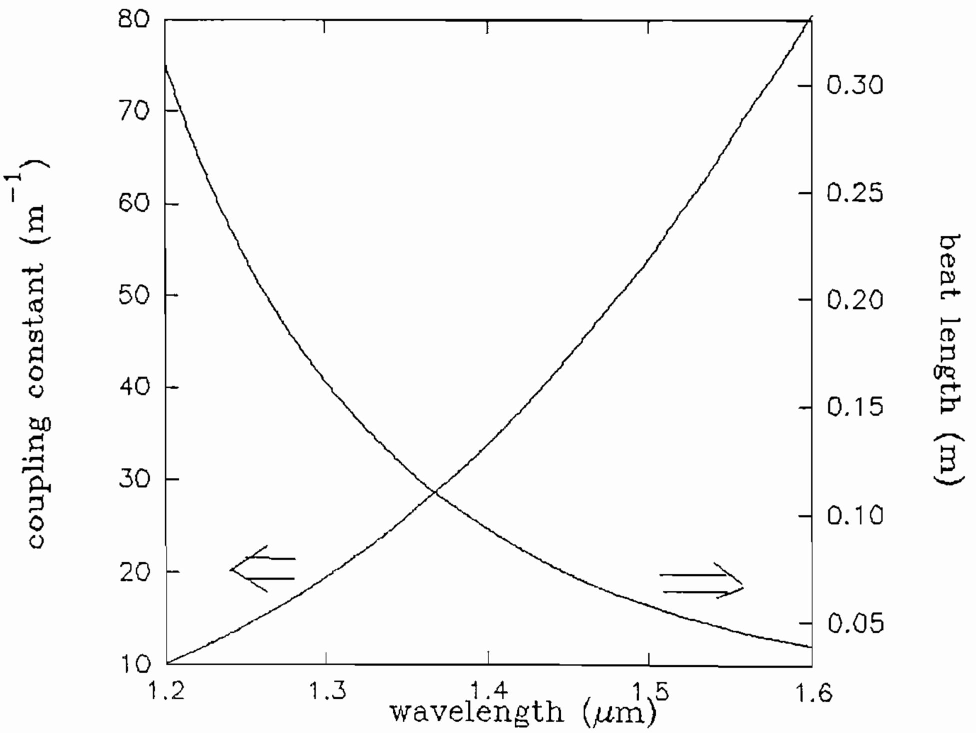

Figure 2.19 Theoretical coupling constant and beat length for TC3

906.

2 K. Okamoto and J. Nova: "Fibre-optic spectral filters consisting of concatenated dual-core fibres", Electronic Letters, **22**, No.4, 1986, pp.211-212.

3 K. Kitayama and Y. Ishida: "Wavelength-selective coupling of two-core optical fibre: application and design", Journal of the Optical Society of American, **2**, 1985, pp.90-94.

4 M. Kobayashi and H. Terui: "Optical demultiplexer using coupling between nonidentical waveguides", Applied Optics, **17**, 1978, pp.3253-3258.

5 D. Marcuse: "Directional-coupler filter using dissimilar optical fibres", Electronics Letters, **21**, 1985, pp.726-727.

6 H.F. Taylor: "Frequency-selective coupling in parallel

dielectric waveguides", Optical Communications, **8**, 1973, pp.421-525.

7 G. Meltz, J.R. Dunphy, W.W. Morey, and Snitzer: "Cross-talk fibre optic temperature sensor" Applied Optics, **22**, 1983, pp.464-477.

8 K. Kitayama, N. Shibata, and M. Ohashi: "Two-core optical fibres: experiment", Journal of the Optical Society of American A, **2**, 1985, pp.84-89.

9 H.A. Haus, W.P. Huang, S. Kawakami, and N.A. Whitaker: "Coupled-mode theory of optical waveguides", Journal of Lightwave Technology, **LT-5**, 1987 pp.16-23.

10 A.W. Snyder: "Coupled-mode theory for optical fibres", Journal of the Optical Society of American, **62**, No.11, 1972, pp.1267-127.

11 A.W. Snyder and J. Love: "Optical waveguide theory", Chapman and Hall, 1983.

12 A.W. Snyder: "Modes of optical waveguides", Journal of the Optical Society of American, **68**, No.3, 1978, pp.297-309.

13 A. Ankiewicz, A.W. Snyder, and X. Zheng: "Coupling between parallel optical fibre cores: critical examination", Journal of Lightwave Technology, **LT-4**, 1986, pp.1317-1323.

14 N. Kishi, E. Yamashita, and H. Kawabata: "Modal and coupling-field analysis of optical fibres with linearly distributed multiple cores", Journal of Lightwave Technology, **7**, No.6, 1989, p.902-907.

15 P.D. McIntyre and A.W. Snyder: "Power transfer between

optical fibres", Journal of the Optical Society of American, **63**, No.12, 1973, pp.1518-27.

16 J.P. Donnelly, H.A. Haus, and L.A. Molter: "Cross power and cross-talk in waveguide couplers", Journal of Lightwave Technology, **6**, No.2, 1988, pp.257-268.

17 A.W. Snyder and A. Ankiewicz: "Optical fibre couplers: optimum solution for unequal cores", Journal of Lightwave Technology, **6**, No.3, 1988, pp.463-474.

Chapter Three Photorefractive Optical Fibres

3.1 Introduction

It has been known for several decades that the colour, or to be more precise the absorption spectrum, of some glasses changes, on being irradiated with γ-rays, x-rays, UV light or even visible light[1,2,3,4]. This photosensitivity has been used a great deal in window, windscreen and spectacle manufacturing, photography, and information storage. There is always an index change in the glasses associated with the absorption change as dictated by the principle of causality, more specifically, the Kramers-Kronig relation. This index change is also useful in many other applications such as grating formation and four-wave-mixing. In optical fibres, the index change has attracted many researchers primarily for its application in making in-core fibre gratings, by exposing the fibre core axially to an interference pattern from a suitable lasers[5,6]. The resultant gratings have many applications including single-mode fibre lasers, WDM telecommunications and fibre sensors. They have many advantages over their conventional counterparts, being compact and easy to align, with low insertion losses. Additionally, the absorption change can also be used in fibre modulators and switches, where light intensity or phase at one wavelength is controlled by light intensity at another wavelength.

In this chapter, we first discuss the investigation of UV-induced loss in transition-metal-doped fibres, then absorption bleaching in Fe^{2+}-doped fibre, and finally the photosensitive response of Ce^{3+}-doped fibre.

3.2 Theoretical background

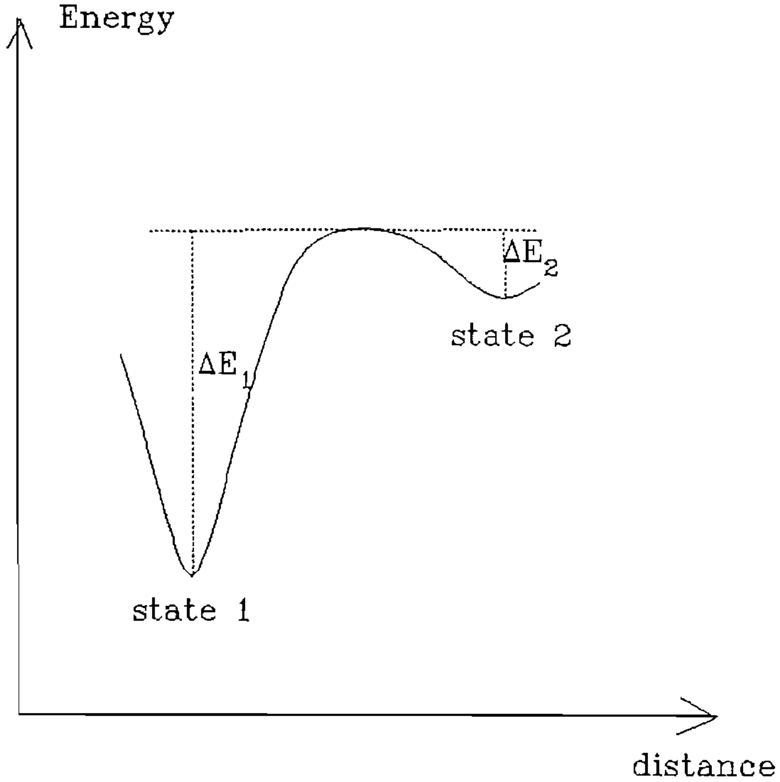

Figure 3.1 Energy diagram in a general photorefractive glass

The photorefractive effect is usually divided into two categories, permanent and temporary effects. Much controversy has been with the nomenclature, in particular, among people working in different areas of physics. However, in general, the effects are referred to as photosensitive and photochromic effects. The detailed physics in many of the glasses known to exhibit photorefractivity is still not clear; however, in general, a two-energy-state system is believed to be involved (see figure 3.1). The system can stay in two stable states, 1 and 2. State 1 has a lower energy and is the stabler of the two. There is an energy barrier between the two states, and an energy, ΔE_1, is needed to transfer the system into state 2, but a smaller energy, ΔE_2, is usually needed to return it to state 1. ΔE_1 and ΔE_2 have a spectrum of values. ΔE_1 usually falls into energy level of γ-rays, x-rays, UV and, sometimes, even visible. ΔE_2 can also be very small. Some photochromic glasses recover spontaneously. However, it is usually necessary to heat up the glass or subject it to IR radiation.

3.3 Transition-metal-doped fibres

3.3.1 Background

Most of the transition metals can be easily incorporated into silica-based fibres, and used to be the cause of strong unwanted IR absorptions in early fibres[7,8,9]. They usually exist in at least two different ionisation states, offering two energy states. If an ion is transferred from one ionisation state to the other by losing or gaining an electron in the glass, the absorption spectrum will alter, thus changing the refractive index. The effects of γ-rays and x-rays on iron-containing glass has been studied by several authors[10,11]. ESR measurements before and after exposure in samples of different silicate glasses doped with iron have shown evidence of a change in the oxidation states of iron.

In this section we investigate the responses of various transition-metal-doped fibres to high power CW argon ion laser light. A description of fabrication procedure for these fibres is outlined. We also studied the bleaching of Fe^{2+} absorption.

3.3.2 Fabrication

3.3.2.1 Background

The solution doping method developed by Townsend and Poole[12] is used in the fabrication of transition-metal-doped fibres. This technique is based on the modified chemical vapour deposition process and enables dopants to be added into an optical fibre in a controllable manner. Cladding layers are first deposited in a conventional way. During core layer deposition, the temperature is reduced in order to deposit a porous oxide soot without consolidation into a glassy state. The deposition temperature is about 1250°C for a SiO_2/GeO_2 core. A higher temperature will reduce the porosity and makes the incorporation of dopants difficult at a later stage. A lower temperature will make the soot loosely adhere to the tube and may peel off in the subsequent soaking and dehydration process. To control the refractive index of the fibre core, the flow rates of the reagents are determined in a similar way to the conventional MCVD process. The tail end of the uncollapsed and unsintered preform is subsequently sealed and the preform removed from the glass lathe. The soot layer is then immersed in a dilute solution of dopant ions for a predetermined time (typically one hour), permitting the dopant-ion/soot bonding to reach saturation. The solution is usually made by dissolving dopant ion halide in water. The dopant concentration in the final fibre is controlled by the dopant concentration in the solution. The soot layer is subsequently dried by rinsing with acetone and blowing with compressed nitrogen gas. The preform is then replaced in the lathe and further dried by flowing drying gases such as oxygen, helium or chlorine through the tube and by heating it to about 500°C by a rapidly traversing burner. The preform is usually dried for one hour and the soot layer is finally sintered into a glass core. The preform is then collapsed and fibres are drawn in the conventional way.

3.3.2.2 Transition-metal-doped fibre fabrication

An iron-doped fibre was fabricated with a saturated Fe_2O_3/HCl solution (PH=2). During collapse, an oxygen-rich atmosphere was maintained. The fibre has a GeO_2/SiO_2 core and a NA of 0.21 (GeO_2/SiO_2 core are assumed for the fibres in this section unless otherwise mentioned).

A copper-doped fibre was fabricated using a solution containing 1.95g $CuCl_2$ and 100ml H_2O. The NA of the fibre is 0.15.

A manganese-doped fibre was made with a solution having 2.05g $MnCl_2.4H_2O$ in 100ml H_2O. The NA is 0.17.

A manganese and iron doped fibre is also made using a solution with 0.5g Fe_2O_3 and 2g $MnCl_2$ in 100ml HCl (20%). The NA is 0.17.

3.3.3 Characterisation

The spectral attenuation of iron-doped fibre is shown in figure 3.2. For comparison, an ordinary GeO_2/SiO_2 core fibre attenuation is also plotted. It can be seen a large loss is present at short wavelength (below 500nm). This is due to Fe^{3+} absorption. The excessive loss indicates a Fe_2O_3 concentration of 130ppm(wt) using data in reference 13. No Fe^{2+} peak around 1100nm is observed in this fibre, indicating that all iron ions go into the Fe^{3+} state.

The spectral loss of the copper-doped fibre is shown in figure 3.3 together with loss of an undoped GeO_2/SiO_2 fibre. A slightly higher loss around 450nm is apparent, but not the broad Cu^{2+} peak around 800nm, suggesting that all the

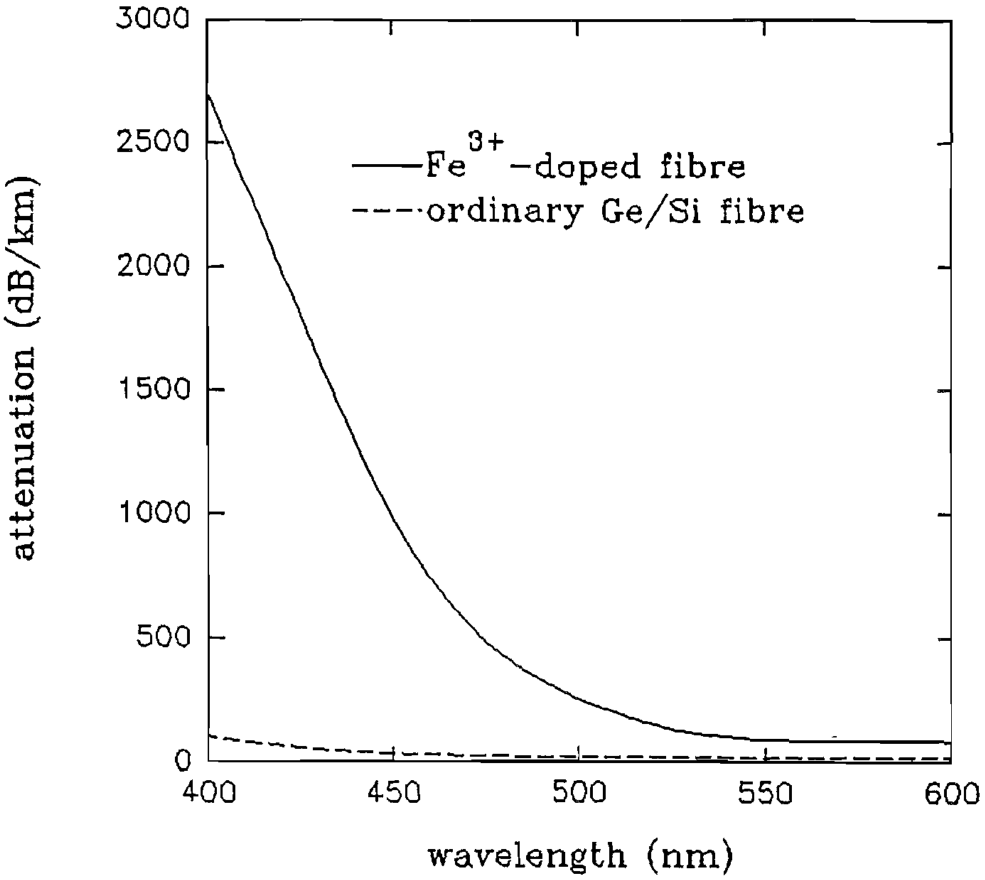

Figure 3.2 Spectral attenuation of a Fe^{3+}-doped fibre and an ordinary Ge/Si fibre

copper ions are in Cu^{1+} state.

The spectral loss of the manganese-doped fibre is shown in figure 3.4. A narrow absorption peak is seen around 520nm, caused by Mn^{3+}. From the data given in reference 8, the concentration of Mn_2O_3 is obtained to be 190ppb(wt). The UV loss of the fibre is also greatly increased.

A Mn^{3+}/Fe^{2+}-doped fibre is also made. The Mn^{3+} ions are doped to increase the possibility of trapping electrons released by Fe^{2+} ions by forming Mn^{2+}. In this fibre, an absorption band at 550nm is observed (figure 3.5), contributed by Mn^{3+}. The strong band at 1100nm is caused by Fe^{2+}. The incorporation of manganese thus had a reducing effect on iron. The concentrations of Mn_2O_3 and FeO are determined to be 220ppb(wt) and 1100ppb(wt) respectively.

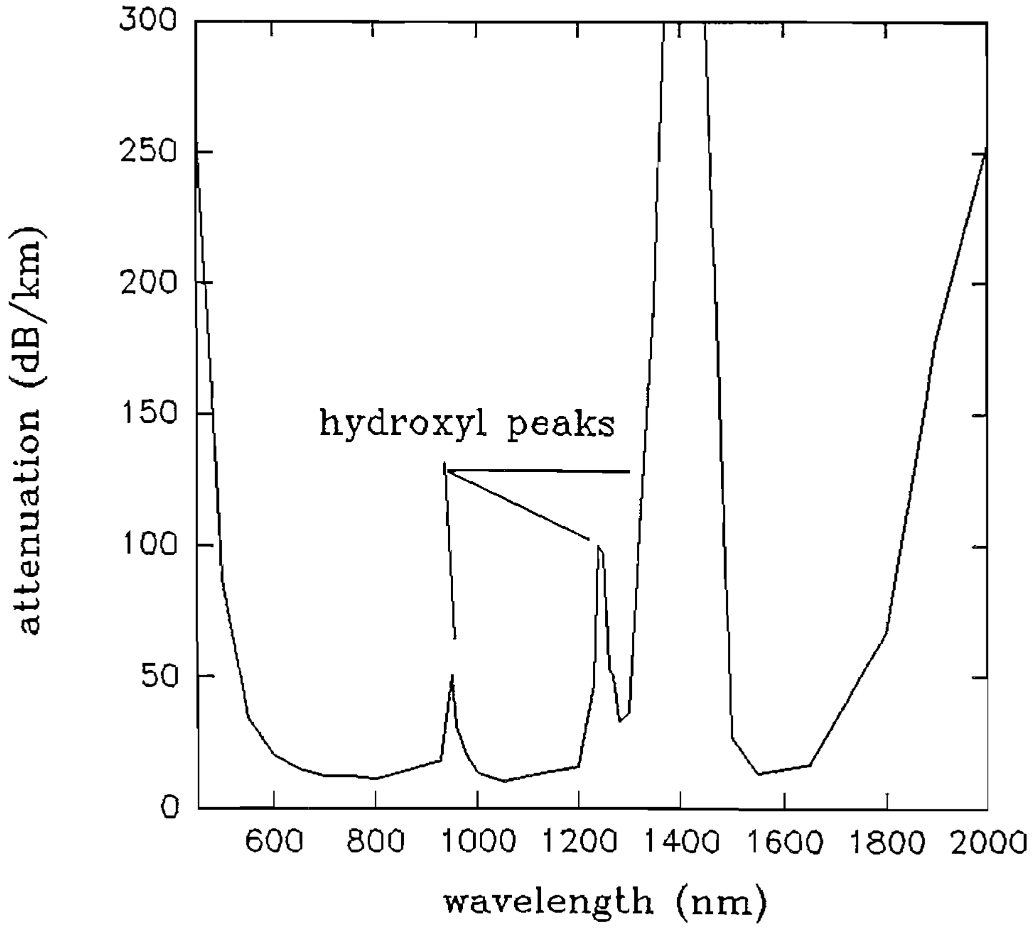

Figure 3.3 Spectral attenuation of a Cu^{1+}-doped fibre

3.3.4 Argon bleaching experiment

A CW argon laser at 488nm was used as the radiation source to investigate the possibility of changing oxidation states in transition metal ions. The iron-doped fibre, manganese-doped fibre and manganese/iron-doped fibre were subjected to few hundred milliwatts of argon laser (equivalent to few $mW/\mu m^2$) for up to 30 minutes. No change of oxidation states was observed in these fibres. Instead a significant increase of absorption in UV and up to near IR was noticed (see figure 3.6). This loss increase has also be observed in other solution-doped fibres. They may be related to an increase in the defect concentration in the glass

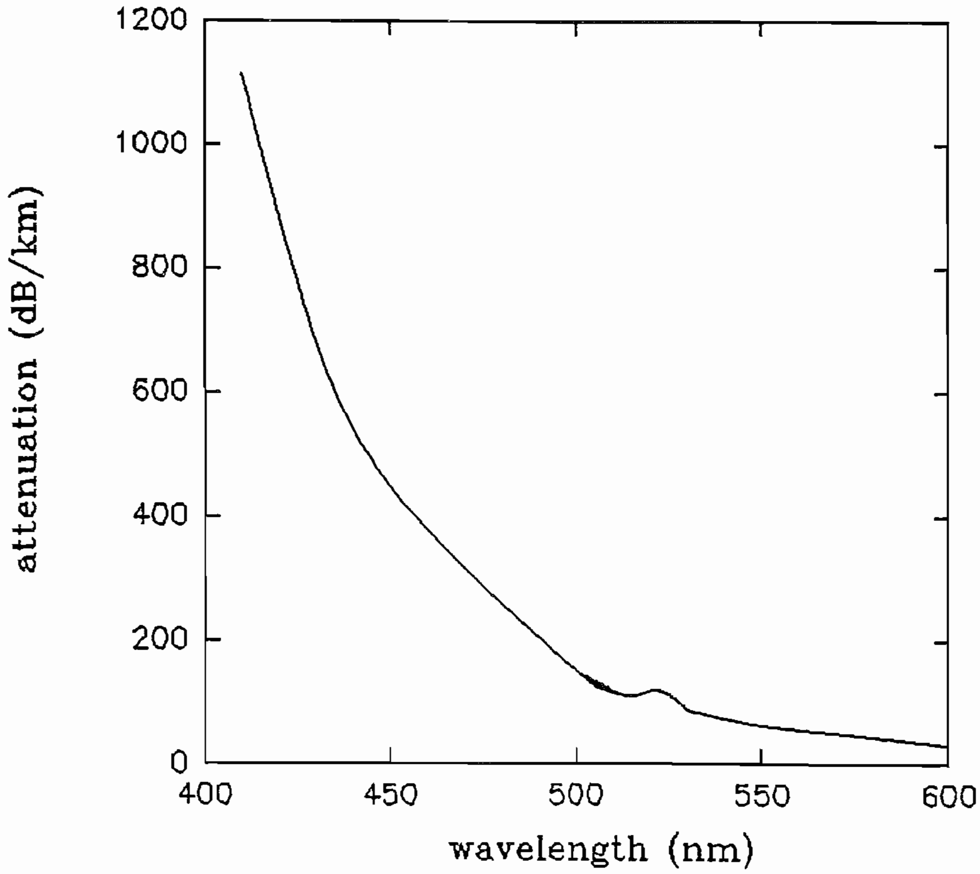

Figure 3.4 Spectral attenuation of a Mn^{2+}-doped fibre

associated with a near UV absorption band.

3.3.5 Bleaching of Fe^{2+} absorption

3.3.5.1 Background

Passively mode-locked fibre lasers are a very important area for generating short optical pulses for optical communications and information processing. Some nonlinear devices are used to this end. A saturable absorber is one of them, which shows a large loss at small signal levels but a smaller loss at large signal levels. Fe^{2+}-doped fibre has a strong absorption around 1100nm, which makes it ideal for a neodymium-doped fibre laser at 1.064μm if the loss

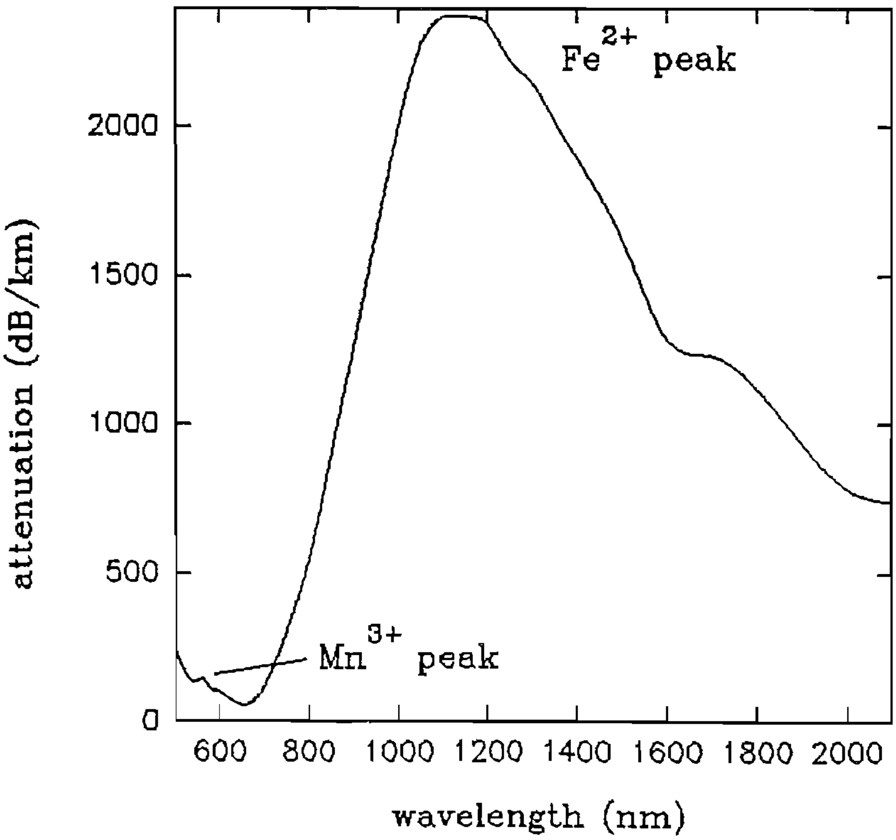

Figure 3.5 Spectral attenuation of a Mn^{3+}/Fe^{2+}-doped fibre

can be bleached out with low power light at 1.064μm and the recovery time is sufficiently fast. In this section, the possibility of Fe^{2+}-doped fibre to act as a saturable absorber in neodymium-doped fibre lasers is investigated. Experimental results on measuring the absorption bleaching with YAG laser pulses are also presented.

3.3.5.2 Theoretical outline

In a simple two-level system as depicted in figure 3.7, N_1 and N_2 are numbers of ions at ground and excited states respectively. B_{12}, B_{21} and A_{21} are the probabilities for stimulated absorption, stimulated emission and spontaneous emission respectively. $N^p(\nu)$ is the photon flux (photons/cm^2/s) at frequency ν. Thus we have

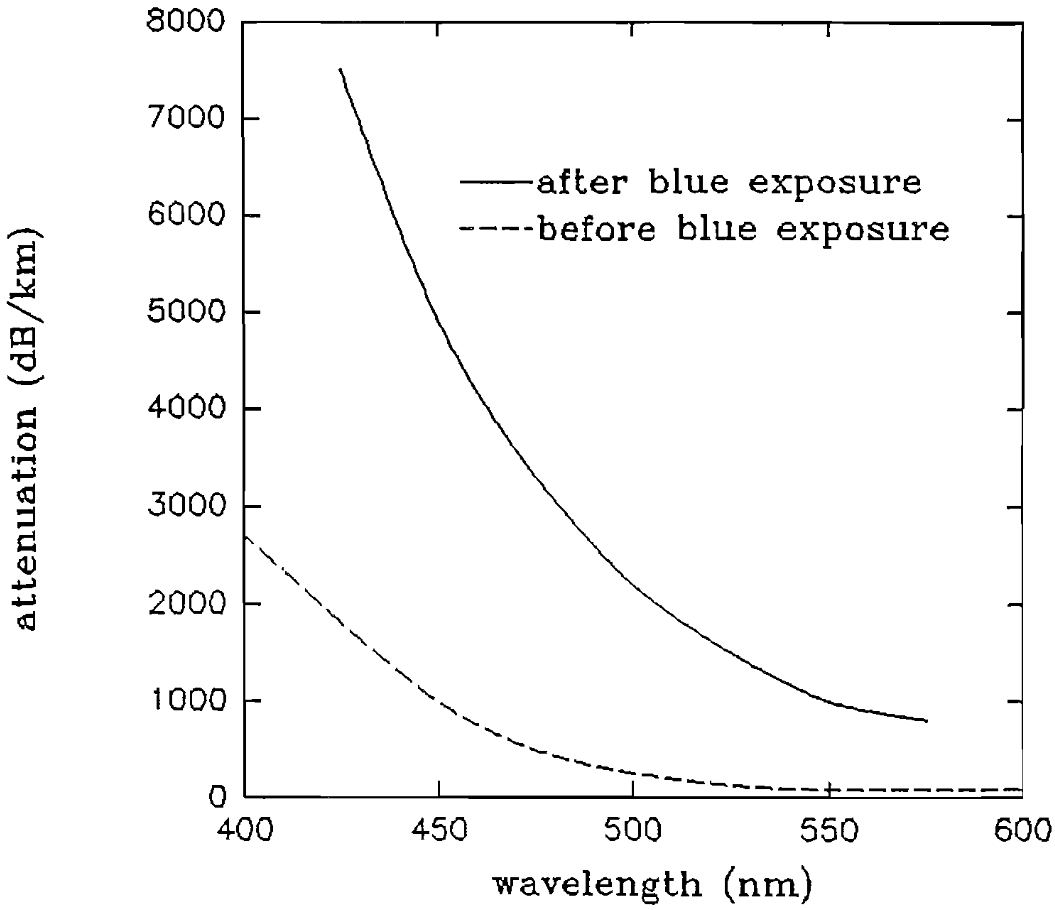

Figure 3.6 Spectral attenuations of a Fe^{3+}-doped fibre before and after blue exposure

$$B_{21} = B_{12} \tag{1}$$

$$\frac{dN_1}{dt} = -B_{12}N^p(\nu)\,(N_1-N_2) + N_2A_{21} \tag{2}$$

$$\frac{dN_2}{dt} = B_{12}N^p(\nu)\,(N_1-N_2) - N_2A_{21} \tag{3}$$

The following analytical solution can be obtained from equations 3.2 and 3.3:

$$\Delta N(t) = N_1(t) - N_2(t) = \frac{2B_{12}N^p(\nu)}{2B_{12}N^p(\nu)+A_{21}} e^{-(2B_{12}N^p(\nu)+A_{21})t} + \frac{A_{21}}{2B_{12}N^p(\nu)+A_{21}} \tag{4}$$

The solution contains two terms, a transient term and a

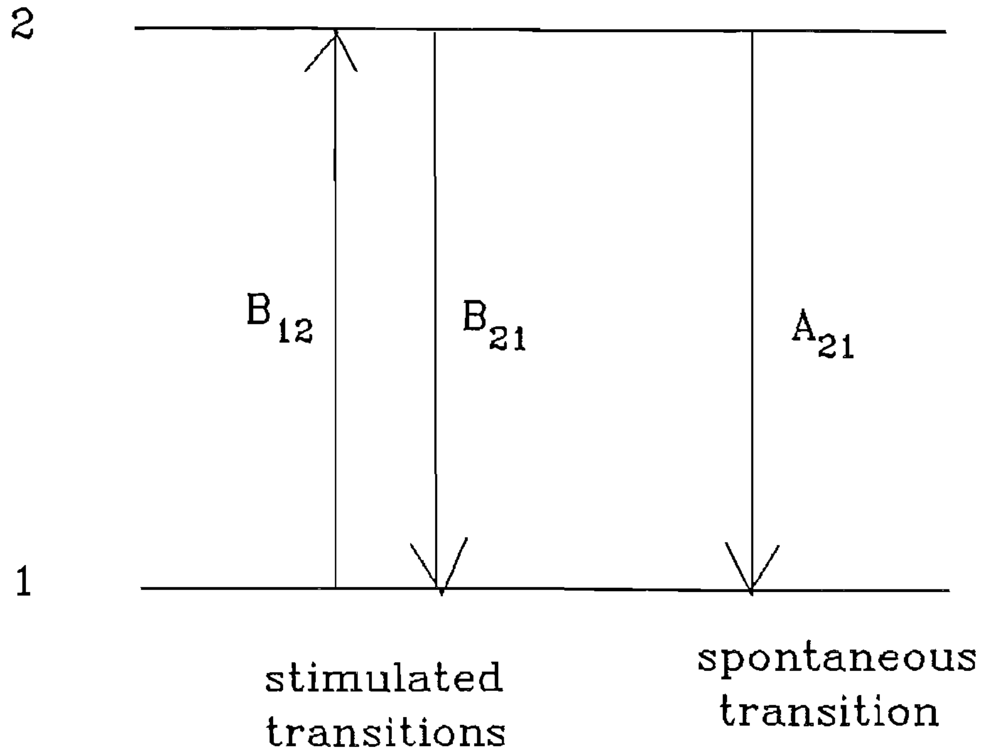

Figure 3.7 Energy states of a two-level system

steady-state term. If we define I_s as the photon flux to reduce the steady-state absorption by a factor of 2, then

$$I_s = \frac{A_{21}}{2B_{12}} \tag{5}$$

If thermal equilibrium is assumed and a normalised absorption line shape function, $g(\nu)$ (Hz^{-1}), is defined, we have

$$B_{21} = \frac{\lambda^2 A_{21}}{8\pi n^2} g(\nu) \tag{6}$$

where n is the refractive index of the medium and λ is the vacuum wavelength. The I_s becomes

$$I_s(\nu) = \frac{4\pi n^2}{\lambda^2 g(\nu)} \tag{7}$$

From the Fe^{2+} absorption curve in figure 3.5, we can estimate

$$g(1.060\mu m) = 5\times10^{-15} \quad (Hz^{-1})$$

Thus we obtain that I_s equals to 4.8×10^{23} photons/cm^2/s. If a core radius of 2.5μm is assumed, 18mW power is required.

3.3.5.3 Experiment

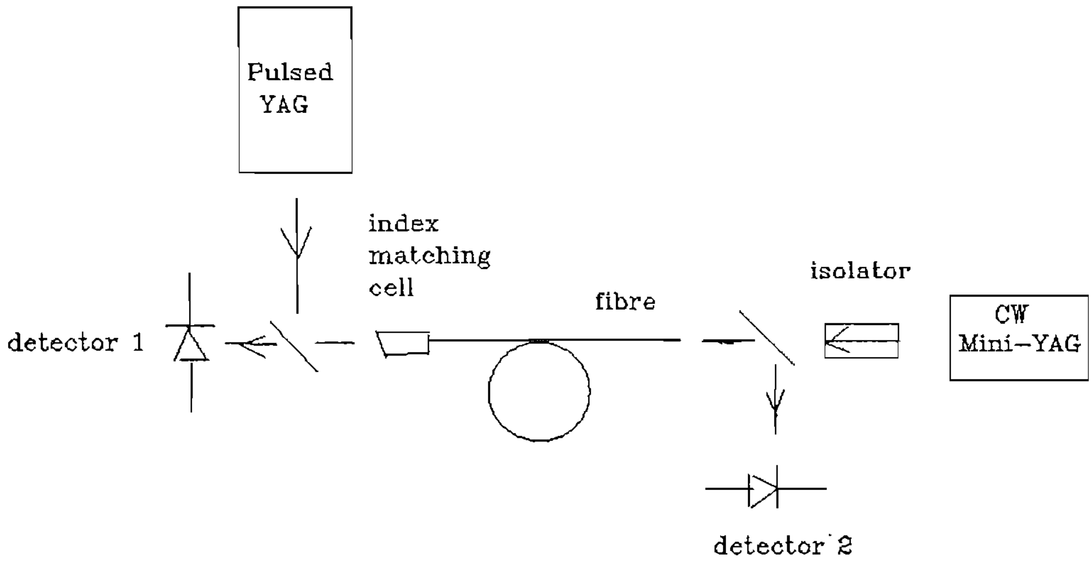

Figure 3.8 Experimental set-up for bleaching in a Fe^{2+}-doped fibre

The experimental set-up is shown in figure 3.8. A Q-switched YAG pump laser gives a train of 180ns pulses and was launched into a sample fibre through an index matching cell, containing index-matching fluid and having a front facet tilt at an angle to the input beam (not a normal incident angle). The purpose of the index-matching cell is

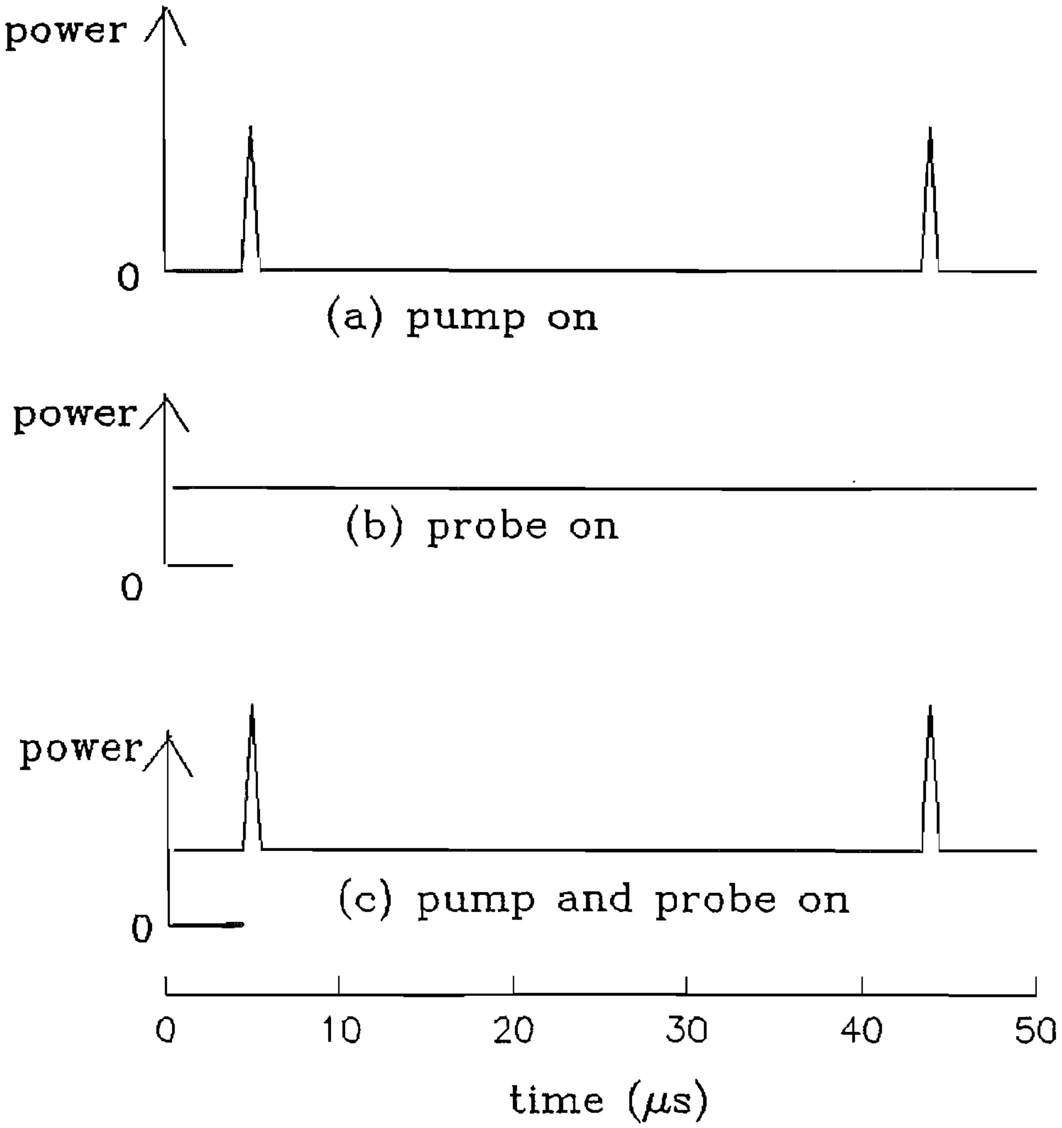

Figure 3.9 Measured signals on dectector 1

to reduce reflection at the detector. A CW mini-YAG was launched into the other end of the fibre and acts as a probe beam. An isolator was put in front of the CW YAG to stop the pump entering the probe YAG. The fibre has a core radius of about 2.5μm and length of about 1.9m. When a peak power of 238 watts was launched into the fibre, no sign of bleaching was observed. Figure 3.9(a) shows the signal at detector 1 while only the pump YAG was on; the pulses were from the reflections from the fibre ends. Figure 3.9(b) gives the signal when only the probe mini-YAG was on. Figure 3.9(c) is the signal when both pump and probe YAGs were on. No loss bleaching was observed.

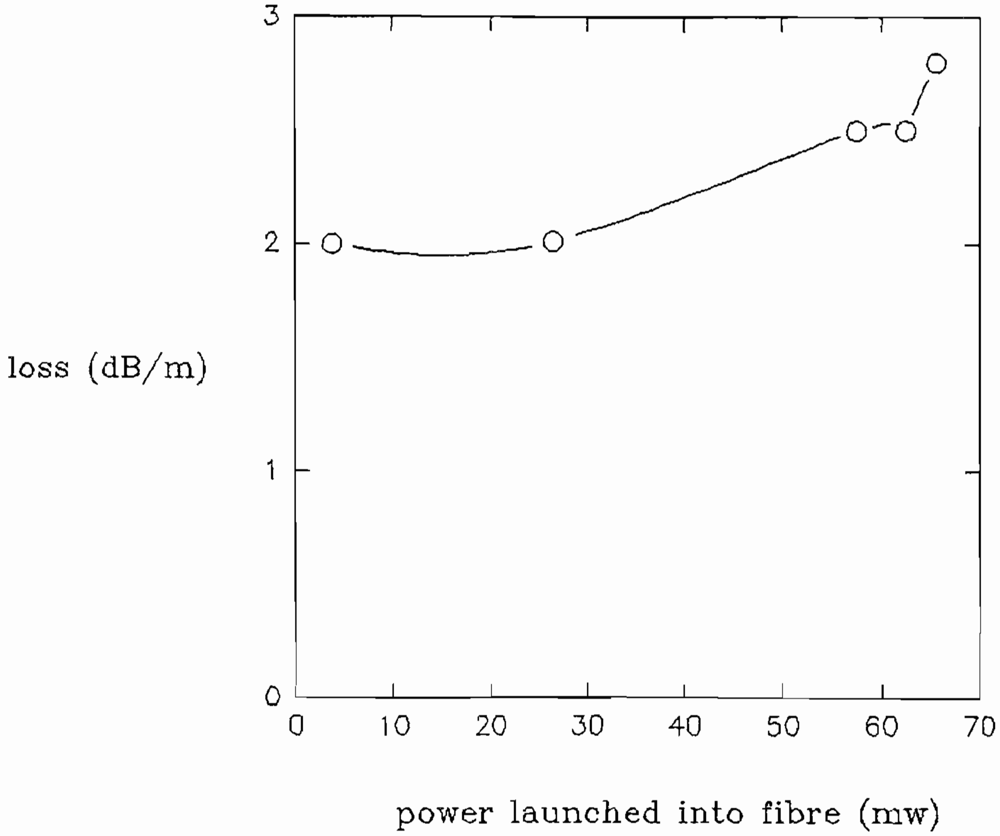

Figure 3.10 Loss at 1.064μm against power launched into a Fe^{2+}-doped fibre

CW YAG was also tested as pump, in which a CW YAG beam was launched into a 2.8m long fibre, the output was measured at various laser current settings and the fibre was then cut back to 0.6m long, the output was again measured with the same settings (the laser current setting was also tested to be reasonably repeatable). The loss was then calculated and plotted in figure 3.10. An increase trend with higher power is observed, without sign of bleaching for power up to 66mW. The loss increase with power level is believed to be caused by the onset of nonlinear effect (Raman and Brillouin effect) in the fibre.

3.3.6 Discussion

An increase of loss at near IR was observed when various transition-metal-doped fibres were subjected to CW argon of few hundred milliwatts. The effect may be attributed to the forming of defect centres in the fibres, which have been investigated in germanosilicate fibres[14,15]. No change of oxidation states in manganese-, iron-, copper-, and manganese/iron- doped fibres was observed with 30 minutes CW argon treatments of few hundred milliwatts.

238w peak power YAG laser has been launched into Fe^{2+}-doped fibre, and no change in the fibre transmission at 1.064μm was observed. CW pump up to 66mW was also tested without sign of bleaching. Higher bleaching threshold and very fast recovery is therefore speculated. The fast recovery process can be attributed to non-radiative decay process associated with phonon coupling in the glass, which has not been taken into account in the theoretical model, and the fact that Fe^{3+} is not a stable state in the glass.

3.4 Cerium-doped fibres

3.4.1 Background

The photosensitive response of optical fibres has been the focus of many researchers, primarily because of its potential for manufacturing efficient in-fibre gratings. In certain fibre cores, the axial index may be periodically perturbed by exposing to an interference pattern from a suitable laser[5,6], and the resultant gratings have many applications including single-mode fibre lasers, WDM telecommunications and fibre sensors. They have many advantages over their conventional bulk counterparts, being compact and easy to align, with low insertion losses. Such photo-induced index changes are well known in germanosilicate fibres on exposure to both blue (480nm) and UV (240nm) light[16,17,18]. Although the exact cause is still of a controversy, it is generally believed to be associated with germania. To increase the photosensitivity, more germanium should be incorporated into the fibre core, this will, of course, alter the fibre index profile. The aim of this research is to find an improved fibre for efficient fibre gratings, in which the photosensitive core dopant may be changed without altering the guiding properties of the fibre. It is known that other glasses suffer large absorption changes on exposure to certain wavelengths, including a cerium-doped sodium silicate glass, hence it seems likely that index change might be expected. The absorption changes induced in fibre cores composed of SiO_2, P_2O_5, Al_2O_3 and Ce_2O_3 on exposure to pulsed UV light at 266nm and 355nm was therefore investigated in section 3.4.4, and an index change of 1.4×10^{-4} was recorded at $1.064\mu m$, with the potential of further improvements with increased doping level as discussed in section 3.4.5.

3.4.2 Fabrication

The conventional MCVD method combined with the solution-doping method developed by Townsend et al[12] was used to fabricate the fibres.

Cerium ions can exist in two ionic valency states in a glass matrix, cerous (Ce^{3+}) and ceric (Ce^{4+}). The equilibrium between the two states depends very much on the basicity of the glass matrix and the glass preparation condition. A photo-induced absorption change in cerium-doped glasses has been attributed to Ce^{3+} ions in the glass[19,20], which are photoionised to form Ce^{4+} ions on UV exposure. P_2O_5 and Al_2O_3 were therefore used as co-dopants to favour the formation of the Ce^{3+} instead of the Ce^{4+} state[21]. A SiO_2/P_2O_5 layer deposited at a relatively low temperature (about 1300°C) on the inside of a silica tube was solution-doped with $AlCl_3.6H_2O$ and $CeCl_3.7H_2O$, using water as a solvent. Four fibre preforms were made in this way with similar $AlCl_3.6H_2O$ concentrations but different $CeCl_3.7H_2O$ concentrations to vary the Ce^{3+}-doping level; one having no $CeCl_3.6H_2O$ to clarify the effect of alumina. The soaking time in each case was 1 hour, and the preforms were subsequently dried by heating up to 600°C for 1 hour. Nitrogen instead of the usual oxygen was used in the following collapse process to further encourage the formation of Ce^{3+} ions.

3.4.3 Characterisation

Table 3.1 Preform parameters

preform number	1	2	3	4
NA	0.13	0.19	0.18	0.17
Ce^{3+} (ppm)	11700	5800	1900	0
P_2O_5 (mol%)	12	23	22	21
$Al_2Cl_3.6H_2O$ in solution (M)	3.62	2.49	2.49	3.77

The parameters of the resultant preforms are listed in table 3.1. The P_2O_5 concentration was estimated by using the data given by Hammond et al[22]. The absorption spectra are shown in figure 3.11, measured with Perkin-Elmer Recording Spectrophotometer of the type EPS-ST with polished thin slices of preform (180 to 480μm thick) because of the high loss. A small aperture ensured that

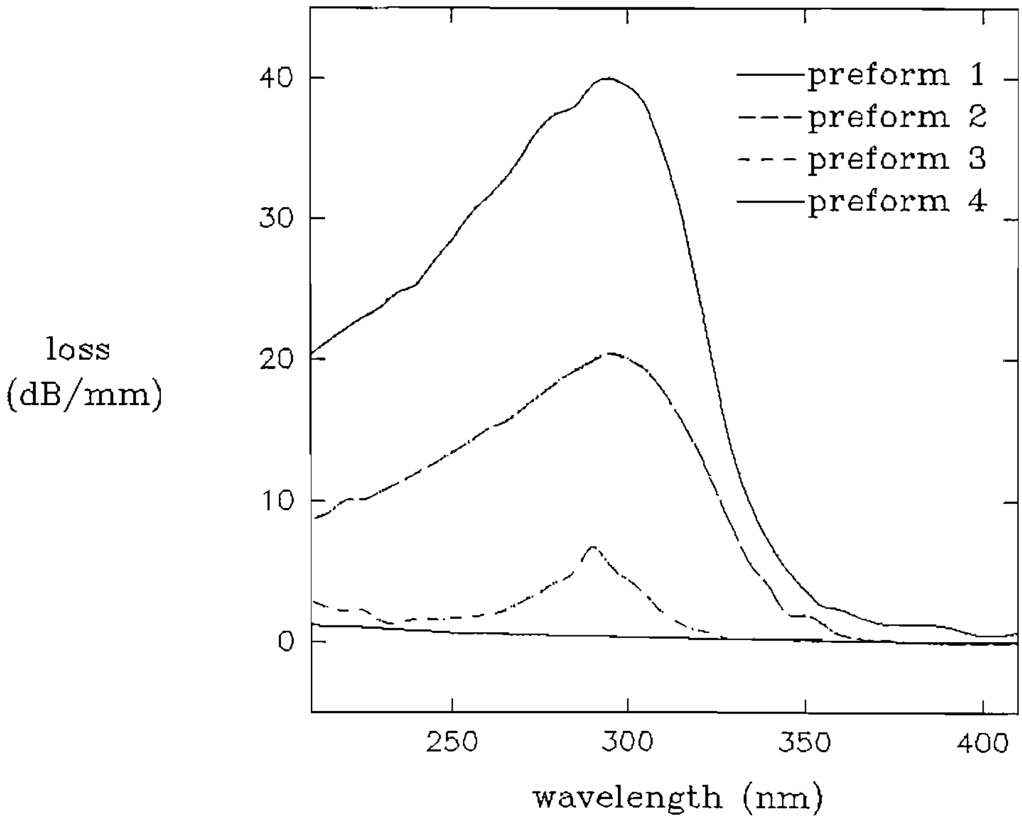

Figure 3.11 Absorption spectrum of Ce^{3+}–doped preforms

light could only pass through the preform core region, and the collimated beam of the spectrophotometer was focused down to a size slightly larger than the aperture to improve sensitivity. The insertion loss were corrected for by comparing with data measured at 600nm in a fibre drawn from the same preform using a cut-back technique. The error in these measurements is less than ±1dB/m.

The Ce^{3+} ion has a 4f-5d electric dipole transition with a corresponding absorption peak, the position of which is highly dependent on the glass composition. In similar glasses, it has been centred in the 276-306nm region. The Ce^{4+} ion, meanwhile, has a charge transfer band, which should appear as a peak at a slightly shorter wavelength. Only a single peak in the absorption spectrum is observed, however, in figure 3.11, and this is confirmed to be due to Ce^{3+} ions by the observation of strong fluorescence centred at 420nm, a Ce^{3+} characteristic. In the absence of any significant additional Ce^{4+} peak, it is assumed that most of the cerium ions must be in the Ce^{3+} state. The concentration is determined by comparison with Ce^{3+} absorption data given by Laczka et al[23] for a glass composed of SiO_2+0.05Al_2O_3, giving 11,700ppm, 5,800ppm, and 1,900ppm for preforms 1, 2, and 3 respectively (±300ppm in each case due to loss measurement error). The additional rising trend at short wavelengths in preforms 3 and 4 is attributed to the UV edge of the glass, which is not visible in heavily doped preforms 1 and 2, because of the dominant Ce^{3+} peak. The relationship between this dopant level and the $CeCl_3.7H_2O$ solution concentrations is shown in figure 3.12. It is found to be linear without any sign of insolubility and devitrification, indicating the possibility of producing preforms with a higher Ce^{3+} dopant level. All the fibres drawn from the Cerium-doped preform have a relatively low loss of about 150dB/km at the important communication wavelength of 1.55μm.

3.4.4 UV-induced loss change

Changes in absorption spectrum of preform 2 on exposure to pulsed 266nm radiation from a frequency-quadrupled YAG laser (pulse width 8-9ns, 30Hz repetition rate, and average intensity of 4kW/m^2) for 1 minute are shown in figure 3.13. Curve 1 is the original loss spectrum, while curve 2 was measured 10 minutes after exposure, curve 3 109 hours after and curve 4 82.2 days after. It can be seen on the curve 2 that the Ce^{3+} absorption peak at 290nm has been reduced on UV exposure, indicating a reduction of Ce^{3+} concentration. A broad absorption band extending over both sides of the Ce^{3+} peak has appeared, and may be attributed to photo-

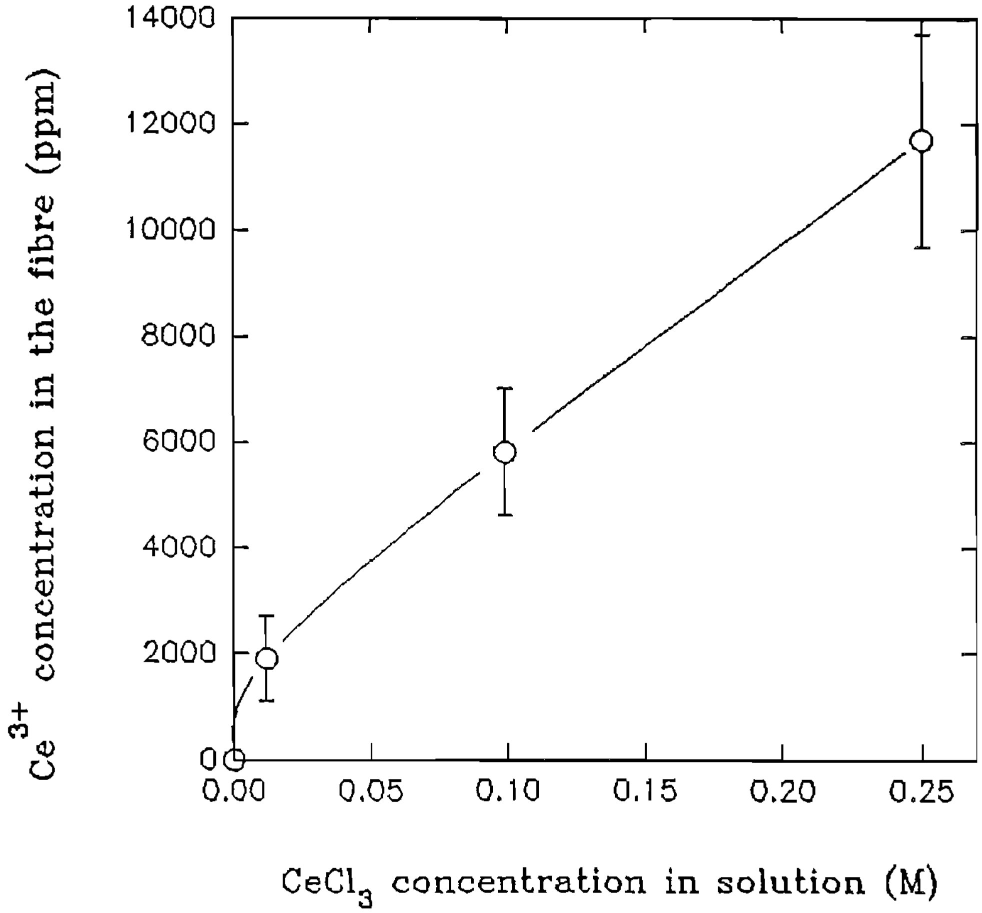

Figure 3.12 Relationship between Ce^{3+} levels in the fibres and solution concentrations.

electrons trapped at various defect-centres. This induced broad band shows signs of recovering in curve 3, with total recovery by curve 4. The reduction in the Ce^{3+} peak remains, however, even after 82 days (curve 4) and the anticipated Ce^{4+} absorption band resulting from Ce^{3+} ions losing electrons can be also seen around 245nm.

The recovery process of the broad band loss was further investigated at 632.8nm in a fibre drawn from the preform, with single-mode operation below 590nm and an intrinsic loss of 200dB/km at 632.8nm. The fibre was laterally exposed to 266nm light with an average intensity of $4mW/\mu m^2$. while probing with 632.8nm light propagating through the fibre. On exposure, the fibre loss increased almost immediately to a very high level and stabilised at that

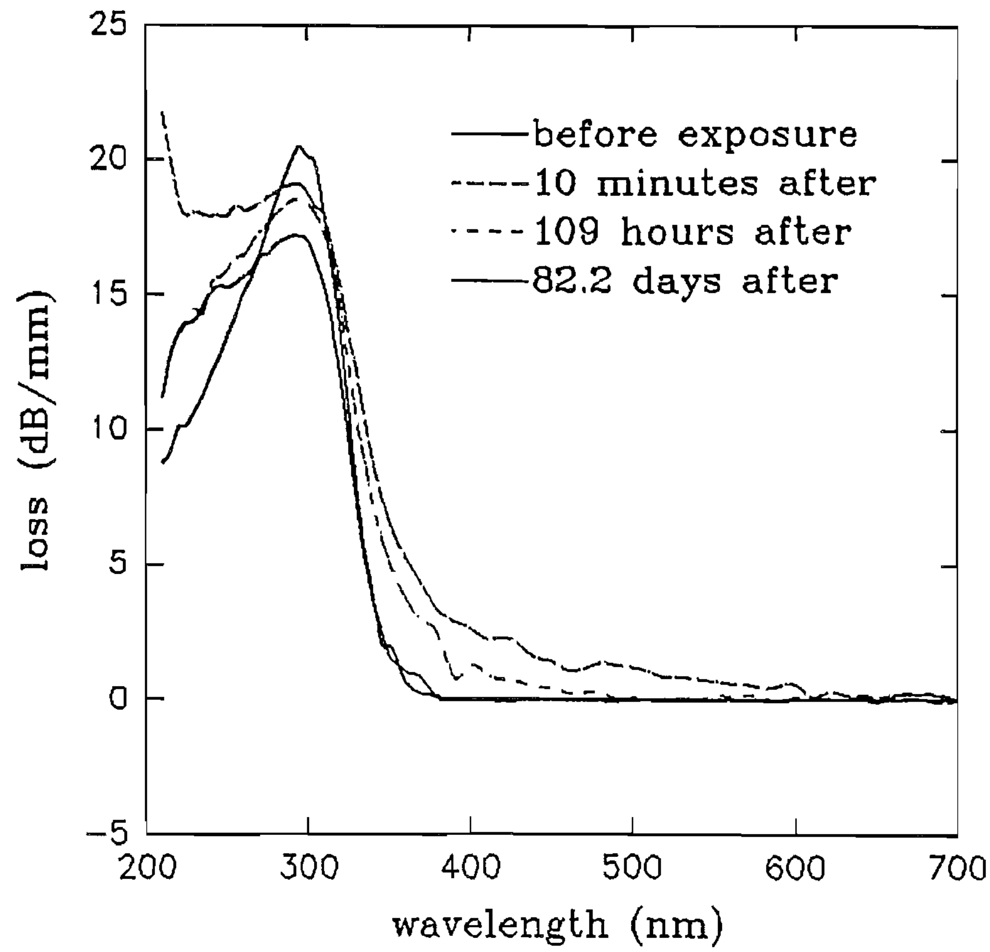

Figure 3.13 Absorption spectrum of preform 2 before and after UV exposure

level provided the UV intensity remained constant (figure 3.14). This loss was found to be linear with UV intensity, indicating a single-photon process (figure 3.15). The loss mentioned here and in the following text is the actual material loss calculated by taking into consideration of only a fraction of light propagates in the fibre core. Figure 3.14 also shows the principle of a modulator, where fibre transmission at 632.8nm is controlled by light at 266nm. The speed of the modulator is limited by the recovery speed of the process, which may be improved in a different glass host. On blocking UV, a reversal of the loss was observed, as shown in figure 3.16. After seven hours, the loss had dropped to 8.3% of its original value. Also shown in the figure is a good fit to the data; the summation of three exponential decays,

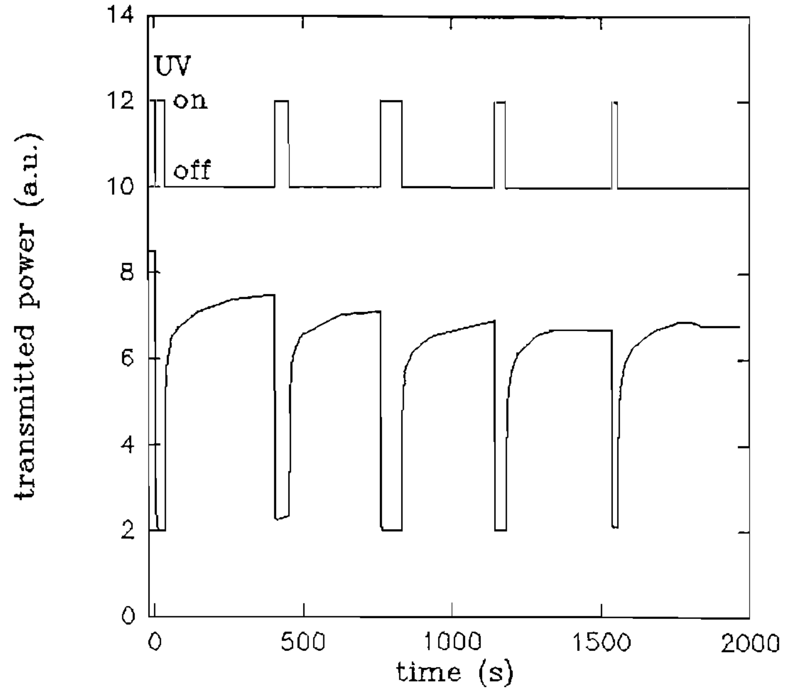

Figure 3.14 The effect of UV radiation at 266nm (4mW/μm^2) on the transmission of a Ce^{3+}-doped fibre (5800ppm) at 632.8nm.

$$\sum_{1}^{3} A_i e^{-\alpha_i t}$$

where A_1 =0.586, A_2=0.0955, A_3=0.129, α_1=0.0291, α_2=0.00210, and α_3=0.0000213. Three different processes are therefore involved with time constants of 34s, 8mins, and 13hrs respectively, indicating that different types of defect centre are formed. The induced losses measured during UV exposure of 4μW/μm^2 in fibres drawn from the other three preforms are plotted for comparison in figure 3.17. As expected, no induced loss was observed in the fibre doped only with alumina, indicating that the mechanism is Ce-related. There is, however, a significant reduction in loss at high concentrations. The induced loss measured 4

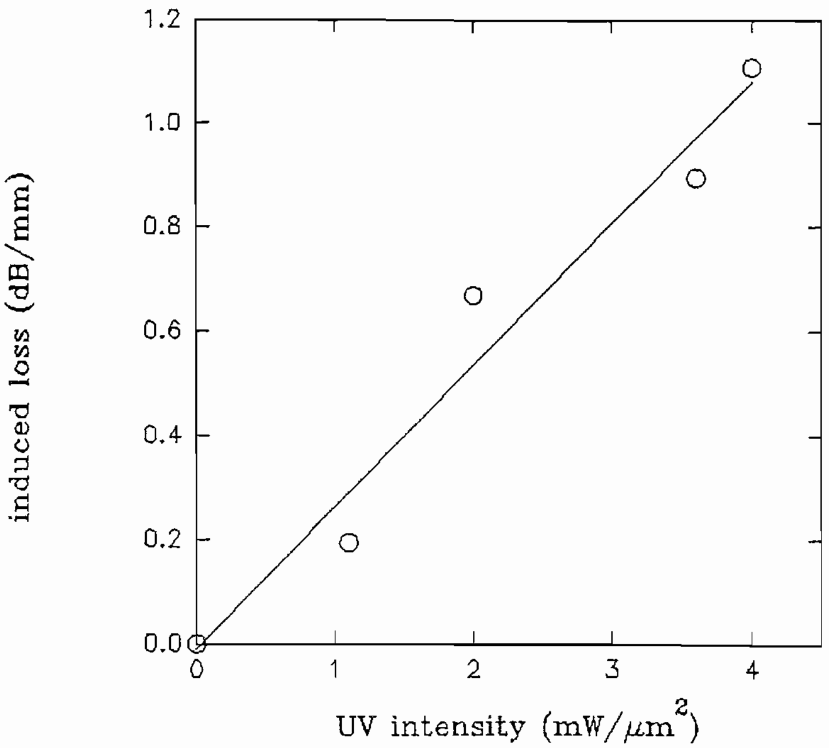

Figure 3.15 UV intensity dependence of the induced loss at 632.8nm in a fibre containing 5,800ppm Ce^{3+} ions

hours after exposure of $4\mu W/\mu m^2$ at the important fibre communication window, $1.55\mu m$, was found to be only 3.1dB/m. negligible for typical fibre grating lengths (1cm long).

Fibres were also exposed to pulsed 355nm light from a frequency-tripled YAG laser. Similar changes in absorption were noted, but 19 times the average intensity was required for these to be of identical magnitude. This is not surprising, given that the Ce^{3+} absorption strength at this wavelength is only one 15th of that at 266nm.

3.4.5 UV-induced index change

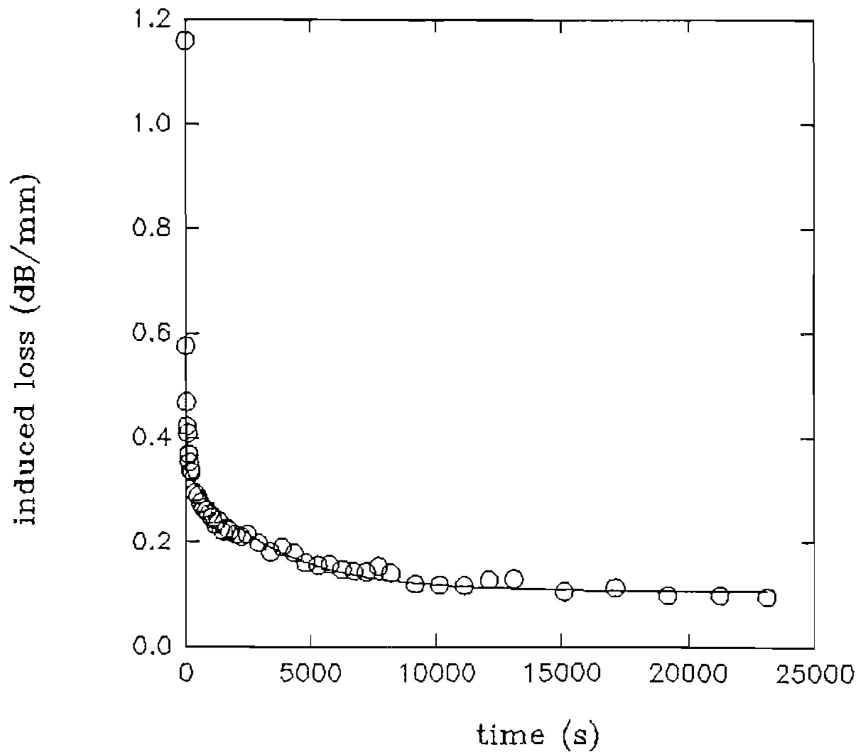

Figure 3.16 Loss recovery process in a fibre doped with 5,800ppm Ce^{3+} ions after being exposed to UV light of $4mW/\mu m^2$.

In order to produce a reliable and repeatable technique for measuring refractive index change, four dual-core preforms were fabricated, each containing one phosphosilicate core and a core from each of the four preforms. These dual-core preforms were numbered 1, 2, 3, and 4, containing in the appropriate core 11,700ppm, 5,800ppm, 1,900ppm, and 0ppm Ce^{3+} ions respectively, and the fibres drawn from each are referred to as TC4, TC5, TC6 and TC7. Three fibres with different diameters were drawn in each case to give single-mode operation over a wide range of probe wavelengths. In all fibres, the cores are sufficiently spaced to preclude any significant coupling between them.

The experimental arrangement used to measure the index change is depicted in figure 3.18. A probe beam is weakly

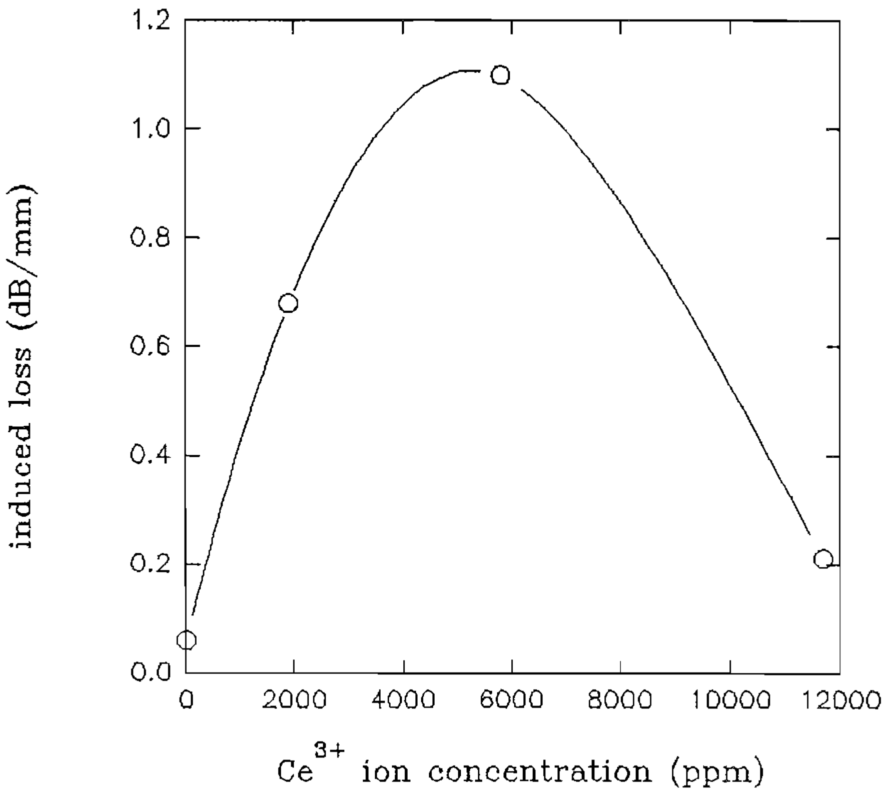

Figure 3.17 Ce^{3+} concentration dependence of induced fibre loss at 632.8nm during UV exposure of $4mW/\mu m^2$

focused onto a cleaved end of the test dual-core fibre, launching equal intensity into both cores. At the far end of the fibre, the two cores act as point sources a few microns apart, with the transmitted light interfering to give large fringes in the far field. The lateral position of these fringes depends on the optical path length difference between the light propagating in the two cores, and so a change in index in only one core will cause fringe movement. A narrow slit is placed in this fringe pattern, allowing only a very small part of a fringe to be transmitted onto a photodiode and monitored on a chart recorder. A coating-stripped section of this fibre is then laterally exposed to pulsed 266nm UV light. Previous experiments have demonstrated that no index change occurs in the pure phosphosilicate core, so any fringe movement

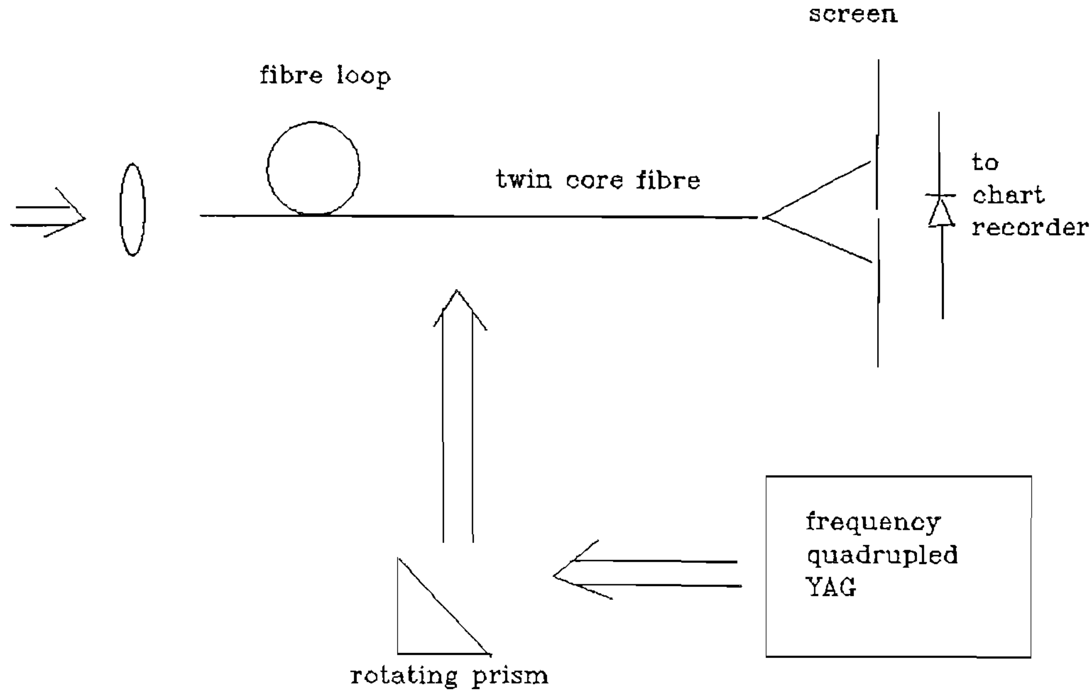

Figure 3.18 Experimental set-up for measuring UV-induced index change

which occurs on exposure must simply be as a result of an index change in the cerium-doped core. The best measurement accuracy can be achieved by exposing a long length of fibre, but this is limited, particularly at shorter wavelengths, by the UV-induced loss which has the effect of reducing fringe contrast. Lengths between 5cm and 15cm were therefore exposed, by repeatedly scanning the beam along the fibre until the fringe position stabilised, typically after 1 minute. The fringes were found to be stable for at least 30 minutes after UV exposure, dissociating the index change mechanism from the fast recovery process of the induced loss at IR. The core material refractive index change could then be calculated from the number of fringes shifted and the exposed fibre length by taking into account the fact that only a proportion of the optical power propagates in the fibre cores.

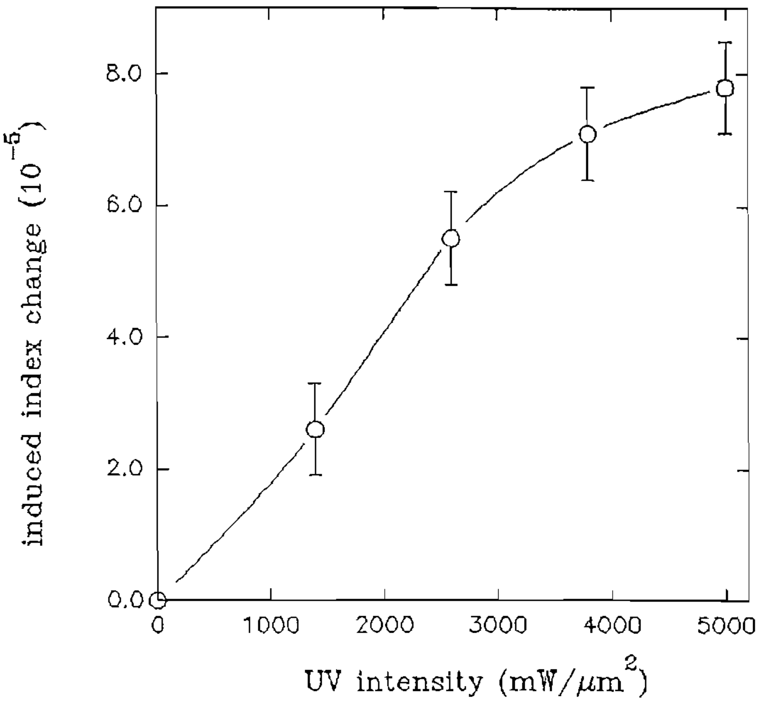

Figure 3.19 UV intensity dependence of induced index change at 784nm in a fibre doped with 5,800ppm Ce^{3+} ions

The variation of refractive index change in TC5 with average UV intensity was investigated at 784nm and the result is shown in figure 3.19. The curve shows a near linear response at low average UV intensities, indicating that the index change mechanism is dependent on a single-photon process, but a saturation trend appears above $4\mu W/\mu m^2$. The dependence of the induced index change on Ce^{3+} concentrations was also measured at $1.064\mu m$ using fibres from the four different preforms. The results are shown in figure 3.20 for an average UV intensity of $4\mu W/\mu m^2$. As expected no index change was seen in TC7, in which the core is doped only with Al_2O_3, demonstrating that Ce^{3+} is

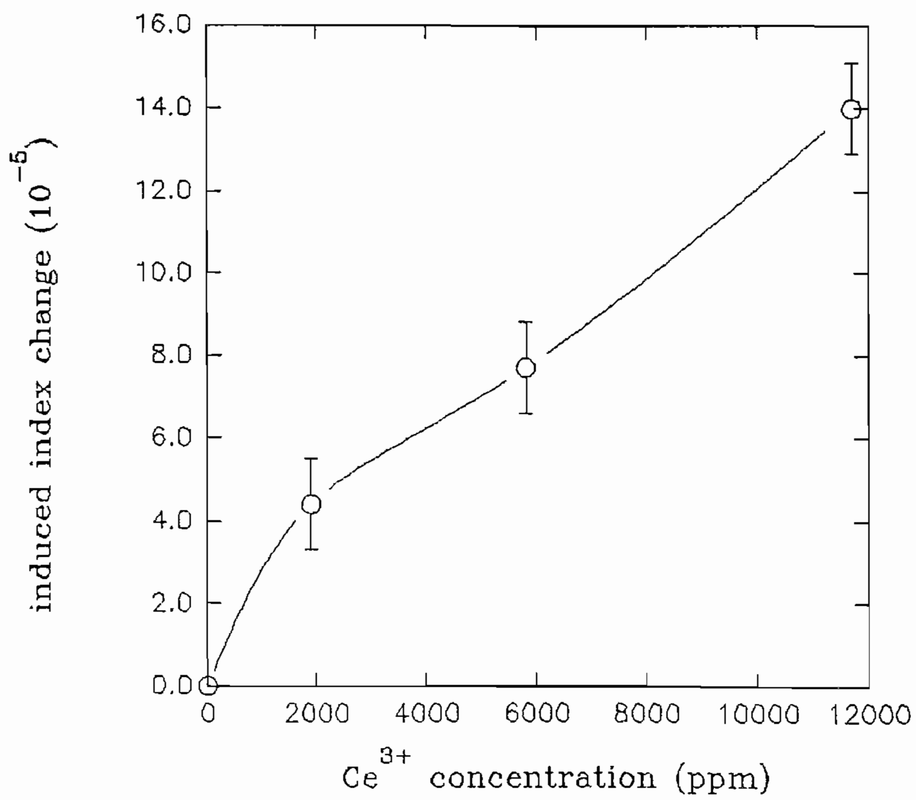

Figure 3.20 Ce^{3+} concentration dependence of UV–induced index change at 1.064μm with UV light of 4mW/μm^2

necessary for the refractive index change. The index change appears to be a near linear function of Ce^{3+} concentration.

The wavelength dependence of the induced index change was investigated by comparing measurements in TC5 at 632.8nm (Helium-Neon laser) and 1550nm (laser diode) with those already made at 784nm and 1.064μm for the average UV intensity of 4μW/μm^2, as shown in figure 3.21. In contrast to the low dispersion observed with germanosilicate fibres, however, a drop in the induced index change with increasing wavelength was observed. Despite this, though, the index change at the important communication wavelength of 1.55μm is still 6.8×10^{-5}, large enough to give a 90% efficiency reflection if induced periodically over a length of 13mm.

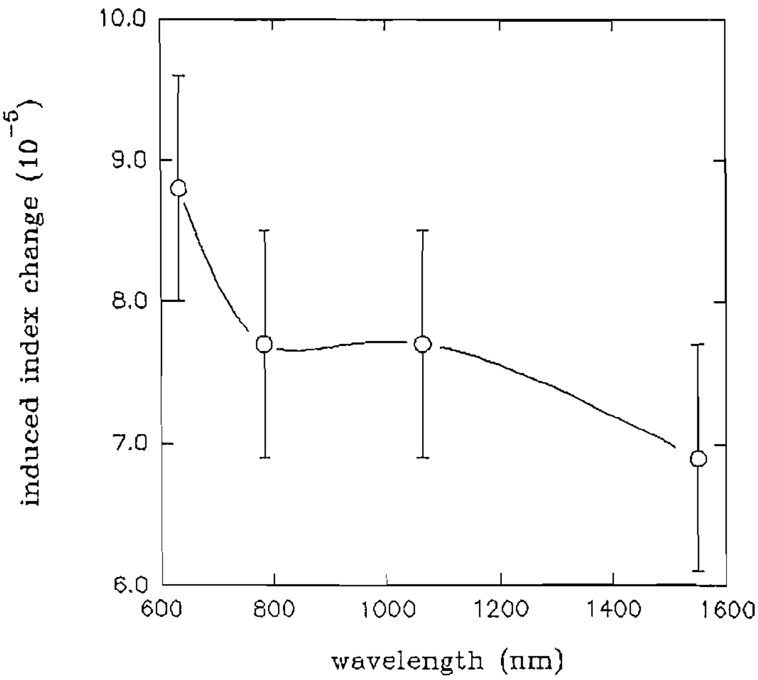

Figure 3.21 Wavelength dependence of UV-induced index change with UV light of $4mW/\mu m^2$ in a fibre doped with 5,800ppm Ce^{3+} ions

Pulsed 355nm light was found to produce an equivalent effect, but required an average intensity greater by a factor of 4.

3.4.6 Discussion

To summarise, a UV-induced absorption change in a selection of Ce^{3+}-doped glass preforms and fibres has been studied. The Ce^{3+} ion concentration is reduced and a broad absorption band extending up to IR created on UV exposure. 82 days after exposure, the change in Ce^{3+} concentration remained, but the induced broad band absorption had totally recovered. Further investigation revealed three distinct recovery time constants in the order of tens of seconds, a few minutes and a few hours. This induced broad absorption band is attributed to defect centres formed by trapping photoelectrons released by Ce^{3+} ions. The anticipated Ce^{4+} absorption peak resulting from Ce^{3+} ions losing electrons, observed by Stroud[19], was also seen. The UV-induced loss at 632.8nm during UV exposure was found to stay at a constant level and depend linearly on average UV intensity. This loss was also observed to increase with Ce^{3+} ion concentration for low concentration levels, but to decrease at higher levels. 355nm light was also found to give a similar absorption changes at 632.8nm but required an average intensity of 19 times that of the 266nm.

Large average index changes are also induced in Ce^{3+}-doped optical fibres on exposure to pulsed 266nm UV light. A linear dependence on UV intensity indicates a single-photon process. The fact that the index change is stable for at least 30 minutes after exposure disassociates it from the fast recovery loss process. Similar effects are seen with 355nm but the required average intensity is four times higher; however this is much less than that required to obtain the same induced loss at 632.8nm (19 times), providing additional evidence for two different mechanisms. The saturation trend of the UV intensity dependence may be explained by a lack of electron-trapping centres associated with the index change mechanism, indicating that an increased index change is achievable if this defect centre concentration can be increased, probably by higher Al^{3+} doping level. The index change that results from the induced absorption change, estimated by Kramers-Kronig relation, are an order of magnitude too small. A precise calculation has not been possible due to unknown absorption line shapes due to insufficient data.

3.5 Summary

In this chapter, photosensitivity in two kinds of fibres was investigated. In transition-metal-doped fibres, the effect of CW argon laser (488nm) was investigated. No change of ionisation states was observed in the fibres tested. Higher energy radiation is apparently needed. Instead, a creation of defect centres was observed, which causes a significant increase in the visible and near IR absorption. Photo bleaching in Fe^{2+}-doped fibre with YAG laser was also tested. When CW photon fluxes greater than those predicted by equation 3.7 was launched into fibre, there was no sign of bleaching. Pulsed YAG with much higher power was also tested, without success. The bleaching is believed to happen at higher power levels than predicted and have a very fast recovery time.

The research in Ce^{3+}-doped fibre shows that fibre index changes by about 10^{-4} when exposed to UV light at 266nm and 355nm. This effect can be used to write gratings in the fibre core, which is of great importance in single-frequency fibre lasers, WDM telecommunications and fibre sensors. The effect is identified as a single-photon process and to be Ce^{3+}-related. A broad absorption band from UV to IR is also induced in this fibre, and a slow modulator is demonstrated with this effect, in which light at IR was switched on and off by another light source at UV.

References

1 L.D. Pye, H.J. Stevens, and W.C. LaCourse: "Introduction to glass science", Plenum Press, 1972.

2 G.H. Brown: "Photochromism", Jhon Wiley&Sons, 1971.

3 P. Balta and E. Balta: "Introduction to the physical chemistry of the vitreous state", Abacus Press, 1976.

4 A.J. Cohen and H.L. Smith: "Variable transmission of silicate glass sensitive to sunlight", Science, **137**, 1962, pp.981.

5 K.O. Hill, Y. Fujii, D.C. Johnson, and B.S. Kawasaki: "Photosensitivity in optical fibre waveguides: application to reflection filter fabrication", Applied Physics Letters, **32**, 1978, pp.47-649.

6 G. Meltz, W.W. Morey, and W.H. Glenn:"Formation of Bragg gratings in optical fibres by a transverse holographic method", Optics Letters, **14**, 1989, pp.823-825.

7 W.A. Weyl: "Coloured glass", Dawsons of Pall Mall, London, 1959.

8 T. Bates: "Modern aspects of the vitreous state", Betterworths, Washington, 1962.

9 H.L. Smith and A.J. Cohen: "Absorption spectra of cations in alkali silicate glasses of high ultra violet transmission, Physics and Chemistry of Glasses, **4[5]**, 1963.

10 G. Kordas and H.J. Oel: "Electron spin resonance studies of radiation-induced damage in iron silicate glasses", Physics and Chemistry of Glasses, **25**, 1984, pp.76-81.

11 C.R. Kurkjian and E.A. Sigety: "Coordination of Fe^{3+} in glass", Physics and Chemistry of Glasses, **9[3]**, 1968.

12 J.E. Twonsend, S.B. Poole and D.N. Payne: "Solution-doping technique for fabrication of rare-earth-doped

optical fibres", Electronics Letters, **23**, 1987, pp.329-331.

13 P.C. Schultz: "Optical absorption of the transition elements in vitreous silica", Journal of the American Ceramic Society, **57**, 1974, pp.309-313.

14 L.J. Poynze-Wright, M.E. Fermann and P.St.J. Russell: "Nonlinear transmission and colour-centre dynamics in germanosilicate fibres at 420-540nm", Optics Letters, **13**, 1988, pp.1023-1025.

15 L.J. Poyntz-Wright and P.St.J. Russell: "Two-photo-induced losses in germanosilicate optical fibres: relaxation processes", Conference on Laser and Electro-optics, June 1989, TUG3.

16 M.A. Saifi, Y. Silberberg, A.M. Weiner, H. Fouckhardt, and M.J. Andrejco: "Sensitivity of two core fibre coupling to light-induced defects", IEEE Photonics Technology Letters, **1**, 1989, pp.386-388.

17 D.P. Hand and P.St.J. Russell: "Photo-induced refractive-index changes in germanosilicate fibres", Optics Letters, **15**, 1990, pp.102-104.

18 B. Malo, K.A. Vineberg, F. Bilodeau, J.Abert, D.C. Johnson, and K.O. Hill: "Ultraviolet light photosensitivity in Ge-doped silica fibres: wavelength dependence of the light-induced index change", Optics Letters, **15**, 1990, p.953-955.

19 J.S. Stroud: "Photoionization of Ce^{3+} in glass", The Journal of Chemical Physics, **35**, 1961, pp.844-850.

20 W.W. Wargin and G.O. Karapetjan: "Photosensitive glass", Ind. Eng. Chem., **41**, 1949, pp.856-861.

21 Y. Ishii, K. Arai, H. Namikawa, M. Tanaka, A. Negishi, and T. handa: "Preparation of cerium-activated silica glasses: phosphorous and aluminium codoping effects on absorption and fluorescence properties", Journal of the American Ceramic Society, **70**, 1987, pp.2-77.

22 C.R. Hammond and S.R. Norman: "Silica based binary glass system refractive index behaviour and composition in optical fibres", Optical and Quantum Electronics, **9**, 1977, pp.399-409.

23 M. Laczka and L. Stoch: "Synthesis, structure and electron spectra of fused quartz doped with titanium, cerium and neodymium", Glastech. Ber., **61**, 1988, pp.218-222.

Chapter Four Specially Structured Fibres

4.1 Introduction

Fibres with special built-in structures have played very important roles in fibre devices for communications and sensors. Fibres with metal rods implanted parallel to the core enable interaction between the metal surface and light propagating in the core through the evanescent field, permitting the realisation of a fibre polariser[1,2]. Fibres containing two metal electrodes adjacent to the core enable the application of very high electrical fields across the fibre core over a long fibre length, to align defect centres in second harmonic generation and to modulate the optical phase in a fibre modulator[3,4]. Other specially structured fibres include ones with two guided structures, one inside the other. The outer waveguide has a rectangular shape and thus can couple, with high efficiency, from a high power laser diode array of a rectangular shape. The inner waveguide is doped with lasing ions and forms a laser cavity. The high power in the outer waveguide is used to pump the lasing ions in the inner waveguide to produce a much needed high power fibre laser.

In this chapter, we discuss the fabrication of these specially structured fibres. Liquid-metal implanted fibres are discussed first, and then the gold-implanted fibre. Fibres for cladding pumping are described at end of the chapter.

4.2 Liquid-metal-implanted fibres

4.2.1 Background

As we already mentioned in the introduction, the application of a strong electrical field over a long length of fibre enables the small electro-optic effect in silica glass to be utilised to make optical modulators and also alignment of light-induced asymmetrical defect centres in excitation poling of second harmonic generation[3,4]. To this end, it is necessary to place the two electrodes very close to each other at two sides of the core. If metal electrodes are inserted into a fibre preform and the preform is then drawn into a fibre, a good match of thermal properties between the metal and silica fibre is required. A liquid-metal filling technique is thus used, in which a fibre is drawn with holes in the place of the electrodes and liquid metal is subsequently pumped into the holes to form continuous electrodes. The hole surface is fire-polished during fibre drawing, ensuring a smooth electrode surface. This is proved later to be crucial in application of high voltage to the electrodes, which is chiefly limited by breaking down at a rough electrode surface.

4.2.2 Design of fibres

Fibres with two different designs were made as shown figure 4.1, the fibre with two holes has the advantage of having a shorter distance between the two electrodes. The one with a flat surface has the obvious advantage of cutting off half of the tedious process of filling a hole with liquid metal and connecting a power supply to it. The distance between two electrodes is ideally small; however this is limited by the difficulty of maintaining the shape of the fibre during fibre pulling at a temperature above

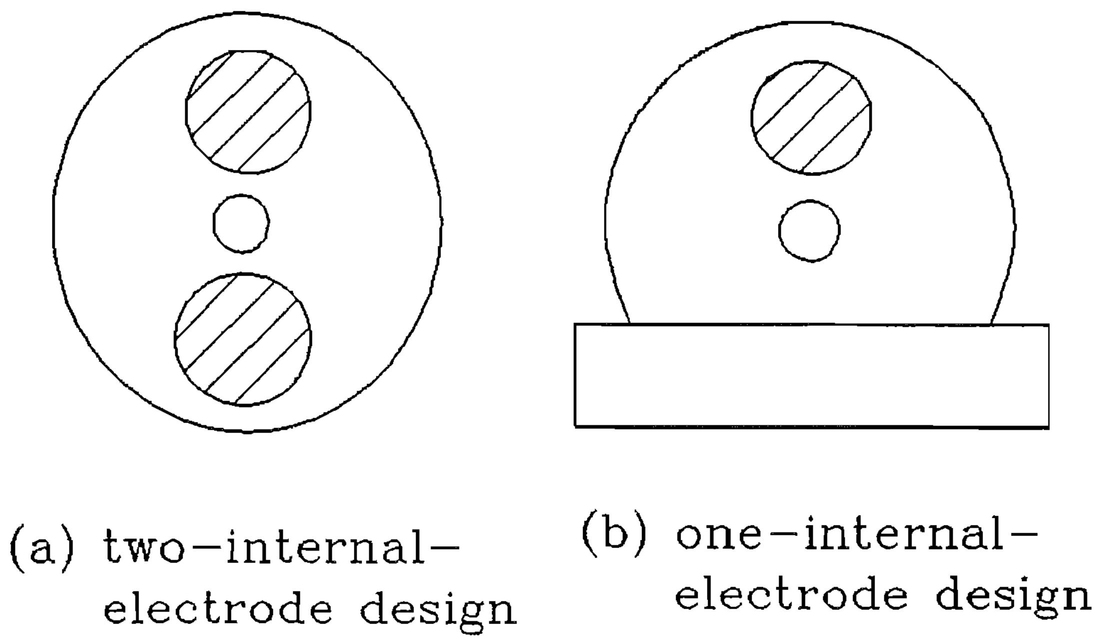

Figure 4.1 Electroded fibre designs

1950°C. The holes should be large enough to ease the liquid metal filling and also be much larger than the core to ensure an even distribution of electric field across the fibre core. Gallium is usually used as the liquid metal, because it gives a good conductivity and has a low melting temperature of 29.78°C.

4.2.3 Fabrication

MCVD preforms of suitable NA are used as starting preforms. They are machined on an ultrasonic glass mill. The hole diameter and position are determined by scaling up the fibre dimensions. Holes are then drilled and a flat surface is milled in the case of the design with a flat electrode. The preforms are subsequently thoroughly cleaned using glass cleaning solution and then pulled on a conventional fibre pulling tower. To maintain fibre shape during pulling, a much lower temperature than normal was used (1950°C compared to 2050°C). The pulling rate was also set to be very slow (about 3m/min) to reduce the tension on the fibre.

Gallium is pumped into the holes of the pulled fibre with a syringe and needle to form the continuous internal electrodes. A thin copper wire (15μm diameter) is then inserted into the hole filled with gallium, with the aid of a microscope and a manipulator. The other end of the thin wire is soldered onto a power supply board located adjacent to the fibre end.

4.2.4 Discussion

In practice, a suitable hole separation is found to be about 20μm and a suitable hole diameter 40μm to 50μm. Attempts to make larger holes and smaller electrode separation have not been satisfactory. The fibre cores normally went flat or, in some cases, totally disappeared. The holes also went flat and sometimes opened up. It is found that the design with two holes gave a lower maximum electrical field as it breaks down at the entrance of two holes. Field strength of 500v/μm has been applied to fibres with a flat surface design.

4.3 Solid-metal-implanted fibres

4.3.1 Background

When an electromagnetic wave propagates along a metal surface, the component with a polarisation perpendicular to

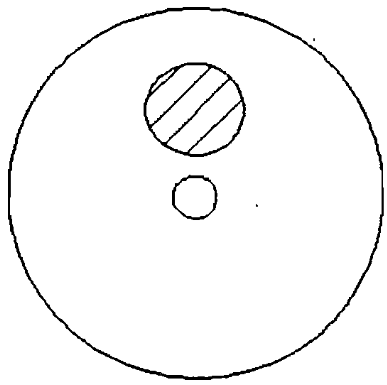

Figure 4.2 Fibre polariser design

the metal surface will penetrate into the metal surface and be attenuated, and the component with a polarisation parallel to the metal surface will penetrate much less into the metal surface and suffer a much smaller loss. This phenomenon has been known for many decades and can be used to make fibre polarisers by implanting a metal rod along one side of the fibre core. Liquid-metal polarisers have been made in the same way as electroded fibres (figure 4.2), exhibiting an extinction ratio as high as 72dB[1,2]. However, the difficult liquid-metal filling process makes it unfavourable for manufacturing in large quantities and extreme care is also needed in handling of these devices. Besides, it suffers a large loss when being fusion-spliced, due to collapse of the large liquid-metal filled holes during electric arc heating, caused by the strong surface tension of the heated glass. They are currently connected to other fibres by UV curable glue with a weak splice and a minimum loss of 1dB. To reduce the splicing loss, a smaller hole is preferred. However it makes liquid-metal filling difficult before the loss is reduced. Therefore a solid-metal implantation is considered, in which a solid metal is incorporated into the fibre preform and the preform is then pulled, enabling a smaller metal diameter and mass production.

4.3.2 Design

The main considerations for the metal in a fibre polariser are its optical characteristics, chemical stability and thermal compatibility with silica fibre. The optical properties of metals are considered in section 6.3 in chapter six. In this section we discuss the design considerations which are relevant to fibre fabrication. Chemical stability of the metal is required first to stop it degrading at room temperature and particularly at high temperature during fibre pulling. Amongst the easily available metals, gold is the best candidate in terms of chemical stability both at room temperature and fibre pulling temperature. It has a high melting temperature (1063°C) and a good malleability, and therefore is a good choice. It also has a boiling temperature of 2966°C which is essential to stop metal boiling off at the fibre pulling temperature (2050°C).

The distance between metal surface and fibre core is considered in section 6.3 in chapter six to be 2μm to achieve a high extinction ratio and low insertion loss.

4.3.3 Fabrication

An appropriate MCVD preform was made first. It had a diameter of about 12mm. A hole of 2mm diameter was then drilled parallel to the core with a distance of 0.24mm between the edges of the core and the hole. The drilling was done with an ultrasonic glass mill. The drilled preform was thoroughly cleaned by soaking in glass cleaning solution and a gold wire with a diameter slightly less than the hole diameter was inserted into the hole. To stop oxidation of gold at pulling temperature, the hole was filled with argon before fibre pulling. The preform was lowered into a furnace on a conventional fibre pulling tower and kept at above 2000°C for about 20 minutes. The preform was occasionally shaken to eliminate the air bubbles trapped in the molten gold. The air bubbles was found to be difficult to eliminate and subsequently the preform was pulled with small amount of air bubbles. The fibre has a yellowish colour caused by the implanted gold. The longest length achieved with a continuous gold implant was over 30 meters.

4.3.4 Discussion

Gold-implanted fibre has been fabricated with continuous gold length of 30 meters. This technique permits the production of fibre polarisers in large quantities and enables the fibre to be fusion spliced. Splice losses as low as 0.5dB have been demonstrated. These fibres can be handled much more easily compared with the liquid metal fibres. The optical properties of these fibres are discussed in section 6.3 in chapter six.

4.4 Cladding-pumping fibres

4.4.1 Introduction

The availability of high power diode laser arrays makes compact high power fibre lasers possible. These diode arrays are capable of providing a few watts of pumping power; however, the output beam has a rectangular shape with different beam divergencies at different directions. The dimensions of a 500mw diode array and a 3 watt diode

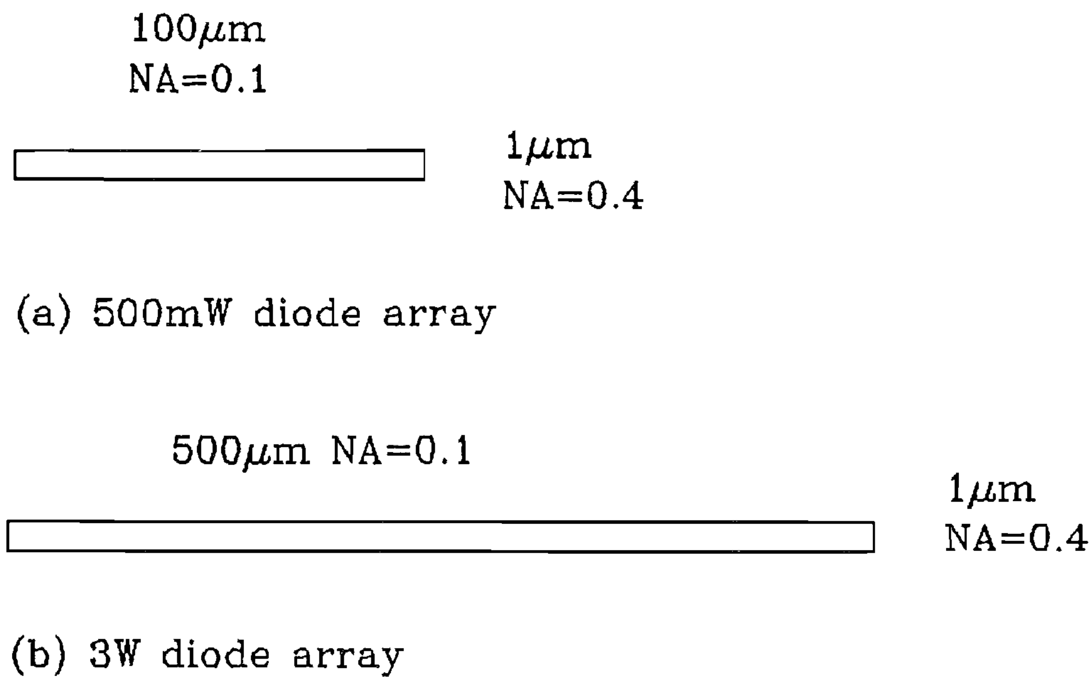

Figure 4.3 Dimensions of laser diode arrays

array are shown in figure 4.3. To ensure an efficient launch, the fibre in figure 4.4 was designed. The fibre has two waveguides. The outer one has a shape which is similar to the diode array and has a NA of 0.4. The inner guide is doped with lasing ions and forms the laser cavity with NA of 0.15. It is possible to launch into the outer guide with a high efficiency and the dopants in the inner core are then excited through the overlap of the two waveguides. The absorption coefficient will be reduced by a factor which is equal to the ratio of the two waveguide areas. However, if low loss fibre is possible, long fibre lengths can be used to compensate the reduction in pump absorption.

4.4.2 Fabrication

A Nd^{3+}-doped MCVD preform with 300ppm Nd^{3+} and NA of 0.15 was

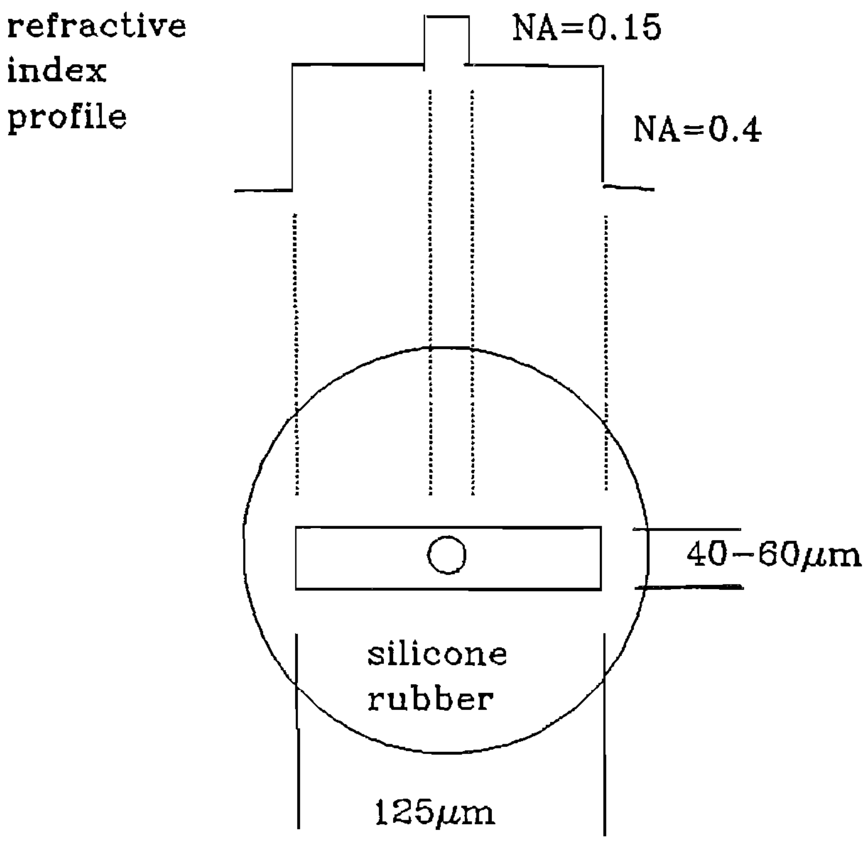

Figure 4.4 Fibre design for cladding pumping fibre laser

fabricated first. It was then milled into a rectangular shape of 11.5mm×3.7mm with the core in the centre. The preform was then pulled and coated with silicone rubber to give the outer waveguide a NA of 0.4. The coating was made by mixing silicone rubber with 10% curing agent and was contained in a steel cup. The fibre was passed through the cup and then went through a circular electrical heater to solidify the coating. A very low pulling temperature (1840°C) was used to maintain the fibre shape. Slow pulling rates (few metre per minutes) were also essential to preserve the fibre shape and ensure a good coating on the fibre. The final fibre has a outer waveguide dimension of 80μm×30μm with core slightly offset (figure 4.5)

4.4.3 Discussion

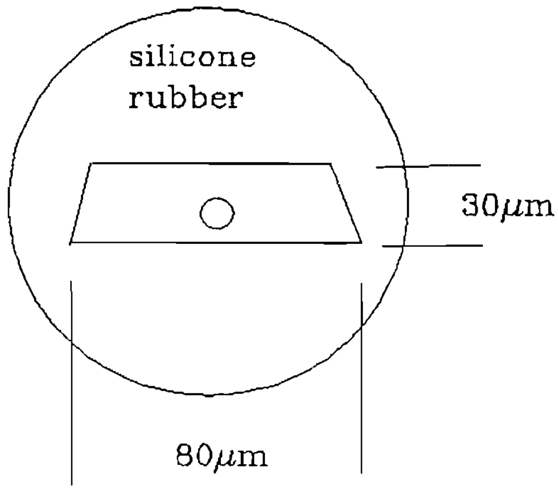

Figure 4.5 Fibre fabricated for a cladding pumping fibre laser

A thin slab fibre coated with silicone rubber has been produced. In an optimum design, the physical dimension of the outer waveguide is necessary to resemble that of the diode array. This is, however, very difficult to achieve. Extremely thin slab is very difficult to maintain its shape during pulling. Nevertheless, an improved fibre for diode array launching was fabricated. This technique of pulling fibre with special shape can also be used in making other fibre devices, such as D-shape fibres and rectangular fibres. These fibres can be used to make fibre couplers, devices requiring access to evanescent field of fibre cores, and devices requiring connection to planar waveguides.

4.5 Summary

In this chapter, we discussed the fabrication of liquid-metal-doped fibres, solid-metal-doped fibres and fibres with special shapes. These fibres have found their applications in polarisers, modulators, second harmonic generations, high power fibre lasers and couplers. The techniques used to fabricate these fibres is versatile and can be used to fabricate many other novel fibres for different applications.

References

1 L. Li, G. Wylangowski, D.N. Payne and R.D. Birch: "Low cost metal/glass fibre polarisers produced in continuous length" 4th International Conference on OFS, Tokyo, Japan, October, 1986.

2 L. Li, R.D. Birch and D.N. Payne: "High performance composite metal/glass fibre polarisers" 12th ECOC, Barcelona, Spain, September, 1986.

3 M.E. Fermann, L. Li, L.J. Poyntz-Wright and L. Dong: "Dynamics of CW-excitation poling for second-harmonic generation in germanosilicate optical fibres", Optics Letters, **14**, 1989, pp.784-750.

4 L. Li R.D. Birch and D.N. Payne: "An all fibre electro-optic Kerr modulator" IEE Colloquium on "Advanced Fibre Waveguide Devices", London, May 1986.

Chapter Five Periodically Perturbed Twin-core Fibres

5.1 Introduction

As we have described in chapter two, non-identical twin-core (TC) fibres have two fundamental modes which are well approximated by the fundamental modes of the separated fibres and, therefore, are physically separated in two fibre cores. The unperturbed coupling between the two cores is determined by the F factor described in equation 2.37 in chapter two, which can be designed to be very small. If a small perturbation with a period of the fibre beat length is applied, 100% intermodal coupling can happen over a perturbed beat length, i.e. a total switch of power from one core to another. The periodical index perturbation required is only of the order of 10^{-4} to cause a total switch of power to happen over tens of centimetres as predicted in section 2.2.5 in chapter two. This magnitude of perturbation can be produced by fibre acoustic flexural wave or mechanical means in practice, thus modulators, filters, tunable WDM taps and frequency shifters can be achieved. These devices are important in the successful implementation of single-mode fibre signal processing and communication systems.

A number of intermodal coupling devices have been reported[1,2,3,4,5,6,7]. In these devices the LP_{11} and LP_{01} normal modes of a dual-mode single-core fibre or the two polarised modes of a birefringent fibre are coupled together by an acoustic, a mechanical or a photorefractive grating whose period matches the intermodal beat length; launching light into one mode results in a signal in another mode. One hundred percent or near one hundred percent modal coupling has been achieved in these devices, and carrier and sideband suppression ratios of 29 dB and 35 dB respectively were obtained in frequency shifters. In practice, however, it is difficult to excite just one mode in these devices, and the coupled mode is not appropriate for efficient pig-tailing to single-mode fibre. These problems are compounded by the fact that slight errors in the launching condition produce a mixture of both normal modes, resulting in an intrinsic wavelength-dependence through intermodal interference. TC fibres avoid these problems by permitting low-loss fusion splicing of a single-mode fibre to either core (0.1dB demonstrated) and having negligible intrinsic coupling by designing the dual-core fibre to be phase-velocity mismatched to such a degree that the normal modes of the TC are almost identical to the modes of each core in isolation.

In this chapter, we first describe the fibre design and fabrication. The mechanical grating induced intermodal coupling in TC fibres is then discussed and, at the end of the chapter, the acoustic flexural wave case.

5.2 Fibre design and fabrication

TC fibres are designed to have two nonidentical cores and therefore negligible intrinsic coupling between the two cores. In this case, the two modes of the fibre are approximated by the fundamental modes of the two cores in the limit of infinite core separation. This is described by the theory discussed in chapter two. The modes of such a fibre are graphically represented in figure 5.1a. When light is launched into one core, by means of splicing with another single-core fibre, one mode of the fibre is mainly excited. A small proportion of the other mode is also

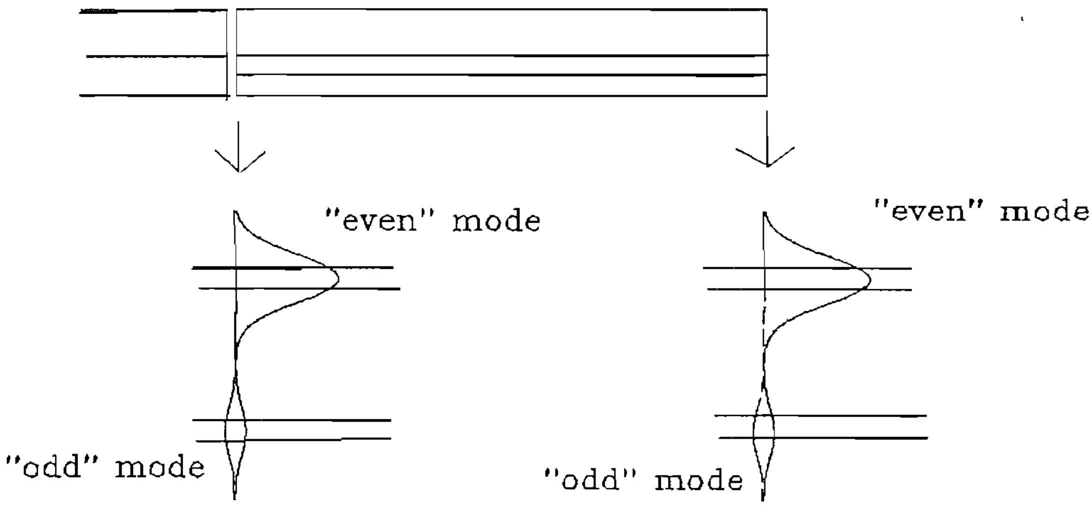

(a) Normal modes in a non-identical TC fibre
when light is launched into central core

excited to cancel out the light power in the non-launching core at beginning of the fibre. A small intensity ripple forms in the two cores as a result of two mode interference, the light remaining mainly in the launching core as depicted in figure 5.1a. The unperturbed coupling of the fibre is described by a factor, F, as defined in chapter two.

$$F = \frac{1}{\sqrt{1+\frac{(\beta_e-\beta_o)^2}{4\kappa_a^2}}} \tag{1}$$

where $\beta_{o,e}$ are the propagation constants of the two modes (even and odd) in the TC fibre and κ_a is the coupling constant of the fibre. When a periodic perturbation with the pitch of the TC fibre beat length, z_b, is applied, intermodal coupling happens and light is coupled to the other core over a length determined by the fibre parameters

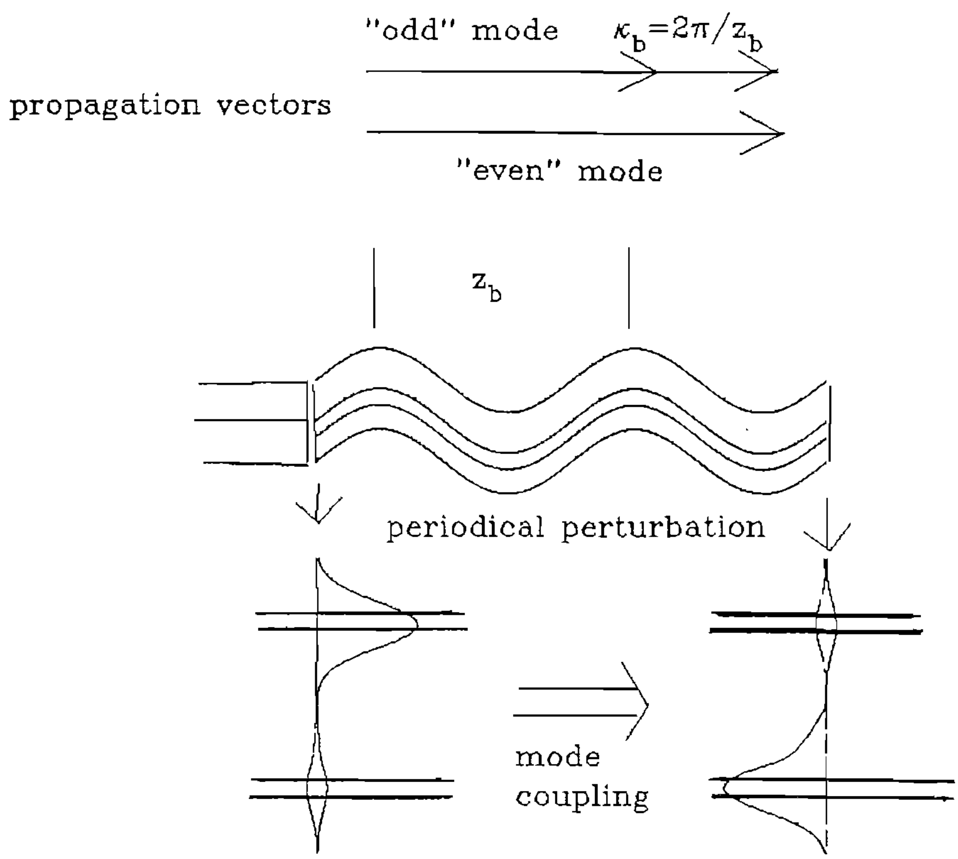

(b) Mode coupling in a non-identical TC fibre when light is launched into central core

Figure 5.1 Principle of mode coupling in a non-identical TC fibre

and perturbation strength (figure 5.1b).

$$z_b = \frac{\pi}{\beta_e-\beta_o} \approx \frac{\pi}{|\beta_1-\beta_2|} \qquad (2)$$

A negligible intrinsic coupling is desired in TC modal couplers and this involves design of fibres with very dissimilar core and large core separation. We already know, from chapter two, that this will also require a larger perturbation strength to keep the perturbed coupling length unchanged. A compromise is thus needed in the design of the fibres. It is also necessary to apply the perturbation in the plane of the two cores to produce a perturbation with opposite signs in two cores and thus to maximise the cross coupling coefficient (see section 2.2.5). Anti-symmetry is essential, since the perturbed coupling constant is proportional to the integral over the fibre cross-section of the transverse perturbation profile multiplied by the product of the two optical normal mode amplitude profiles (equations 2.55 and 2.57 in chapter two). If the perturbation is constant (as in the case of an axial perturbation), the coupling constant would be zero due to normal mode orthogonality.

To achieve controllable fibre fabrication, the TC fibres are designed to have the same core and cladding refractive index but different core radii. The two cores can therefore be made from a single MCVD preform which usually has a good uniformity over the middle section of the preform to guarantee the cores having the same index profile. The preform can be stretched into a smaller diameter on a MCVD glass lathe in a controllable manner to give the correct diameter ratio between the two cores. The unstretched preform and the stretched preform are then used as the two preforms in fabrication of the TC fibre using the method described in chapter two. The two pieces of preform are also taken as close as possible from the original preform to eliminate non-uniformity, which can give rise to very large errors in fibre coupling. The larger core is also designed to be at centre of the fibre to ease splicing with normal single-core fibres. The two fibres made have the parameters listed in table 5.1.

Table 5.1 TC fibre parameters

Fibre Name	Δ	ρ_1 (μm)	ρ_2 (μm)	d (μm)	O.D. (μm)
TC8	0.0144	1.1	0.91	5.5	110
TC9	0.00521	1.93	1.66	6.1	90

5.3 Mechanical TC modal coupler

5.3.1 Background

Modal coupling in two-moded fibres by periodic mechanical bending has been investigated by various authors[1,2,3]. Polarisation-mode coupling in a birefringent fibre was reported by Youngquist et al[1] and intermodal coupling in two-moded fibres was also studied by Youngquist et al[2] and Blake et al[3].

In this section we describe the first demonstration of mode coupling in a TC fibre caused by bending the fibre periodically by a mechanical grating. One hundred percent intermodal coupling has been obtained in a fibre with few percent intrinsic coupling. The perturbation was applied by squeezing the fibre between two V-grooved aluminium blocks. The effect of perturbation strength was also investigated.

5.3.2 Experiment

Fibre TC9 was used in the experiment. To characterise the device, intrinsic coupling of the TC fibre was measured first. A combination of a white light source and a scanning monochromator was used as the tunable light source. A single-core fibre with a matched modal spot-size was spliced onto the central core of TC9, so light could be easily launched into the central core by launching into the single-core fibre. At the detection end, one of the TC fibre cores was butted with another spot-size matched single-core fibre. The length of the TC fibre was one meter. With this arrangement, light from the two cores was

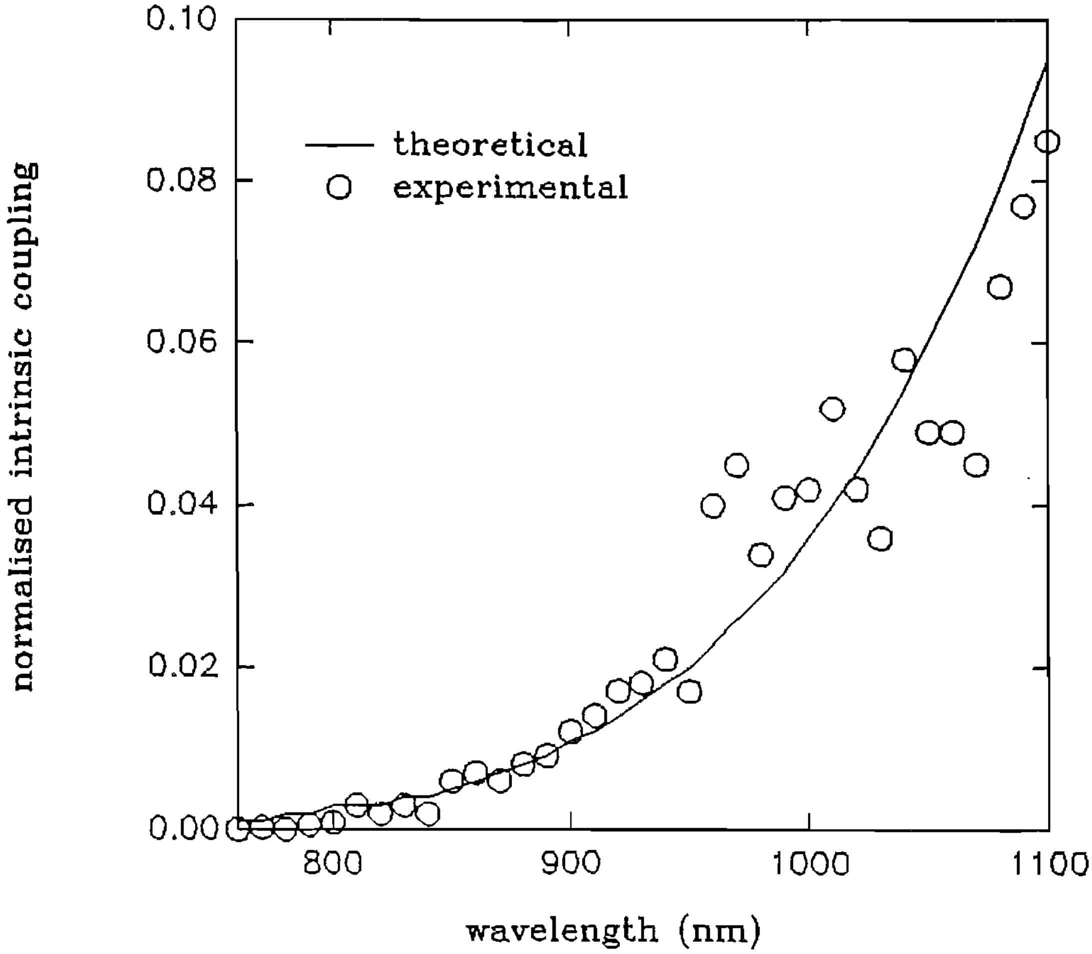

Figure 5.2 Intrinsic coupling of TC9

measured separately and intrinsic coupling was calculated. The result is shown in figure 5.2. The experimental data fits reasonably well with a theoretical curve obtained from equation 5.1.

The experimental set-up for measuring modal coupling is shown in figure 5.3. The grating was made on two aluminium blocks. There were 250 V-grooves with a depth of 0.3mm and a pitch of 1mm. Four dowel pins were used to guide the top block to be positioned to fit into the bottom block. Four nuts with springs were fitted to fix the two blocks and to adjust the perturbation strength on the fibre. The fibre was laid at a certain angle with the groove to give a required pitch. The two cores of the TC fibre were laid in

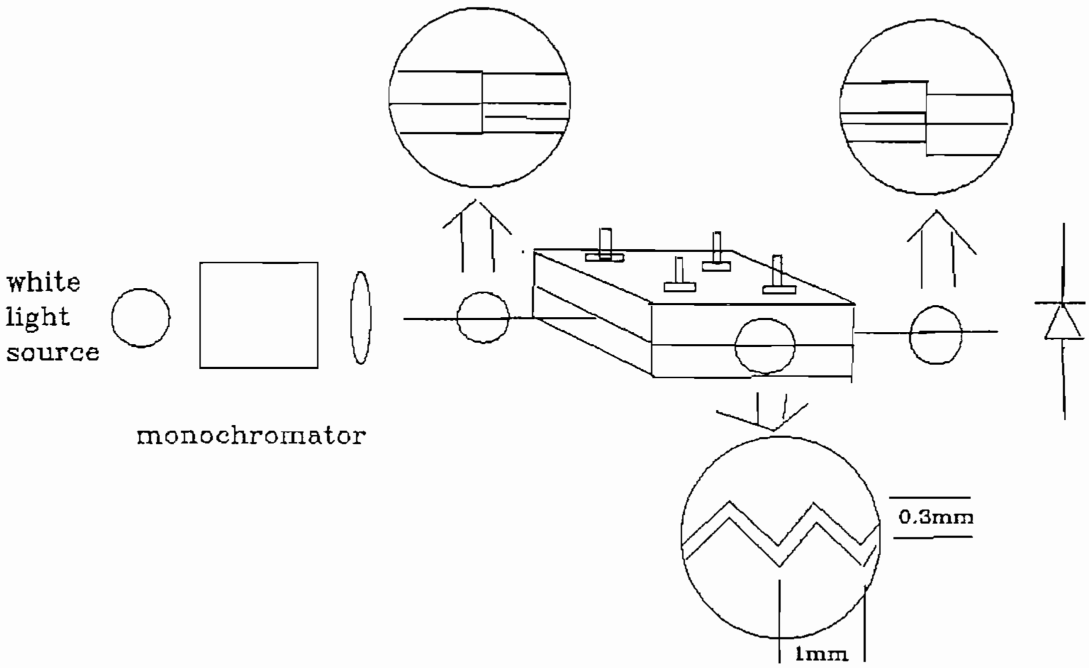

Figure 5.3 Experimental set-up for intermodal coupling in a TC fibre with mechanical grating

the plane perpendicular to the block surface. This was done by marking the orientation of the two cores while observing the fibre end under a microscope. When the angle between the fibre and the grating was 90°, the grating gave a pitch of 0.5mm. The central core of the TC fibre was spliced to a spot-size matched single-core fibre for launching into the central core. At the detection end, the TC fibre was butted with another spot-size matched single-core fibre for detection of light from one of the TC fibre cores. The power was normalised against the transmission of the system without the mechanical grating. The results for the two cores are given in figure 5.4. A grating pitch of 1.01μm and interaction length of 252.5mm

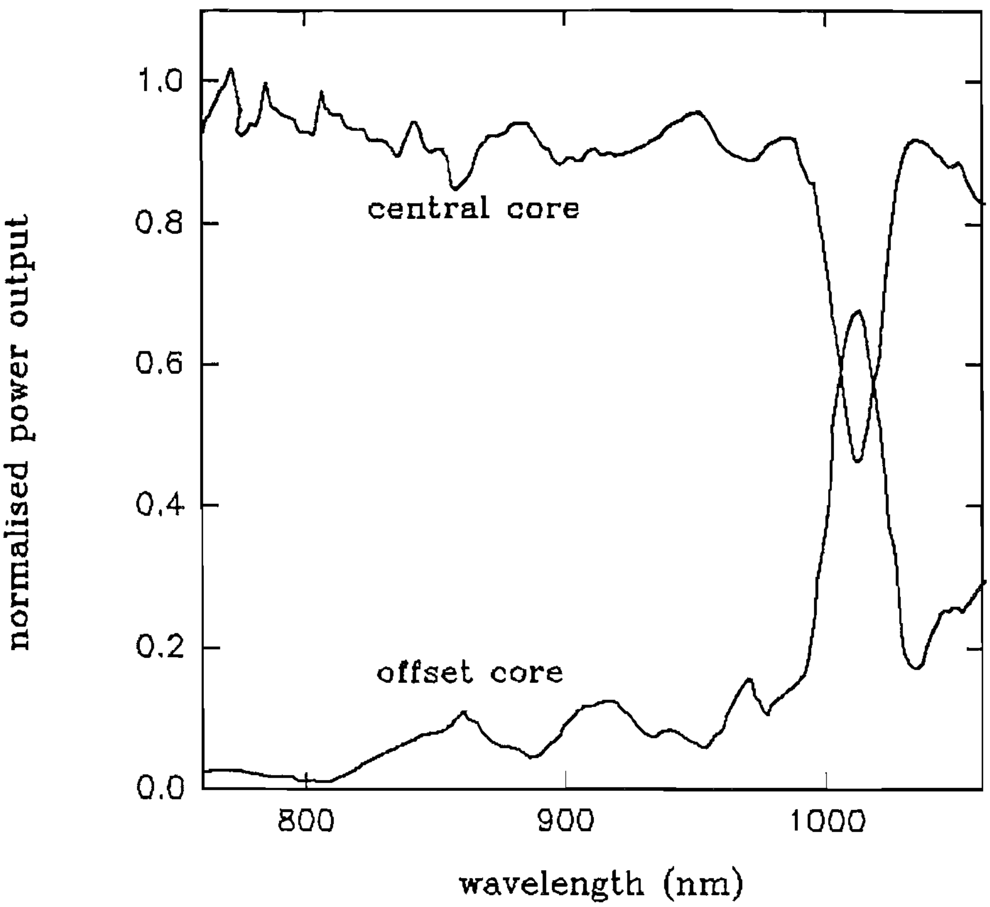

Figure 5.4 Intermodal coupling in TC9 by mechanical grating

were applied. The coupling is about 74% at 1.013μm and the coupling width is about 25nm. There are also three side bands visible in the graph, and they are at 860nm, 910nm, and 970nm. The outputs from the two cores are exactly complementary, as expected. 100% coupling was also obtained with a stronger perturbation, but the side bands have grown to a very large size. The device was tuned by varying the angle between the fibre and the V-grooves. The tuning was limited by the size of the aluminium blocks. The tuning curve is shown in figure 5.5.

5.3.3 Discussion

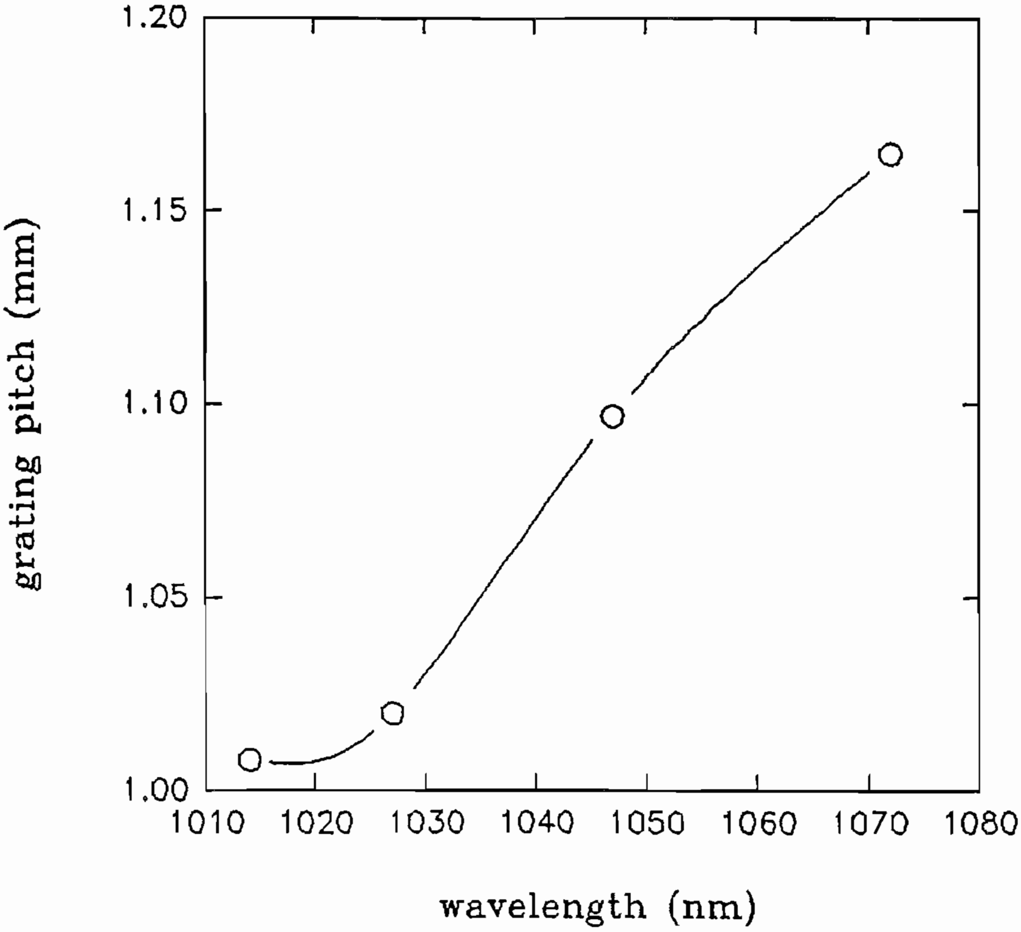

Figure 5.5 Tuning curve for intermodal coupling in TC9 by mechanical grating

From equations 2.44, the coupled power p_c is given by

$$p_c(\lambda) = F^2 \sin^2(\frac{\kappa_a L}{F}) \tag{3}$$

Combined with equations 2.36 and 2.37 in chapter two it becomes

$$p_c(\lambda) = (\kappa_a L sinc(L\sqrt{\kappa_a^2 + (\frac{\upsilon(\lambda)}{2})^2})^2 \tag{4}$$

where

$$\upsilon(\lambda) = \frac{2\pi}{z_b}(1 - \frac{\lambda_0}{\lambda}) \tag{5}$$

From equation 5.4, with L=252.5mm and I_c=74%, thus $\kappa_a = 3.4m^{-1}$.

The FWHM calculated from the theory is 2.8nm, which is much narrower than the measured value. The discrepancy is thought to be caused by the nonuniform grating pitch which arises from the uneven pressure over the fibre to stretch it differently. This can be improved by designing a grating having even pressure over the whole length of the fibre.

5.4 Acoustic TC modal coupler

5.4.1 Background

Intermodal coupling can also be induced by acoustic means. Kim et al have demonstrated the coupling between LP_{01} and LP_{11} modes by a travelling acoustic flexural wave guided along an optical fibre[5]. Total modal conversion has been achieved at 8MHz frequency shift with about 0.25W of electrical power. Carrier and side band suppression of 15dB and 35dB, respectively, were obtained. Greenhalgh et al also acquired 4.5% polarised mode conversion with electrical drive of 2W in a birefringent fibre with a surface acoustic wave device[6]. In this section, we describe the demonstration of intermodal coupling in non-identical TC fibres (TC8 and TC9) with acoustic flexural waves guided along the fibres.

5.4.2 Acoustic design

The acoustic modulator is designed as in figure 5.6. A PZT4 pad of half wave thickness is bonded to an aluminium pad of equal thickness with electrical conducting glue. This maximises the acoustic excitation by efficiently

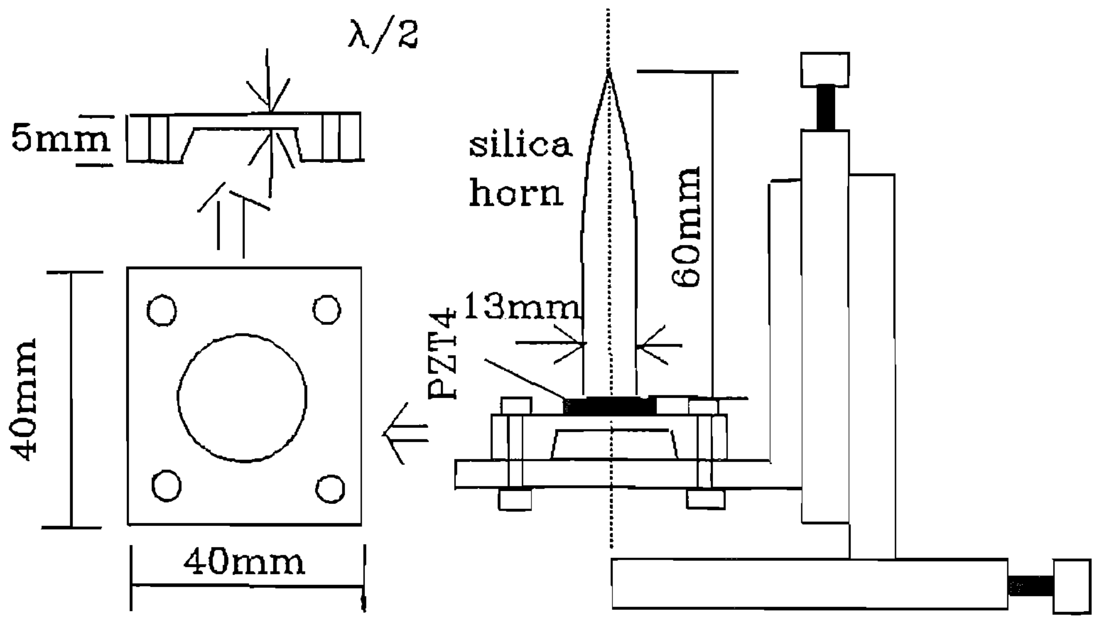

Figure 5.6 Acoustic modulator design
(left part is the aluminium
pad supporting PZT4 disc)

utilising the reflected acoustic power at the interfaces. Aluminium has also a similar acoustic impedance to PZT4, reducing the reflection at the PZT4 and aluminium interface. The aluminium pad has a thicker outer ring, suspending the inner pad in the air, and is fixed on a translation stage. The acoustic horn, made from silica rod which also has a similar acoustic impedance with PZT4, is bonded to the PZT4 disc with silicon rubber. The fibre is bonded to the tip of the horn by soft glass solder. The two electrodes on the PZT4 are connected via the upper surface of PZT4 and the aluminium pad. A matching network is also required to couple electrical energy efficiently onto the piezo. The translation stage ensures precise positioning of the horn.

The TC fibre is held with two silica capillaries, which are fixed in tension stands. The fibre is bonded with silicone rubber to the silica capillaries, for damping acoustic energy, and the stand has two steel sheet supports, ensuring the fibre under tension.

5.4.3 Experiment

5.4.3.1 Characterisation of acoustic excitation

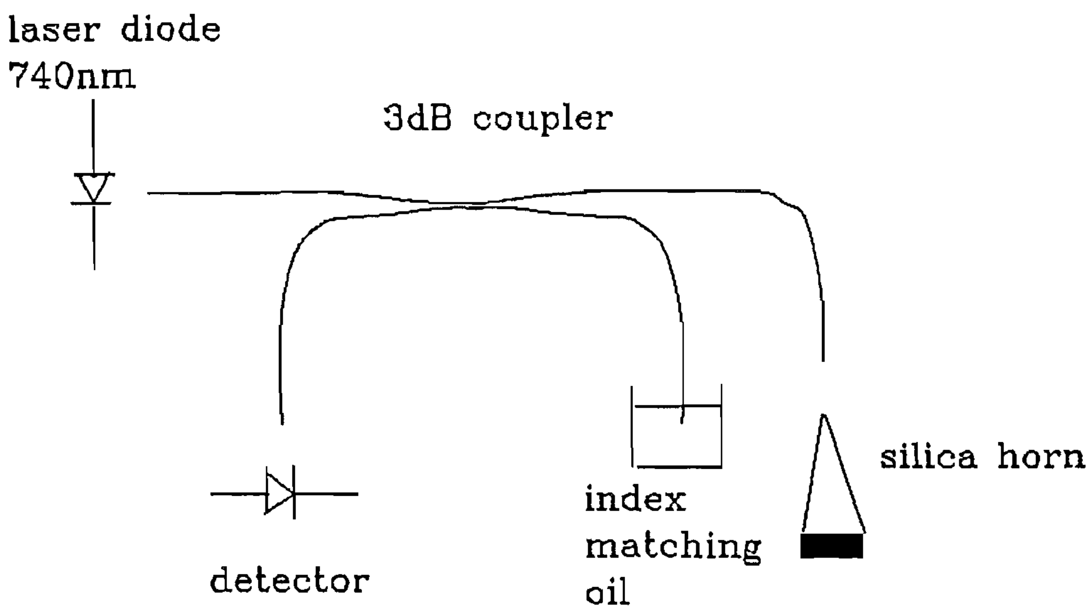

Figure 5.7 Set-up for characterisation of silica horn

The acoustic transmission of the horn was characterised with the set-up in figure 5.7. An interferometer arrangement at 780nm was used to measure the movement of the tip of the horn. The light from a Hitachi 7801E laser was launched into one input arm of a 3dB coupler. One output arm of the coupler was immersed in index matching oil to eliminate the reflection from that arm. The other output arm was cleaved and placed very close to the cleaved tip of the horn. The reflected light from the cleaved fibre end and the tip of the horn was collected with a silicon detector (40k termination, 0.5MHz) from the other input arm of the coupler.

The amplification of the horn is found to be approximately an order of magnitude and the spectral response of the horn is found to be fairly flat with only few nodes.

5.4.3.2 Acoustic wavelength measurement

A TC fibre was glued into the fibre holder with silicon rubber and bonded onto the tip of the horn with soft glass solder. The acoustic wavelength on the fibre was measured with the same fibre interferometer as the one measuring the horn transmission. The cleaved end of the fibre was mounted on a translation stage and could be moved along the fibre. The acoustic wavelengths at various frequencies were measured. The result of averaging over 10 or 20 acoustic periods of flexural waves is shown in figure 5.8. The solid curve is a theoretical predication at low frequencies given by Thurston[8], which is

$$\frac{c_f}{c_{ext}} \approx \sqrt{\frac{\pi f_a D}{2c_{ext}}} = \sqrt{Q} \tag{6}$$

where c_f is acoustic wave velocity, c_{ext} longitudinal wave velocity (5760ms^{-1} for silica), and D fibre diameter (100μm).

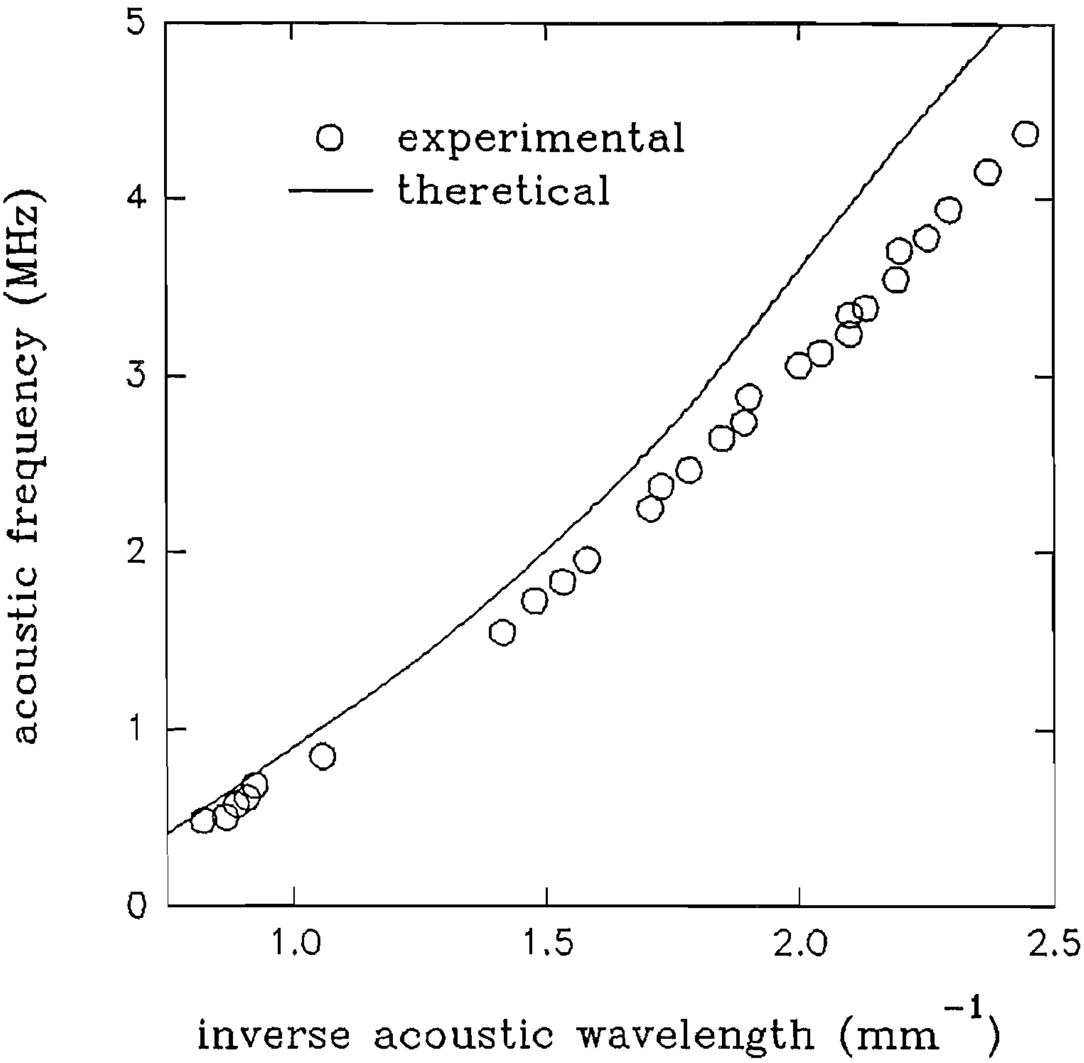

Figure 5.8 Acoustic dispersion relation

This approximation over-estimates c_f/c_{ext} by less than 5% for q<0.1. At high frequencies c_f approaches the surface wave velocity. In our experiments, q ranges from 0.12 to 0.37 (500kHz<f_a<5MHz). The expected deviation with the measured data at higher frequency is apparent. The acoustic amplitude is also measured over the 30cm lengths used; no acoustic damping could be measured.

5.4.3.3 Intermodal coupling

The set-up in figure 5.9 is used to measure the intermodal

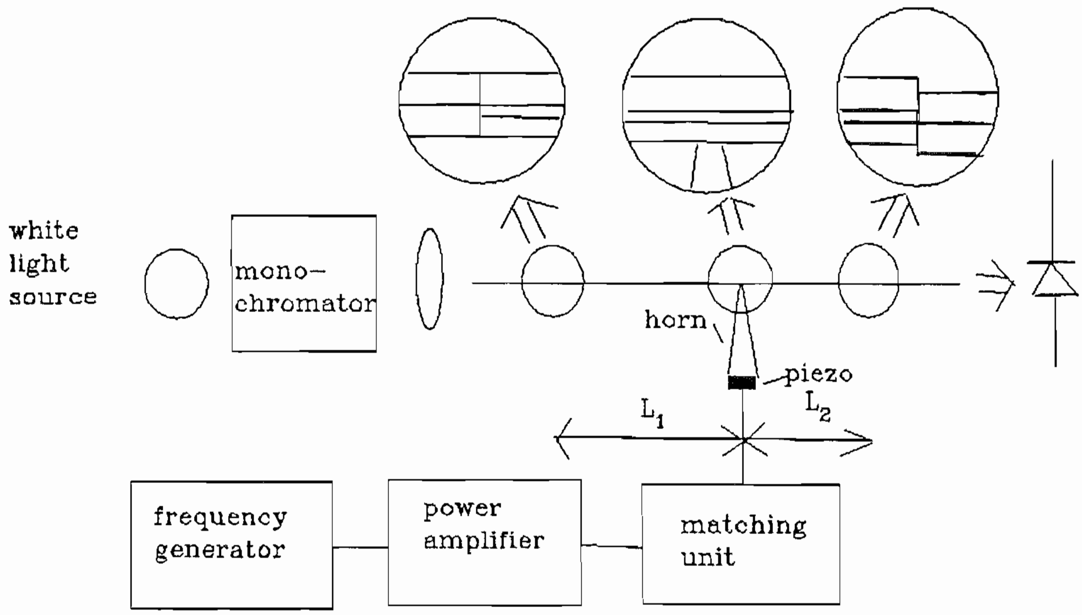

Figure 5.9 Experimental set-up for intermodal coupling in a TC fibre with acoustic fibre flexural wave

coupling in the TC fibres. A tungsten lamp and monochromator combination was used to deliver tunable narrow band (1-2nm) light to a single-core fibre spliced to the centre core of the TC fibre. The offset core was butted with another single-core fibre at the detection end of the TC fibre. An acoustic frequency was selected, and the optical wavelength scanned until coupling was obtained. The acoustic driving signal was amplitude-modulated to permit easy detection of coupling to the offset core. Once coupling had been achieved, the interferometer was used to measure the beat length; this enabled the beat length to be plotted as a function of wavelength for the fibres measured. The results are plotted in figure 5.10. The

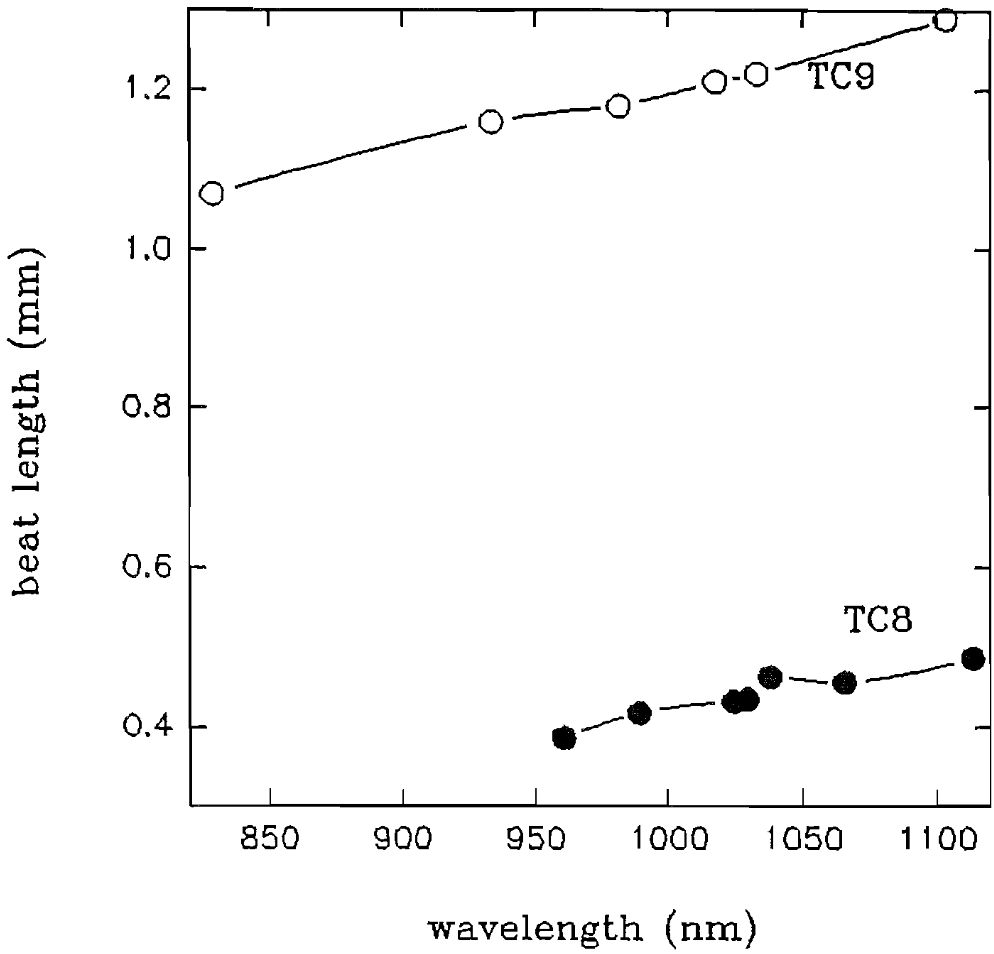

Figure 5.10 Tuning curves for intermodal couplinge by acoustic flexural wave

beat length is a fairly linear function of wavelength in both cases, indicating negligible dispersion in the measured wavelength range. The tuning curve for TC9 also shows that a longer perturbation period than that in the mechanical grating case is necessary. This is expected due to the fact that the fibre was stretched in the mechanical grating case.

Different phenomena contribute to the acousto-optical coupling constant; the first is micro-bending and the second strain-optical effects. It is therefore interesting to know how the coupling strength varies with flexural wave amplitude. Using the set-up in figure 5.9, this is measured directly, providing data that may be related to theory, in order to clarify the relative importance of micro-bending and strain-optical effects. The horn is bonded to a length of fibre TC9 at a point L_1=91mm from one end and L_2=290mm from the other. It is straight forward to show that the conversion efficiency to the second core (measured at a square-law detector) obeys the relationship

$$\eta_c = \sin^2\kappa_a L_1 + \sin^2\kappa_a L_2 - 2\sin^2\kappa_a L_1 \sin^2\kappa_a L_2 \qquad (7)$$

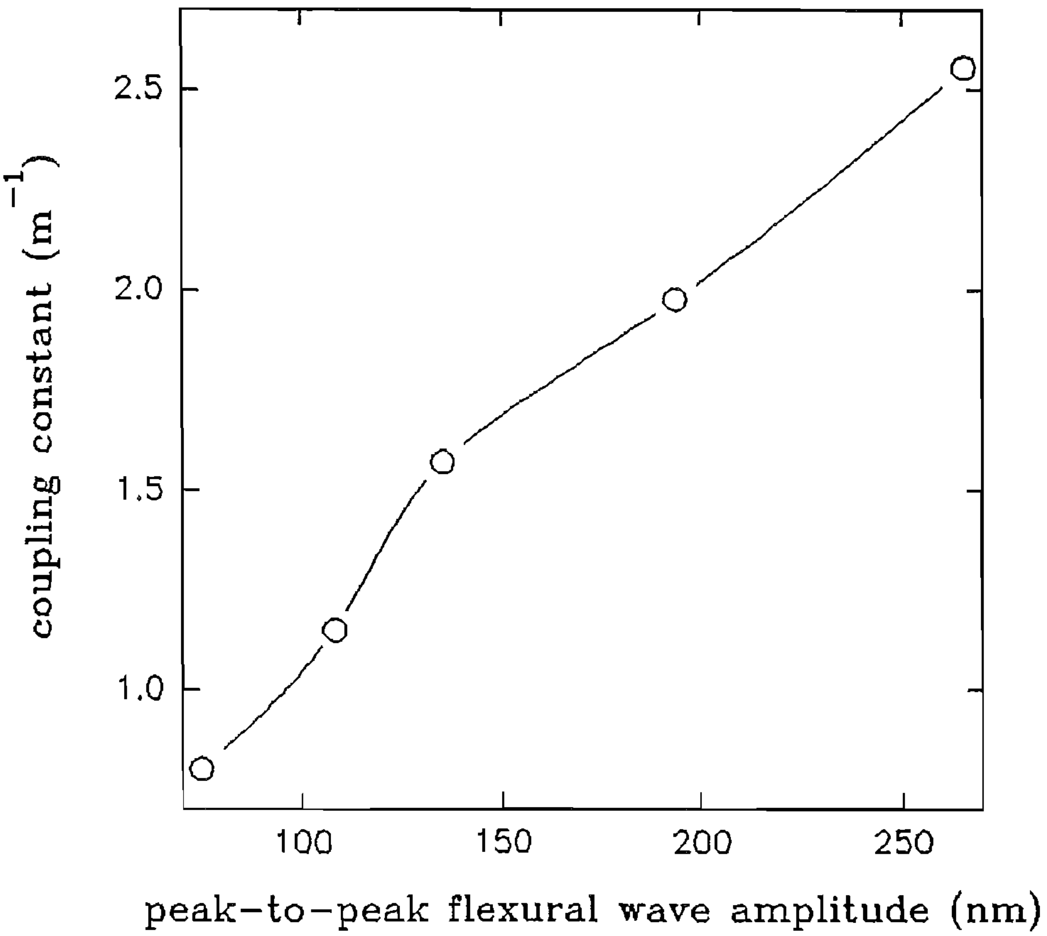

Figure 5.11 Relation between coupling constant and peak-to-peak flexural wave amplitude

A plot of κ as a function of flexural wave amplitude, obtained by solving this equation for κ using experimentally determined values for η_c at different acoustic power levels, is given in figure 5.11. The intrinsic coupling in TC8 was too small to measure, and 8.5% acousto-optical coupling was obtained at 4.6MHz and 962.5nm. TC9's intrinsic coupling is about 3%, and 100% (and beyond) acousto-optical coupling was achieved at

560kHz and 1.064μm. The electrical drive power at 100% coupling was around 200mW. For L=240mm, TC8 yields 8.5% efficiency at f_a=4.634MHz and λ_0=962.5nm, corresponding to a beat length of 0.407mm and coupling constant κ=1.2m^{-1}. The measured conversion-efficiency with wavelength has a FWHM of about 1.5±0.5nm (resolution limited by the monochromator); this agrees well with the theoretical prediction (calculated from equation 5.4) of 1.3nm. This excellent agreement confirms that the beat length was uniform over a fibre length of 290mm. In the case of TC9, for 25% efficiency over a fibre length of 290mm at z_b=1.21mm, f_a=589kHz and λ_0=1.02μm, the theoretical FWHM is 4nm.

5.4.3.4 Frequency shifting measurement

The heterodyne set-up for measuring frequency shift in TC9 is given in figure 5.12. A 40MHz Bragg Cell was used. The light from a YAG laser (1.064μm) was split into two fibres by a 3dB coupler. After going through the Bragg Cell and the TC frequency shifter, the light was combined in the second 3dB coupler. The result are shown in figure 5.13. Carrier and side-band suppression ratios were measured to be 11dB and 4.5dB respectively. The bad side-band suppression is due to the 91mm of fibre on the opposite side of the horn.

5.4.4 Discussion

Total intermodal coupling in TC fibre by acoustic flexural wave has been demonstrated for the first time. The device can be used as modulators, filters, frequency shifter and tunable WDM taps. These are vital components in fibre

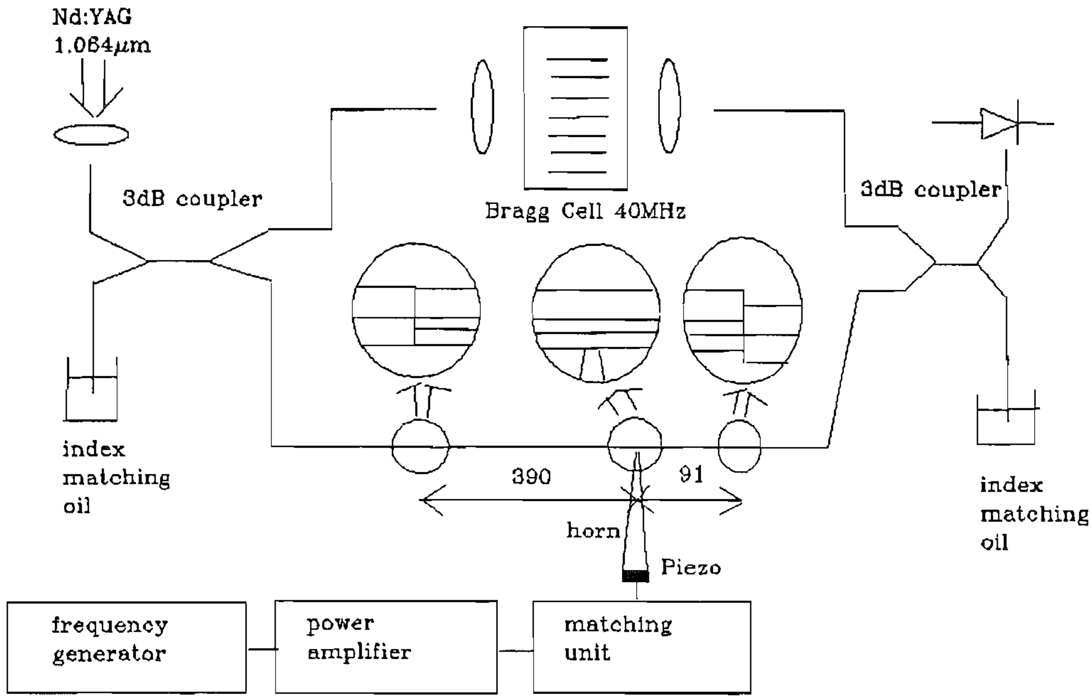

Figure 5.12 Experimental set-up for frequency shift measurement

sensors, interferometers, gyroscopes and tele-communications. The TC fibre device also possesses the unique advantage of being able to be spliced onto an ordinary single core fibre system with very low loss (0.1dB demonstrated). With additional development the device has considerable potential in practical applications.

5.5 Summary

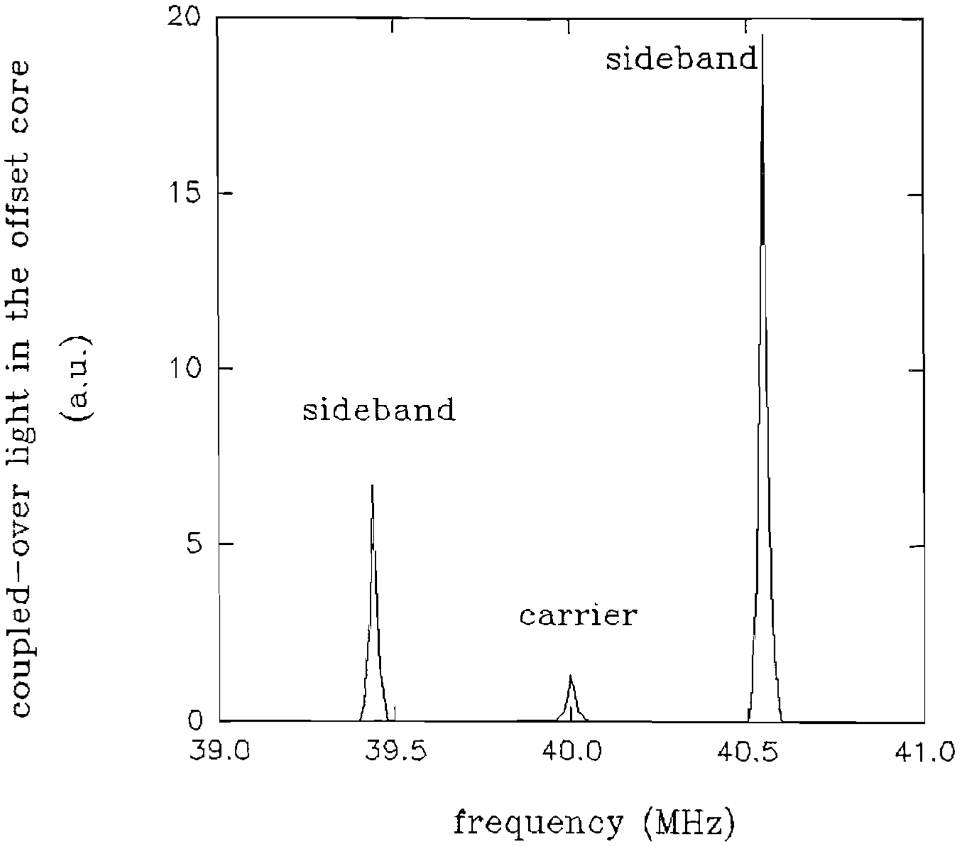

Figure 5.13 Frequency shift in TC9 by acoustic flexural wave

In this chapter, we have described periodically perturbed TC fibre devices. 100% intermodal coupling has been observed for the first time with mechanical grating and acoustic flexural wave. The coupling bandwidth in the mechanical grating case is much larger than that predicated by theory, indicating non-uniformity in perturbation pitch along the fibre. Nevertheless, efficient coupling is observed with a small perturbation. The tunability of the devices is also demonstrated. An improved version with better perturbation pitch uniformity and electronically controlled perturbation strength would make it practical for applications such as fibre modulators, switches and filters. The acoustic flexural wave device has a worse carrier suppression than its counterparts; this is mainly due to the large intrinsic coupling (of a few percent) in the TC fibre. This can also be improved by having more mismatched cores or controlling temperature of the fibre to give zero carrier in the second core, however, larger electrical drive power will be required. These devices, with further improvement, should find applications in interferometers, filters, switches, and wavelength-multiplexing systems.

References

1 R.C. Youngquist, J.L. Brooks, and H.J. Shaw: "Birefringent-fibre polarization coupler", Optics Letters, **8**, 1983, pp.656-658.

2 R.C. Youngquist, J.L. Brooks, and H.J. Shaw: "Two-mode fibre modal coupler", Optics Letters, **9**, 1984, pp.177-179.

3 J.N. Blake, B.Y. Kim, and H.J. Shaw: "Fibre-optic modal coupler using periodic microbending", Optics Letters, **11**, 1986, pp.177-179.

4 H.G. Park and B.Y. Kim: "Intermodal coupler using permanently photo-induced grating in two-mode optical fibre", Electronic Letters, **25**, 1989, pp.797-799.

5 B.Y. Kim, J.N. Blake, H.E. Engan and H.J. Shaw: "All-fibre acoustic-optic frequency shifter", Optics Letters, **11**, 1986, pp.389-391.

6 P.A. Davies: "All-fibre frequency shifter using piezoceramic saw devices" Electronic Letters, **25**, 1989, pp.1206-1207.

7 G.J. Cannel, R.E. Epworth, N.E. Jolley, C.M. Legget and

A. Robinson: "Wavelength selection cross-coupling for distributed fibre sensors", EFOC/LAN 88.

8 R.N. Thurston: "Elastic waves in rods and clad rods", Journal of the Acoustic Society of American, **64(1)**, 1978, pp.1-37.

Chapter Six Miscellaneous Fibre Devices and Effects

6.1 Introduction

In this chapter, we discuss some other novel optical fibre devices and effects, e.g. cascaded TC fibre filters, gold-implanted polarisers, excitation poling in second harmonic generation (SHG) and spatial mode converters. These fibre devices and effects have been investigated for various applications in optical fibre systems. The work on the cascaded TC fibre filter reveals the limits of the technique. The gold-implanted fibre polariser has many advantages over its liquid-metal counterpart. The excitation poling with a strong electric field shows the potential of a much improved efficiency of SHG. The spatial modal converter deals successfully with the problem of conversion of a circular fibre mode to a triangular planar waveguide mode. These devices provide both passive elements and optical sources for optical fibre systems and are vital components in future optical fibre systems.

6.2 Cascaded-TC-fibre filter

6.2.1 Background

The dispersive nature of the coupling constant in an identical-core TC fibre makes it very attractive for fibre filter applications. A filter made by cascading four TC fibres with a beat length of 4.8cm at 1.55μm has been demonstrated to give a FWHM of 17nm with an insertion loss of 1.9dB by Okamoto et al[1]. A narrower bandwidth filter has many applications in fibre telecommunications and sensors. It can be used to filter out a narrow band signal in a wavelength multiplexing system and to separate signal from noise in a fibre amplifier system. In these cases, a fibre filter is also preferred to its bulk counterpart for the reasons of easy connection and less insertion loss. It is compact, rigid and easy to fit into the rest of the system.

6.2.2 Theory

If we launch unit power into core 1 of an identical-core TC fibre, the power output from core 1 after a length of L is

$$P_1 = \cos^2(\kappa_a L) \tag{1}$$

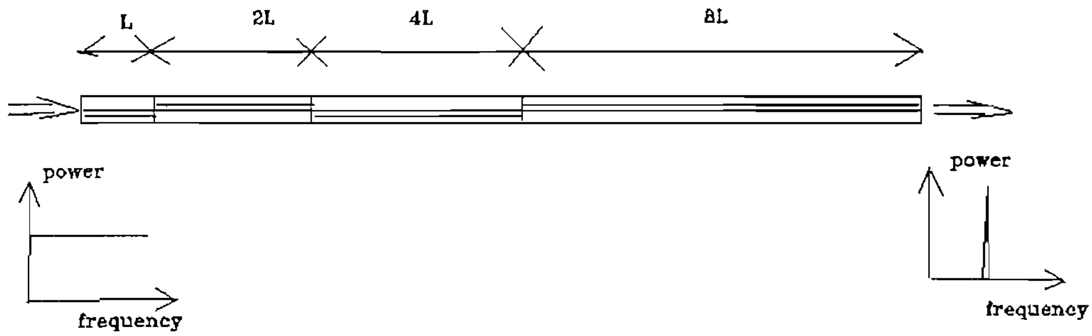

Figure 6.1 Cascaded TC fibre filter

If TC fibres of length L, 2L, 4L and 16L are cascaded together with only core 1 connected as in figure 6.1, the power in core 1 at each connection is allowed to continue its propagation and that in core 2 is lost by excitation of radiation modes in the following TC fibre. If no connection loss is considered, the power output from the last TC fibre will be

$$P_{out} = P_1(L)\,P_1(2L)\,P_1(4L)\,P_1(16L)$$
$$= \frac{1}{256}\frac{\sin^2(16\kappa_a L)}{\sin^2(\kappa_a L)} \tag{2}$$

This is the transfer function of a band-pass filter. If we have $\kappa_a(\lambda_0)L=m\pi$ (m is an integer) and assume a linear function for $\kappa_a(\lambda)$ in the vicinity of λ_0 then

$$\kappa_a(\lambda) = \kappa_a(\lambda_0) + \frac{d\kappa_a(\lambda_0)}{d\lambda}(\lambda-\lambda_0) \tag{3}$$

From equations 6.2 and 6.3, the full width of the pass-band can be obtained as

$$\Delta\lambda = \frac{m\pi}{8L}\frac{1}{\frac{d\kappa_a(\lambda_0)}{d\lambda}} \tag{4}$$

where $Ld_a\kappa(\lambda_0)/d\lambda>>1$. The free wavelength range is

$$\Delta\lambda_{free} = \frac{1}{2}|\lambda_2-\lambda_1| \tag{5}$$

where $\lambda_{1,2}$ are determined by

$$\kappa_a(\lambda_1) = (m-1)\pi \tag{6}$$

$$\kappa_a(\lambda_2) = (m+1)\pi \tag{7}$$

For a TC fibre with $\Delta=0.0017$, $\rho_1=\rho_2=\rho=2\mu m$ and $d/\rho=4$, $\Delta\lambda=3.3nm$ at $0.7\mu m$ with L=5cm and m=1.

6.2.3 Experiment

The spectral response of a TC fibre was investigated in chapter two. The sensitivity of the coupling to small perturbations was also investigated. Despite this, a cascaded TC band-stop filter was successfully realised using the fibre TC1 (see chapter two). There were three sections with lengths of 5.8cm, 7.8cm and 11.6cm respectively. The sections were fusion spliced together (yielding a total insertion loss of 1.2dB) and were kept straight to give a bandwidth of 16nm and a rejection ratio of 15dB. The filter performance deteriorated severely if one of the sections was slightly bent.

6.2.4 Discussion

A theoretical bandwidth of 13nm can be derived from equation 6.4. and the slightly worse performance of the filter is believed to be caused by the fact that the sections are not in a perfect straight state. As discussed in chapter two, filters with more sections become extremely difficult to make owing to the perturbation-sensitivity of the fibres.

6.3 Gold-implanted fibre polariser

6.3.1 Background

In many areas of optical fibre systems, polarised light is required to eliminate polarisation-dependent properties. These areas include coherent telecommunication systems, fibre gyroscopes, polarised fibre lasers and some fibre sensor systems. A fibre polariser is therefore a vital component in these systems, producing linearly polarised light without the penalty of large insertion loss. Metal-implanted polarisers employ the property that light with different polarisations propagating along a metal surface will suffer different losses due the difference in field penetration depths. Liquid-metal implanted polarisers have been demonstrated with extinction ratios as high as 72dB and insertion losses of 1dB[2,3]. However they are difficult to splice to ordinary fibres as desired in practice. Well developed fusion-splicing techniques cannot be used owing to the fact that the big hole in the polariser collapses under strong surface tension at the high fusion temperatures. UV curable glue has been used yielding a splice loss of 1dB. This method is, however, tedious and does not give a strong splice. A small hole is apparently desirable, but this makes the liquid-metal insertion very difficult if not impossible. The solid-metal implantation described in chapter four was therefore used. This method not only supplies a solid fibre but also offers a more convenient way of mass fabrication. Silver has been attempted and found to be oxidised thus degrading the polariser performance. The success of gold-implantation in chapter four revives the thought of a solid-metal-implanted polariser.

6.3.2 Theory

The performance of a polariser is assessed by means of its extinction ratio r_{ex} in dB, which is defined at the output of the polariser to be

$$\begin{aligned} r_{ex} &= \alpha_y - \alpha_x \\ &= 10 \log \frac{P_y}{P_x} \end{aligned} \tag{8}$$

where $\alpha_{x,y}=10\log P_{x,y}$. $P_{x,y}$ are the output powers from the polariser along the x and y polarisations respectively, for equal input powers along the two polarisations.

The earliest attempt to analyze a metal-implanted fibre polariser theoretically used a slab model[4]. This reduces the problem to one-dimension, simplifying it significantly. The propagation constants can be easily worked out for both TM and TE waves by deriving the eigen equations from Maxwell's equations and then solving them numerically. The TM field has a major electric field component normal to the metal surface (y direction) and suffers a large loss, α_y. The TE field only has an electric field component parallel to the metal surface (x direction) and suffers a small loss, α_x. A more rigorous analysis is later given by Vassallo with a two-dimensional model[5]. The field inside and outside the fibre core is written as a Fourier-Bessel series and near the metal surface as a plane wave. The result is a far more complicated equation for the propagation constants. The solution, however, is very similar to that of the one-dimensional model. Another attempt to solve the two-dimensional model is recently given by Tong et al[6]. This analysis is based on equivalent current theory of optical waveguide coupling and the reflected wave from the metal surface in the core area is ignored. The result is in a simple analytical form, which fits well with the previous solutions apart from when the distance between metal and core is small. Many other aspects of fibre polarisers have also been investigated by various authors[7,8,9,10,11,12,13,14,15,16].

In the slab model, the eigen value equation for a four-layer structure is given by[4]

$$\tan^{-1}\left(\frac{K_1}{jK_2}\right)-u_2t_2+\tan^{-1}\left[\frac{K_3}{jK_2}\tan\left(\tan^{-1}\left(\frac{K_4}{jK_3}-u_3t_3\right)\right)\right] = 0 \quad \textbf{(9)}$$

where $K_i = u_i/n_i^2$ for TM wave,

$K_i = u_i$ for TE wave,

$u_i = k^2 n_i^2 - \beta^2$,

$k = 2\pi/\lambda$, vacuum wave number,

β = propagation constant,

n_i refractive index of layer i (see figure 6.2),

t_i thickness of layer i.

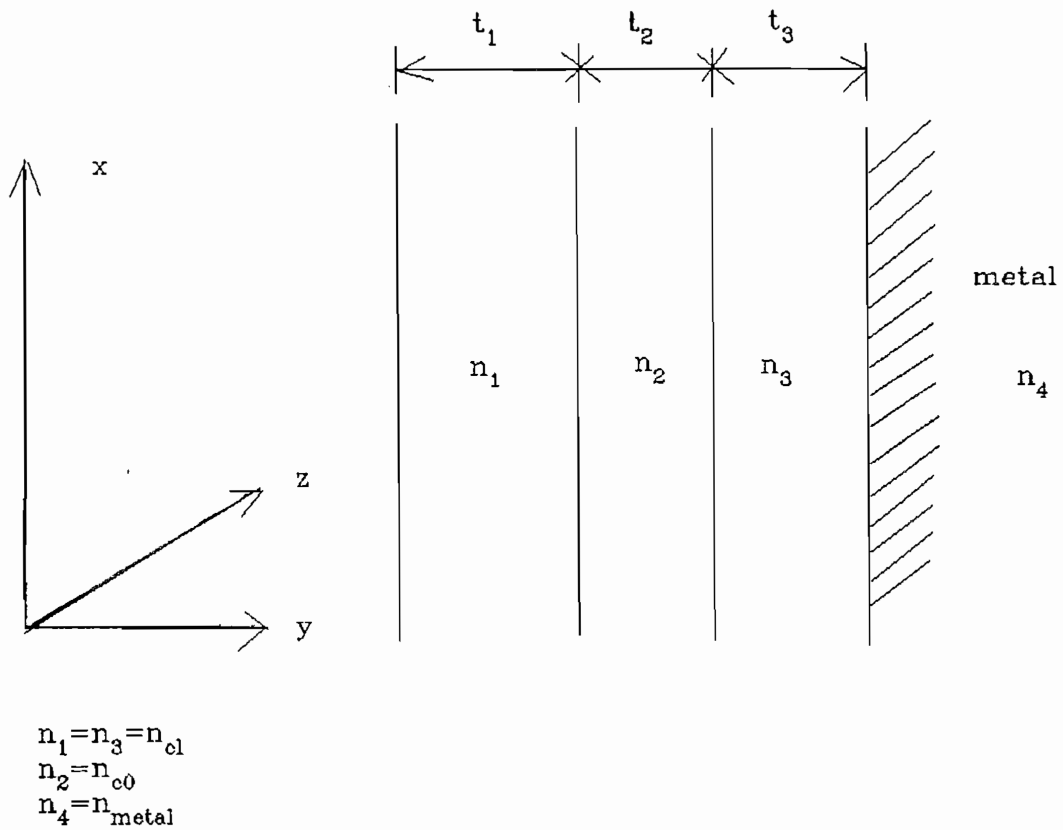

Figure 6.2 Slab model of a metal-implanted polariser

The equation given by Vassallo[5] for the three-dimensional model is

$$\left(\frac{VK_m'}{K_m}-U\frac{J_m'}{J_m}\right)B_m+\left(\frac{VI_m'}{I_m}-U\frac{J_m'}{J_m}\right)\frac{I_m}{\eta_m K_m}\sum_{n=0}^{M-1}P_{mn}B_n = 0 \qquad (10)$$

where $P_{mn} = 2\int_0^\infty R_v \cosh(mg)\cosh(ng)\,e^{-2\gamma d\cosh(g)}dg$,

$U = \alpha R$,

$V = \gamma R$,

$\alpha^2 = k^2 n_{co}^2 - \beta^2$,
$\gamma^2 = \beta^2 - k^2 n_{cl}^2$,
B_{mn} modal amplitudes in Fourier-Bessel series,
$K_m = K_m(v)$ Bessel function,
$J_m = J_m(v)$ Bessel function,
$I_m = I_m(v)$ Bessel function,
$R_v = (a_v - b_v)/(a_v + b_v)$ for TE wave,
$R_v = (a_v/n_{cl}^2 - b_v/n_{metal}^2)/(a_v/n_{cl2}^2 + b_v/n_{metal}^2)$ for TM wave,
$a_v^2 = \gamma^2 + \alpha^2$,
$b_v = a_v^2 + k^2(n_{cl}^2 - n_{metal}^2)$,
$\eta_0 = 2$,
$\eta_m = 1$ for m>0.

As a result of numerical iteration methods, the propagation constants, $\beta_{(x,y)}$, which are complex numbers, $\beta_{r(x,y)} + \beta_{i(x,y)}$, can be solved from equations 6.9 and 6.10. The extinction ratio can be calculated from $\beta_{(x,y)}$.

$$\alpha_{x,y} = 10 \log e^{-2\beta_{i(x,y)}} \tag{11}$$

For a fibre with n_{co}=1.47, n_{cl}=1.4585, n_{metal}=2.09-j5.063 and d=3.33μm, at λ=0.8μm, the solutions are shown in figure 6.3.

6.3.3 Design considerations

6.3.3.1 Metal choices

The compatibility with silica glass places a stringent restriction on the choice of metals. High melting temperatures are therefore required to match the high

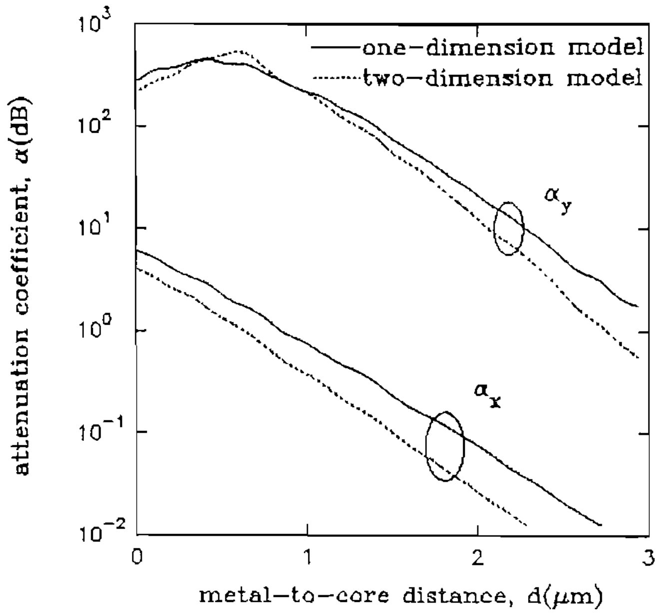

Figure 6.3 Attenuation of the x- and y- polarised modes for gallium-implanted fibre polariser as a function of metal-to-core distance

melting point of silica (about 1800°C). The melting and boiling temperature, for the commonly available candidates are listed in table 6.1.

Table 6.1 Melting and boiling temperatures of some common candidates

Metals	Melting Points	Boiling Points
Gallium	29.78°C	2403°C
Indium	156.61°C	2000°C
Aluminium	660.2°C	2467°C
Silver	960.8°C	2212°C
Gold	1063°C	2966°C

These metals all have high boiling temperatures which prevent boiling off. The High melting temperature requirement makes gold and silver better candidates. Chemical stability, especially at high temperature, is also required to prevent degradation of the metal. Gold is a better candidate in this aspect.

The optical performance in a polariser of the various candidate metals is now compared by means of the theoretical simulation. The optical constants of the metals are given in table 6.2. The permittivity, ϵ, is given by $n_m^2=(n-ik)^2$ and can be used in the simulation to investigate the extinction ratio if the metal is used.

Table 6.2 Optical constants of various metals

λ	0.6μm		1.3μm		1.5μm	
Metal	n	k	n	k	n	k
Ga	1.25	6.6	4.55	12.5	5.8	13.8
In	1.29	2.59	2.07	9.62	2.3	11.3
Al	1.1	7.5	1.92	10.9	2.02	12.5
Ag	0.06	3.75	0.38	7.8	0.45	9.0
Au	0.2	2.9	N/A	N/A	N/A	N/A

As a result of simulation, gallium gives the highest extinction ratio and is much better than the rest. The order of metals in order of better extinction ratio is gallium, aluminium, indium, silver and gold. In an optimum design with an insertion loss of 0.5dB, an extinction ratio of more than 75dB is achievable with gallium, 35dB with aluminium and only 12dB with gold. Despite the poor performance of a gold polariser, the thermal compatibility with silica still makes it the best choice and was therefore the one chosen in the experiments.

6.3.3.2 Structural considerations

A compromise between polariser insertion loss and extinction ratio can be achieved by varying the core/metal distance, modal spot-size and fibre length. A core/metal distance of about 2μm is found to give the best overall performance from the simulation. The fibre NA is chosen to be a common value of 0.12.

6.3.4 Measurements

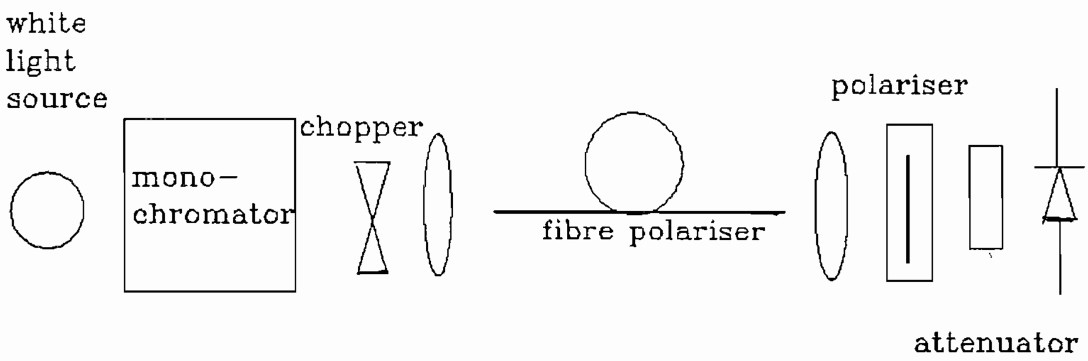

Figure 6.4 Experimental set-up for fibre polariser measurement

The polariser was fabricated in the way described in chapter four. The fibre diameter is 125μm and has a metal diameter of 20μm. The core became slightly elliptical during pulling. The distance between the edges of the metal and core is 2μm. The set-up in figure 6.4 was used to characterise the polariser. A 150W tungsten lamp was employed as a light source. Light from a monochromator was

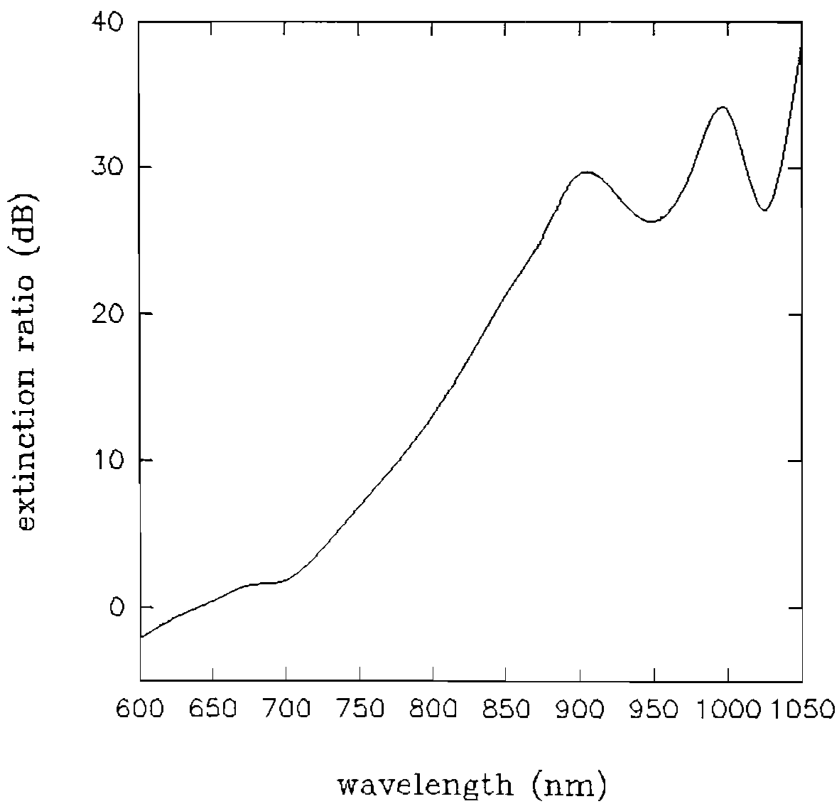

Figure 6.5 Extinction ratio of the gold-implanted fibre polariser

depolarised and a polariser was placed at the end of the fibre to discriminate light with two different polarisations. The input light was modulated by a mechanical chopper and the in-phase signal was detected by a lock-in amplifier. The system had a dynamic range of 40dB. The extinction ratio for one meter of fibre is shown in figure 6.5. The curve above 900nm is due to cross-coupling between the polarisations. The insertion loss from 800nm to 1100nm is a flat response of 1.5dB/m. Fusion splice with 0.5dB loss has been demonstrated.

6.3.5 Discussion

A gold-implanted fibre polariser has been demonstrated for the first time. The polariser has shown a reasonably good performance. Moreover, it can be mass-produced and spliced easily with low loss to ordinary fibres. The maximum extinction ratio given by a polariser with a 0.5dB insertion loss worked out in practice to be larger than 8.5dB, which compares quite well with the theoretical prediction of 12dB.

6.4 Excitation poling in second-harmonic generation

6.4.1 Background

It was first reported by Bergot et al[17] that by subjecting a fibre core to a poling electric field and at the same time launching blue light into it, a process called excitation poling, a strong permanent second order nonlinearity was obtained. It was postulated that non-centre-symmetrical defect centres were excited by the blue light and subsequently aligned by the electrical field. If efficient SHG can be achieved in fibre, it will provide convenient and inexpensive green or blue sources. It is therefore very interesting to find out more about the physics in the process.

6.4.2 Theory

The second-order nonlinear susceptibility, $\chi^{(2)}$, can generate a wave of sum frequency from two waves of different frequencies. A typical application of this is to generate a second-harmonic wave from a fundamental wave. Assume that a wave of frequency ω and electric field E^{ω} is propagating in a medium with a nonlinear coefficient $d^{2\omega}$, which is related to $\chi^{(2)}$ by

and if the wave is confined to a cross section of area A

$$d^{2\omega} = \frac{\varepsilon_0 \chi^{(2)}}{2} \tag{12}$$

(in m^2) the conversion efficiency for the SHG (second harmonic generation) is given by

$$\eta_{shg} = \left(\frac{2}{Acn}\omega d^{2\omega} L O_m \mathrm{sinc}\left(\frac{\Delta kL}{2}\right)\right)^2 P_\omega \tag{13}$$

where $\Delta k = k^{2\omega} - 2k^{\omega}$ ($k^{2\omega}$ and k^{ω} are the propagation constants for waves at frequencies 2ω and ω respectively) and O_m is the overlap integral between the SH and fundamental wave. The conversion efficiency is governed by the intensity of the fundamental wave, P_ω, the interaction length, L, the overlap integral, O_m, the magnitude of the second-order nonlinearity, $\chi^{(2)}$, and the propagation constant difference, Δk.

A phase-matching criterion can be written as $k^{2\omega}=2k^{\omega}$. If phase-matching between the fundamental and SH waves is achieved, the factor $\mathrm{sinc}^2(\Delta kL/2)$ becomes 1 in equation 6.14. This is the condition for efficient SHG.

A variety of possible methods exist for achieving phase-matching for SHG in optical fibres[18,19,20,21]. These methods mainly fall into two categories: modal-phase-matching and grating-phase-matching. Modal phase-matching involves the selection of appropriate modes for the fundamental and SH waves. It is then possible to use waveguide dispersion to compensate the material chromatic dispersion between the two waves to obtain phase-matching. The pump usually operates at the fundamental mode of the waveguide and the SH wave at one of the higher-order modes. The design requires a high numerical aperture and a precisely controlled V value. Moreover, the overlap integral, O_m, between the phase-matched fundamental mode and the higher-order mode is usually small (about 10%). In grating phase-matching, a grating of period Λ is produced in the fibre, leading to phase-matching if

$$k^{2\omega}-2k^{\omega} = \frac{2m\pi}{\Lambda} \qquad (14)$$

where m is an integer and is usually chosen to be 1. A suitable grating is therefore required. This can be achieved in many different ways[22,23,24].

The fibre was designed to be multi-moded at blue light wavelength and to be D shape with one internal electrode. A novel method based on modal interference gratings of the defect excitation source was used to achieve phase matching. $\chi^{(2)}$ gratings were generated by the stationary interference pattern of blue light inside the multi-mode fibre when poling field was applied. The gratings were permanent. Phase matching between pump and SH waves was therefore achieved when the pump was tuned to the correct wavelength satisfying equation 6.14.

6.4.3 Experiment

The fibre used is gallium-filled and has a germanium-doped core and a NA of 0.3 and becomes single-mode at wavelengths longer than 1.15μm. It is elliptical with an aspect ratio of 3:1. The applied field was aligned with the major axis of the fibre core. A fibre length of 30cm was used. A Raman-shifted dye laser was used as the tunable IR pump. A CW argon at 488nm provided the optical excitation source. By using suitable filters and detectors, simultaneous measurement of the fundamental wave, the SH wave and the excitation power was possible.

The effect of launching an intense infrared light while simultaneously applying a field was investigated first. However, it is found that the SH signal simultaneously

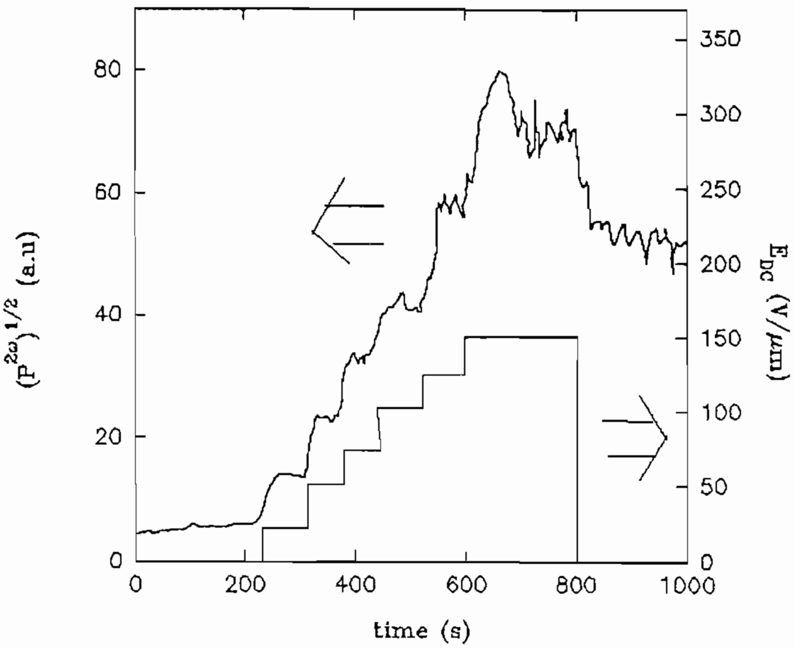

Figure 6.6 Time and poling-fileld dependence of induced $\chi^{(2)}(2\omega=\omega+\omega)$ for a constant launched blue light power of 25mw at 488nm in a Ge-doped fibre

appeared when dc field was on and was very small when the field was off. No permanent $\chi^{(2)}$ was therefore generated. When argon light was launched into the fibre with the poling field on, a permanent $\chi^{(2)}$ was observed. With a fixed CW argon light power of 25mw, the variation of the induced $\chi^{(2)}$ as a function of the poling field intensity was measured. The result is shown in figure 6.6. With a poling field up to 150V/μm, no saturation was observed. The SH power was linear with the applied poling field. The induced nonlinearity was bleachable by launching only blue light into the fibre. The highest SH conversion efficiency was obtained when the launched intensity of the excitation power was 6mw/μm^2. For blue light power greater than this optimum level, the SH conversion efficiency decreases. A maximum SH conversion efficiency of 1% was obtained for an infrared pump power of only 150w. The maximum induced $\chi^{(2)}$ was approximately 10^{-13}m/V.

6.4.4 Discussion

Much of the underlying physics for SHG in fibres remains unclear. In the original experiment of Osterberg et al[25,26], SH signal was observed to grow when a single-mode fibre was exposed to intense YAG pulses for few hours. It was also found that the process was greatly accelerated by adding a small amount of SH to the pump. This was explained by Stolen[27] that a periodic phase-matching $\chi^{(2)}$ can be generated by a periodic field induced by $\chi^{(3)}$ through pump and SH in the presence of centre-symmetry.

$$P_{dc}^{(3)}\,(0=\omega+\omega-2\omega)=\chi^{(3)}E_{\omega}^{2}E_{2\omega}^{*} \qquad \textbf{(15)}$$

Osterberg's observation can be explained as that the tightly confined fibre core possessed an axial asymmetry and thus SH can be generated through the axial gradient of the fibre modes[28]. This process can thus seed itself.

Our experiment confirms the necessity of blue light in the generation of the $\chi^{(2)}$ gratings in the fibre. The novel phase matching method also provides more evidence for the existence of periodic non-centre-symmetrical defect centres produced by combination of blue light and electrical field.

6.5 Spatial mode converter

6.5.1 Background

The value of the single-mode fibre taper in the construction of fibre devices is widely recognised. The changes in fundamental mode size brought about by a taper allow closer matching to the modes of other waveguides, and tapered fibre ends have found widespread use for interconnecting fibres with optical elements such as diode laser[29] and isolators[30].

Previous work on the single-mode fibre taper has been restricted to variations in the taper width only, with a uniformly circular-sectional shape throughout the transition. However, low-loss transitions are possible in which the cross-sectional shape also changes[31]. The realisation of such a transition is reported in this section. In particular, a circular-to-rectangular transition is constructed in a tapered single-mode fibre, in which the fundamental mode is transformed in shape from circular to rectangular.

6.5.2 Theory

It is well established that light entering a single-mode fibre taper spreads out from the core and becomes guided in the fundamental mode of the waveguide formed by the cladding/air interface[32]. This waveguide dominates the guidance of the fundamental mode at taper ratios greater than 3:1. If the taper is sufficiently gradual, little loss accompanies this transition. The cladding waveguide is highly multimode, so the fundamental mode is strongly confined by the cladding and closely follows the shape of the boundary[33]. If the taper cross-section is rectangular then the fundamental mode shape will also be rectangular. Therefore, such a taper functions as a mode shape transformer, in which a circular mode is transformed into a rectangular cladding mode, and vice versa. Fundamentally, a rectangular taper should be no more prone to waveguide transition loss than a conventional circular taper, for a given taper angle. Similar adiabaticity considerations prevails in both cases.

6.5.3 Fabrication

A motor-driven polishing wheel[34] was used to change the circular cross section of a standard single-mode fibre (diameter 125μm, cut-off wavelength 1150nm) into a rectangle. Two parallel sides are polished flat, and these constitute the long sides of the rectangle. The two short sides retain the circular curve of the original fibre cross-section, but the more closely the polished sides approach the fibre core, the more 'rectangular' the cross-section becomes. By polishing each side to the same depth, a symmetrical quasi rectangle is produced. The polished region is then tapered in the conventional manner in a flame, and the throughput loss of the whole transition is monitored.

Rectangularly polished fibres with symmetric and parallel-sided cross-sections can be routinely produced. As would be expected, the polishing process does not introduce any loss prior to tapering. Many rectangular mode transformers were then made by tapering these polished fibres.

6.5.4 Experiment

In a polished rectangular fibre with an aspect ratio of 22:1, the throughput loss of the taper was 0.4dB. The taper ratio was about 4.5:1, which is sufficient to bring about cladding guidance in unpolished fibre. The cladding mode behaviour of the rectangular tapers was confirmed by the application of index matching fluid, leading to a total loss of power.

To investigate whether the circular-to-rectangular transition is in itself a source of loss, a uniformly rectangular fibre (with a circular core) was also tapered to a similar ratio. This nonstandard fibre was fabricated from a rectangular preform, having an aspect ratio of 2.5:1 therefore needing no polishing. A taper throughput loss of less than 0.1dB was readily obtained.

6.5.5 Discussion

In a previous design of mode transformer[35], a single-mode fibre with a rectangular core was fabricated from special soft glasses. The initial rectangular core diffused into a circular shape in part of the fibre after heat treatment, resulting in a core cross-section which gradually varied from a rectangle to a circle along the fibre. However, because the initial rectangular core waveguide was single-mode, the fundamental mode was weakly confined by the core and was near-circular to begin with. The change in the shape of the core therefore had little effect on the mode shape.

In contrast, the tapered mode transformer reported here was made from standard off-the-shelf silica fibre, and because of the highly multi-mode and strongly confining nature of the taper waveguide, there was a true circular-to-rectangular mode transformation. Such transitions should permit more efficient interconnection of fibres and other optical waveguides.

The typical throughput loss for the tapered rectangularly polished fibres is 0.4dB. This is probably due to scattering from the rough polished surfaces; finer polishing should therefore reduce this loss. The circular to rectangular transition in itself does not introduce any further loss, as was demonstrated by tapering the rectangular fibre. The loss of one mode transformer is in any event half the measured throughput loss of the tapered fibre, since each tapered fibre is cleaved at its waist to yield two mode transformers.

The circular-to-rectangular transition discussed here is of particular interest for waveguide interconnection. However, other shape transitions are also possible with this polishing and tapering approach. For instance, a circular-to-semicircular mode transformer has been fabricated with the above technique, and may give low-loss joints between fibres and ion-diffused waveguides, in which the modal fields can be semicircular in shape.

6.6 Summary

In this chapter, we investigated TC cascaded filters, gold-implanted fibre polarisers, excitation poling in SHG and spatial mode converters. They are all vital components in optical fibre systems. Specially structured fibres have been used in these devices. A cascaded TC filter of 17nm has been fabricated, proving the possibility of the technique, but the filter performance is limited by the perturbation sensitivity of TC fibres. A gold-metal implanted fibre polariser has been demonstrated for the first time, with the advantages of easy mass-manufacturing and splicing with good extinction ratio and better insertion loss. Excitation poling in SHG has yielded 1% conversion efficiency; although far from being practical, it represents, nevertheless, a potential way of producing visible or even UV source from a IR laser. The spatial mode converter also provides a low-loss way of interconnecting waveguides with different spatial modes. These devices, although not yet very practical in some ways and needing further research and development, have large potential in many applications.

References

1 K. Okamoto and J. Nova: "Fibre-optic spectral filters consisting of concatenated dual-core fibres, Electronics Letters, **22**, No.4, 1986, pp.211-212.

2 L. Li, G. Wylangowski, D.N. Payne and R.D. Birch: "Low cost metal/glass fibre polarisers produced in continuous length", 4th International Conference on OFS, Tokyo, Japan, October, 1986.

3 L. Li, R.D. Birch, and D.N. Payne: "High performance composite metal/glass fibre polariser", 12th ECOC, Bacelona, Spain, September, 1986.

4 Y. Yamamoto, T. Kamiya and H. Yanai: "Characteristics of optical guided modes in multi-layer metal-clad planar optical guide with low-index dielectric buffer layer", IEEE Journal of Quantum Electronics, **QE-11**, 1975, pp.729-736.

5 C. Vassallo: "Rigorous theory for modes of optical fibres with cladding limited by a plane", Electronics Letters, **22**, No.18, 1986, pp.944-945.

6 Y. Tong and W. Yizun: "Theoretical study of metal-clad optical waveguide polariser", IEEE Journal of Quantum Electronics, **25**, 1989, pp.1209-1213.

7 A. Reisinger: "Characteristics of optical guided modes in lossy waveguides" Applied Optics, **12**, 1973.

8 F. Yang, Z. Cao, L. Ruan and J. Fang: "Long-range surface modes of metal-clad four-layer waveguides", Applied Optics, **25**, 1986, pp.3903-3908.

9 P. Varnham, D.N. Payne, A.J. Barlow and E.J. Tarbox: "Coiled-birefringent-fibre polarisers", Optics Letters, **9**, 1984, pp.306-308.

10 K.Okamato and J. Noda: "High-birefringence polarising fibre with flat cladding", Journal of Lightwave Technology, **LT3**, 1985, pp.758-762.

11 W. Eickoff: "In-line fibre-optic polariser", Electronics Letters, **16**, 1980, pp.758-762.

12 J.R. Feth, C.L. Chang and L.F. Stokes: "A novel in-line single-mode fibre optic polariser", SPIE Conference, San Diego, August, 1985.

13 T. Hosaka, K. Okamoto and T. Edahiro "Fabrication of single-mode fibre-type polariser", Optics Letters, **8**, 1983, pp.124-126.

14 C.Y. Tsao, L. Li and D.N. Payne: "Propagation characteristics of guided waves in stratified metallic optical waveguides", Applied Optics, **27**, 1988, pp.1316-1325.

15 C.A. Miller, B.J. Ainsilie, M.C. Brierley and S.P. Caig: "Fabrication and characterisation of D-fibres with a range of accurately controlled core/fl distances", Electronics Letters, **18**, 1982, pp.980-981.

16 W.M. Henry and J.D. Love: "Mismatch limitations on

metal-fibre polarisers", Optical and Quantum Electronics, **21**, 1989, pp.205-214.

17 M.V. Bergot, M.C. Farries, M.E. Fermann, L. Li, L.J. Poynz-Wright, P.StJ. Russell and A. Smithson: "Generation of permanent optically-induced second-order nonlinearities in optical fibres by poling", Optics Letters, **13**, 1988, pp.592-594.

18 Y.R. Shen: "The principles of nonlinear optics", John Wiley and sons, 1984.

19 Y. Sasaki and Y. Ohmori: "Phase-matched sum-frequency light generation in optical fibres", Applied Physics Letters, **39**, 1982, pp.466-468.

20 U. Osterberg and W. Margulis: "Effective second harmonic generation in an optical fibre", 14th International Quantum Electronics Conference, San Francisco, 1986, WBB2.

21 F. P. Payne: "Second-harmonic generation in single-mode optical fibres", Electronics Letters, **23**, 1987, pp.1215-1216.

22 K.O. Hill, Y. Fujii, D.C. Johnson and B.S. Kawasaki: "Photosensitivity in optical fibre waveguides: Application to reflection filter fabrication", Applied Physics Letters, **32**, 1978, pp.647-65

23 P.St.J. Russell and R. Ulrich: "Grating-fibre coupler as a high-resolution spectrometer", Optics Letters, **10**, 1985, pp.291-293.

24 D. Gloge: "Weakly guided fibres", Applied Optics, **10**, pp.2252-2258.

25 U. Osterberg and W. Margulis: "Dye laser pumped by Nd:YAG laser pulses frequency doubled in a glass optical fibre", Optics Letters, **11**, 1986, pp.516-518.

26 U. Osterberg and W. Margulis: "Experimental studies on efficient frequency doubling in glass optical fibres", Optics Letters, **12**, 1987, pp.57-59.

27 R.H. Stolen and H.W.K. Tom: "Self-organized phase-matched harmonic generation in optical fibres", Optics Letters, **12**, 1987, pp.585-587.

28 F.P. Payne: "Frequency-doubling in single mode fibres", Electronic Letters, **23**, 1987, pp.1215-1217.

29 T.Schwander, B. Schwaderer, and H. Storm: "Coupling of lasers to single-mode fibres with high efficiency and low optical feedback", Electronics Letters, **21**, 1985, pp.287-289.

30 K.J. Warbrick: "Design of a compact optical isolator", IEE Colloquium on All-fibre Devices, London, 1988, pp.5/5/4.

31 C.D. Hussey and T.A. Birks: "Fabrication of wavelength-flattened tapered couple using polishing for cladding removal", Electronics Letters, **24**, 1988, pp.1072-1073.

32 K.P. Jedrzejewski, F. Martinez, J.D. Minelly, C.D.Hussey, and F.P. Payne: "Tapered-beam expander for single-mode optical-fibre gap devices", Electronics Letters, **22**, 1986, pp.600-609.

33 A.W. Snyder and X.H. Zhang: "Optical fibres of arbitrary cross sections", Journal of the Optical Society of America A, **3**, 1986, pp.600-609.

34 C.D. Hussey and J.D. Minelley: "Optical fibre polishing with a motor-driven polishing wheel", Electronics Letters, **24**, 1988, pp.805-807.

35 K. Shigihara, k. Shiraishi and S. Kaakami: "Modal field transformer between dissimilar waveguides", European Conference on Optical Communication, Barcelona, 1986, pp.185-188.

Chapter Seven Conclusions

7.1 Summary of the thesis

In chapter two of the thesis, light propagation in twin core fibres was analyzed with coupled-mode theory. Both identical-core TC fibres and near-identical-core fibres were treated. Periodically perturbed TC fibres were also investigated using a method based on grating assisted coupling between the normal modes of the unperturbed TC fibre. TC fibres with gain were also analyzed based on coupling between normal modes of the unperturbed TC fibre.

A novel technique for fabrication of TC fibres with low loss and better controlled parameters was presented. Light propagation in three identical-core TC fibres was investigated experimentally. The theory agreed well with the experimental data for weakly coupled fibres ($\kappa<200m^{-1}$). In strongly coupled fibres, the theory predicted a smaller coupling than experimental data, due to the fact that the superposition of the fundamental modes in the two isolated cores is no longer a good approximation to the normal modes of the TC fibres. Perturbation sensitivity of TC fibres was also investigated. Weakly coupled TC fibres of long length were much more sensitive to slight bending. Strongly-coupled TC fibres with short lengths are therefore preferred in stable TC fibre devices.

In chapter three, photosensitivity in two kinds of fibres was investigated. In transition-metal-doped fibres, the effect of CW argon laser radiation on the fibre transmission was measured. A creation of defect centres was observed, causing an increase in UV absorption. No change in the oxidation states of the transition-metal ions, however, was observed. The possibility of photo-bleaching in a Fe^{2+}-doped fibre with radiation from a YAG laser was investigated. A CW photon flux over the theoretical prediction was launched into fibre, without sign of bleaching. A pulsed YAG with much higher power (200W peak power) was also tested, without success. The bleaching is believed either to happen at a much higher power level, or to have a much faster recovery time (less than tens of nano-seconds).

Photosensitivity in Ce^{3+}-doped fibre was also investigated. The fibre index was observed to change by as much as 10^{-4} when exposed to UV light at 266nm and 355nm. This effect is useful for writing gratings in fibre cores by forming interference pattern on side of the fibre and is of great importance in single-frequency fibre lasers, wavelength-multiplexing telecommunications and fibre sensors. The 266nm light was also found to give a much larger effect than 355nm light. This effect was identified to be a single-photon process and Ce^{3+}-related. A broad band loss from UV to IR was also observed upon UV exposure, and recovered totally with time. A slow modulator was demonstrated, where light transmission at 632.8nm was modulated by a light at 266nm. The induced loss at 632.8nm was found to be linear with UV intensity. The induced index change was found to saturate at high UV intensity, but to increase almost linearly with Ce^{3+} concentration. The index change dropped off at longer wavelengths ($>1.0\mu m$). The Ce^{3+} absorption peak was observed to be reduced on UV exposure and a Ce^{4+} peak was found to appear. The change in cerium absorption was seen to be stable for at least several months. The index change that results from the induced absorption change, calculated by Kramers-Kronig relation, are an order of magnitude too small.

In chapter four, the techniques for fabricating electroded fibres, solid-metal-implanted fibres and fibres with special waveguide structures was discussed. Fibre designs and methods of fabrication were described. These fibres have found their applications in fibre polarisers, modulators, excitation poling in second harmonic generations, high power lasers and couplers. These techniques are also versatile for fabricating many other fibre devices for a variety of applications.

In chapter five, periodically-perturbed TC fibre modal couplers were investigated experimentally. Total intermodal coupling in non-identical-core TC fibres by a mechanical grating and fibre acoustic flexural wave was demonstrated for the first time. The tunability of the devices by varying perturbation pitch was also studied. In the mechanical grating case, the measured coupling bandwidth was broader than that predicted by the theory, indicating a non-uniformity in the grating along the fibre. In the acoustic flexural case, the coupling bandwidth fits well with theoretical prediction, indicating a uniform perturbation pitch along the fibre. The frequency shift by an acoustic flexural wave was also measured. Carrier and side-band suppression ratios were measured to be 11dB and 4.5dB. The carrier suppression was affected by the large intrinsic coupling (3%) and the side-band suppression by the 91mm of fibre on the other side of the acoustic horn in the experiment. 100% coupling was achieved using the fibre with 3% intrinsic coupling with an electric driving power of 200mW. These devices have the advantage of easier incorporation into a single mode fibre system than devices based on two lower order modes or polarised modes in fibres. They can be spliced with ordinary fibres with very low loss (0.1dB demonstrated) and be used as filters, switches, and signal taps in wavelength-multiplexing systems.

In chapter six, cascaded TC filters, gold-implanted fibre polarisers, excitation poling in second harmonic generation and spatial mode converters were investigated. These devices are important components in an optical fibre system. A cascaded TC filter of 16nm bandwidth and 15dB extinction ratio was fabricated, but filters with better performances were found to be limited by the perturbation sensitivity of TC fibres. The results obtained fit well with the theoretical predictions. A gold-implanted polariser was demonstrated for the first time. The device has the advantage of relatively easy mass-manufacturing and low splice losses with good extinction ratio. Excitation poling in the second harmonic generation was investigated with 1% conversion efficiency achieved. Although still far from being practical, it nevertheless demonstrates a potential way to produce visible or even UV laser sources. A spatial mode converter was also demonstrated for converting a circular mode to a rectangular mode with very low insertion loss (0.2dB), thus providing a connection between circular fibres and rectangular planar waveguides. These devices, although not yet practical in many ways, have a large potential of being used in many applications in future optical fibre systems.

7.2 Future work

An erbium-doped TC fibre amplifier with gain compensation has been proposed, in which the dispersive nature of a TC fibre is exploited to produce differential gain for signals at different wavelengths. In a TC fibre, even signals with very close wavelength spacings follow individual paths. If a signal is large enough to cause gain saturation, that signal will see a smaller gain than any other signals due to the other signals propagating on different paths and thus seeing a smaller saturation effect. This amplifier would be able to produce an equal power output for signals at different wavelengths. A high NA fibre would be required to lower the signal saturation threshold and a short beatlength (<1mm) would also be necessary to shorten the device length.

Another proposal which has been put forward is to mode-lock a fibre laser with an in-line frequency shifter. The 5MHz frequency shift is matched to the cavity mode spacing thus the laser cavity modes are coupled among each other and therefore locked together. A broad band in-line frequency shifter is possible by careful shifter design and narrow pulses should therefore be possible from this laser.

The fabrication of fibre gratings in cerium-doped fibres would allow comparisons with germanium-doped fibre gratings to be made. An improved nonlinearity may be possible in this fibre if higher dopant levels can be achieved.

Appendix A The Derivation of Coupled-mode Equations in a TC Fibre

The fundamental modes in a TC fibre can be well approximated by the summation of the fundamental modes of the two isolated cores, if the cores are well separated.

$$E = V_1(z)E_{10} + V_2(z)E_{20} \tag{A.1}$$

E_{10} and E_{20} are the fundamental modes of the isolated cores 1 and 2 respectively.

$$E_{10} = a_1(x,y)\,e^{j\beta_1 z} \tag{A.2}$$

$$E_{20} = a_2(x,y)\,e^{j\beta_2 z} \tag{A.3}$$

In equations A.2 and A.3, $a_{1,2}$ and $\beta_{1,2}$ are the transverse field distribution and propagation constant respectively. E_{10} and E_{20} should satisfy Maxwell's equation, therefore

$$[\nabla^2 + (n_{cl}k)^2(1+2\Delta_1(x,y))]E_{10} = 0 \tag{A.4}$$

$$[\nabla^2 + (n_{cl}k)^2(1+2\Delta_2(x,y))]E_{20} = 0 \tag{A.5}$$

In equations A.4 and A.5, n_{cl} is the cladding refractive index, k is the vacuum wave number, and $\Delta_{1,2}(x,y)$ are defined as the relative index-difference distribution of the isolated fibres, i.e. $\Delta_1=(n_{co1}-n_{cl})/n_{cl}$ over core 1 and $\Delta_1=0$ elsewhere (n_{co1} is the refractive index of core 1). Higher orders of $\Delta_{1,2}$ have been neglected in equations A.4 and A.5.

In a TC fibre, field E described in equation A.1 should satisfy Maxwell's equation.

$$[\nabla^2 + (n_{cl}k)^2(1+2\Delta(x,y))](V_1(z)E_{10} + V_2(z)E_{20}) = 0 \tag{A.6}$$

In equation A.6, $\Delta(x,y)$ is the relative index-difference distribution of the TC fibre, i.e. $\Delta=(n_{co1}-n_{cl})/n_{cl}$ over core 1, $\Delta=(n_{co2}-n_{cl})/n_{cl}$ over core 2 and $\Delta=0$ elsewhere. By using

$$\nabla^2(V_pE_{po}) = V_p\nabla^2E_{po}+2\nabla E_{po}\nabla V_p+E_{po}\nabla^2 V_p \tag{A.7}$$

where p=1 or 2 and

$$\Delta = \Delta_1+\Delta_2 \tag{A.8}$$

equation A.6 can be simplified to

$$\begin{aligned}&2\nabla E_{10}\nabla V_1+E_{10}\nabla^2V_1+2\nabla E_{20}\nabla V_2+E_{20}\nabla^2V_2\\&+2(n_{cl}k)^2\Delta_2V_1E_{10}+2(n_{cl}k)^2\Delta_1V_2E_{20}=0\end{aligned} \tag{A.9}$$

If we assume the modal amplitudes, $V_1(z)$ and $V_2(z)$, change slowly then the second-order derivatives of $V_1(z)$ and $V_2(z)$ can be neglected. Using equations A.4 and A.5, equation A.9 becomes

$$\begin{aligned}&2ja_1\nabla(\beta_1z)\nabla V_1e^{j\beta_1z}+2ja_2\nabla(\beta_2z)\nabla V_2e^{j\beta_2z}\\&+2(n_{cl}k)^2\Delta_2V_1a_1e^{j\beta_1z}+2(n_{cl}k)^2\Delta_1V_2a_2e^{j\beta_2z}=0\end{aligned} \tag{A.10}$$

By multiplying equation A.10 by E_{10}^* and integrating it over the whole cross-section of the fibre, $A\infty$, we obtain equation A.11.

$$\begin{aligned}&2j\beta_1\frac{dV_1}{dz}\int_{A\infty}a_1a_1dA+2j\beta_2\frac{dV_2}{dz}e^{j(\beta_2-\beta_1)z}\int_{A\infty}a_1a_2dA+\\&2(n_{cl}k)^2V_1\int_{A\infty}\Delta_2a_1a_1dA+2(n_{cl}k)^2V_2e^{j(\beta_2-\beta_1)z}\int_{A\infty}\Delta_1a_1a_2dA=0\end{aligned} \tag{A.11}$$

Equation A.11 can be written as

$$\frac{dV_1}{dz}+\kappa_{12}^{(2)}e^{j(\beta_2-\beta_1)z}\frac{dV_2}{dz}-j\kappa_{11}V_1-j\kappa_{12}e^{j(\beta_2-\beta_1)z}V_2=0 \tag{A.12}$$

In equation A.12,

$$\kappa_{11} = \frac{(n_{cl}k)^2}{\beta_1} \frac{\int_{A\infty} \Delta_2 a_1 a_1 dA}{\int_{A\infty} a_1 a_1 dA} \tag{A.13}$$

$$\kappa_{12} = \frac{(n_{cl}k)^2}{\beta_1} \frac{\int_{A\infty} \Delta_1 a_1 a_2 dA}{\int_{A\infty} a_1 a_1 dA} \tag{A.14}$$

$$\kappa_{12}^{(2)} = \frac{\beta_2}{\beta_1} \frac{\int_{A\infty} a_1 a_2 dA}{\int_{A\infty} a_1 a_1 dA} \tag{A.15}$$

Similarly, if equation A.10 is multiplied by E_{20}^* and integrated over the whole cross-section of the fibre, we obtain equation A.16.

$$\frac{dV_2}{dz} + \kappa_{21}^{(2)} e^{j(\beta_1-\beta_2)z} \frac{dV_1}{dz} - j\kappa_{21} e^{j(\beta_1-\beta_2)z} V_1 - j\kappa_{22} V_2 = 0 \tag{A.16}$$

In equation A.16,

$$\kappa_{22} = \frac{(n_{cl}k)^2}{\beta_2} \frac{\int_{A\infty} \Delta_1 a_2 a_2 dA}{\int_{A\infty} a_2 a_2 dA} \tag{A.17}$$

$$\kappa_{21} = \frac{(n_{cl}k)^2}{\beta_2} \frac{\int_{A\infty} \Delta_2 a_1 a_2 dA}{\int_{A\infty} a_2 a_2 dA} \tag{A.18}$$

$$\kappa_{21}^{(2)} = \frac{\beta_1}{\beta_2} \frac{\int_{A\infty} a_1 a_2 dA}{\int_{A\infty} a_2 a_2 dA} \tag{A.19}$$

$\kappa_{12}^{(2)}$ and $\kappa_{21}^{(2)}$ are very small comparing with the rest of the coefficients in equations A.12 and A.16. They are neglected in the following analysis. Since the cores are well separated, $a_{1,2}$ are small over the other core . The self-coupling coefficients κ_{11} and κ_{22} are also negligible comparing with the cross-coupling coefficients, κ_{12} and κ_{21}. Therefore they are also neglected. Equations A.12 and A.16

become

$$\frac{dV_1}{dz} - j\kappa_{12} e^{j(\beta_2-\beta_1)} V_2 = 0 \tag{A.20}$$

$$\frac{dV_2}{dz} - j\kappa_{21} e^{j(\beta_1-\beta_2)} V_1 = 0 \tag{A.21}$$

Appendix B The Analysis of Periodically Perturbed TC Fibres

In appendix A, we derived the coupled-mode equations for TC fibres from Maxwell equations and fundamental modes of the two isolated fibres. In this section, we will analyze the situation where a TC fibre is periodically perturbed. Normal modes of the TC fibre are used in the analysis, which give a better insight into the coupling between the real modes of the waveguide. These normal modes have already been derived in the chapter two and can therefore be used to complete the analysis.

The normal modes in an unperturbed TC fibre can be written as

$$E_q = a_q(x,y)\, e^{j\beta_q z} \qquad \textbf{(B.1)}$$

where q=e or o and represents even and odd modes of the TC fibre respectively. In a periodically perturbed TC fibre, the field can be described by a superposition of the unperturbed fibre modes with slow axially varying amplitudes.

$$E = V_e(z)\, E_e + V_o(z)\, E_o \qquad \textbf{(B.2)}$$

If the relative refractive index distribution of the perturbed fibre can be described as

$$\Delta(x,y) = \Delta_0(x,y) + \Delta^p(x,y)\cos(k_p z) \qquad \textbf{(B.3)}$$

where Δ_0(x,y) is the relative index distribution of the unperturbed fibre, E will satisfy the Maxwell equation

$$[\nabla^2+(n_{cl}k)^2(1+2\Delta)]E=0 \tag{B.4}$$

The two normal modes in equation B.1 satisfy the Maxwell equation for the unperturbed TC fibre, therefore

$$[\nabla^2+(n_{cl}k)^2(1+2\Delta_0)]E_q=0 \tag{B.5}$$

where q=e or o. Combining equations B.4 and B.5 we have

$$\begin{aligned}&E_e\nabla^2V_e+2\nabla V_e\nabla E_e+2(n_{cl}k)^2\Delta^p\cos(k_pz)V_eE_e+\\&E_o\nabla^2V_o+2\nabla V_o\nabla E_o+2(n_{cl}k)^2\Delta^p\cos(k_pz)V_oE_o=0\end{aligned} \tag{B.6}$$

V_q (q=e,o) varies slowly, we can therefore ignore higher order derivatives of V_q.

$$\begin{aligned}&\frac{dV_e}{dz}a_e(j\beta_e)e^{j\beta_e z}+(n_{cl}k)^2\Delta^p\cos(k_pz)V_eE_e+\\&\frac{dV_o}{dz}a_o(j\beta_o)e^{j\beta_o z}+(n_{cl}k)^2\Delta^p\cos(k_pz)V_oE_o=0\end{aligned} \tag{B.7}$$

By multiplying equation B.7 by E^*_e and integrating it over the cross-section of the fibre, A_∞, we have

$$\frac{dV_e}{dz}-j\kappa_{ee}\cos(k_pz)V_e-j\kappa_{eo}\cos(k_pz)e^{j(\beta_o-\beta_e)z}V_o=0 \tag{B.8}$$

where

$$\kappa_{ee} = \frac{(n_{cl}k)^2}{\beta_e}\frac{\int_{A\infty}\Delta^p a_e^2 dA}{\int_{A\infty} a_e^2 dA} \tag{B.9}$$

$$\kappa_{eo} = \frac{(n_{cl}k)^2}{\beta_e}\frac{\int_{A\infty}\Delta^p a_e a_o dA}{\int_{A\infty} a_e^2 dA} \tag{B.10}$$

By multiplying equation B.7 by E^*_o and integrating it over the cross section of the fibre, we have

$$\frac{dV_o}{dz} - j\kappa_{oo}\cos(k_p z)\,V_o - j\kappa_{oe}\cos(k_p z)\,e^{j(\beta_e-\beta_o)z}V_e = 0 \tag{B.11}$$

where

$$\kappa_{oo} = \frac{(n_{cl}k)^2}{\beta_o}\frac{\int_{A\infty}\Delta^p a_o^2 dA}{\int_{A\infty} a_o^2 dA} \tag{B.12}$$

$$\kappa_{oe} = \frac{(n_{cl}k)^2}{\beta_o}\frac{\int_{A\infty}\Delta^p a_o a_e dA}{\int_{A\infty} a_o^2 dA} \tag{B.13}$$

Equations B.8 and B.11 define the solutions of $V_q(z)$ $(q=e,o)$ and can be further written as

$$\frac{dV_e}{dz}-\frac{j}{2}(e^{-jk_pz}+e^{jk_pz})\,\kappa_{ee}V_e-\frac{j}{2}(e^{j(\beta_o-\beta_e-k_p)z}+e^{j(\beta_o-\beta_e+k_p)z})\,\kappa_{eo}V_o=0 \tag{B.14}$$

$$\frac{dV_o}{dz}-\frac{j}{2}(e^{-jk_pz}+e^{jk_pz})\,\kappa_{oo}V_o-\frac{j}{2}(e^{j(\beta_e-\beta_o-k_p)z}+e^{j(\beta_e-\beta_o+k_p)z})\,\kappa_{oe}V_e=0 \tag{B.15}$$

The complete solutions of equations B.14 and B.15 are too complicated, however, asymptotic solutions are much easier to obtain. If we consider only the slowest components (varying with a frequency of $\beta_e-\beta_o-k_p$) in these equations, the equations become

$$\frac{dV_e}{dz}-\frac{j}{2}e^{-j(2\beta_b-k_p)z}\kappa_{eo}V_o=0 \tag{B.16}$$

$$\frac{dV_o}{dz}-\frac{j}{2}e^{j(2\beta_b-k_p)z}\kappa_{oe}V_e=0 \tag{B.17}$$

where

$$\beta_b=\frac{\beta_e-\beta_o}{2} \tag{B.18}$$

By cancelling out V_e in equations B.16 and B.17, we have

$$\frac{d^2V_e}{dz^2}+j(2\beta_b-k_p)\frac{dV_e}{dz}+\frac{\kappa_{eo}\kappa_{oe}}{4}V_e=0 \tag{B.19}$$

V_e can therefore be solved from equation B.19 and V_o can be obtained form equation B.16.

$$V_e = Ae^{j(\frac{\sigma}{2}-\frac{\kappa^p}{F_p})z} + Be^{j(\frac{\sigma}{2}+\frac{\kappa^p}{F_p})z} \tag{B.20}$$

$$V_o = \frac{2}{\kappa_{eo}}[A(-\frac{\sigma}{2}-\frac{\kappa^p}{F_p})e^{j(\frac{\sigma}{2}-\frac{\kappa^p}{F_p})z} + B(-\frac{\sigma}{2}+\frac{\kappa^p}{F_p})e^{j(\frac{\sigma}{2}+\frac{\kappa^p}{F_p})z}] \tag{B.21}$$

where

$$\sigma = 2\beta_b - k_p \tag{B.22}$$

$$\kappa^p = \frac{\sqrt{\kappa_{oe}\kappa_{eo}}}{2} \tag{B.23}$$

$$F_p = \frac{1}{\sqrt{1+\frac{\sigma^2}{4\kappa^{p^2}}}} \tag{B.24}$$

Follow the same way as in section 2.2.4 for a near-identical TC fibre. We are able to obtain the power in the fibre cores for initial condition of $p_1(0)=1$ and $p_2(0)=0$.

$$p_1(z) = 1-F_p^2\sin^2(\frac{\kappa^p z}{F_p}) \tag{B.25}$$

$$p_2(z) = F_p^2\sin^2(\frac{\kappa^p z}{F_p}) \tag{B.26}$$

Appendix C The Analysis of TC Fibres with Gain

We introduce a complex refractive index for the case of a TC fibre with gain.

$$\eta = n(1+j\chi) \tag{C.1}$$

where n and $n\chi$ are the real and imaginary parts of the refractive index respectively. If the power in the fibre can be written as $p=p_0e^{\delta z}$, where δ is called the gain coefficient, therefore

$$\delta = \frac{2\omega n\chi}{c} \tag{C.2}$$

where ω is the angular frequency of the propagating wave. For a weakly guided fibre, we define the relative refractive index distribution as

$$\Delta(x,y) = \Delta_0(x,y) + j[1+\Delta_0(x,y)]\chi(x,y) \tag{C.3}$$

where $\Delta_0(x,y)$ is the relative refractive index distribution of the same fibre without gain, which is zero in the cladding and only non-zero over the two cores. If we assume the two normal modes of the TC fibre without gain are

$$E_q = a_q(x,y)\, e^{j\beta_q z} \tag{C.4}$$

where q=e,o, the field in the TC fibre with gain can be expressed as

$$E = V_e(z)\,E_e + V_0(z)\,E_o \tag{C.5}$$

It satisfies the following Maxwell equation

$$[\nabla^2 + (n_{cl}k)^2[1+2\Delta_0+2j(1+\Delta_0)\chi]]\,E = 0 \tag{C.6}$$

In the TC fibre without gain, we have the following equations for the normal modes.

$$[\nabla^2+(n_{cl}k)^2(1+2\Delta_0)]E_q=0 \tag{C.7}$$

where q=e,o. By substituting equation C.7 into equation C.6 and ignoring the higher derivatives of the slowly varying $V_q(z)$ (q=e,o), we have

$$\frac{dV_e}{dz}a_e(j\beta_e)e^{j\beta_e z}+\frac{dV_o}{dz}a_o(j\beta_o)e^{j\beta_o z}+ \\ j(1+\Delta_0)\chi(n_{cl}k)^2V_e a_e E^{j\beta_e z}+j(1+\Delta_0)\chi(n_{cl}k)^2V_o a_o e^{j\beta_o z}=0 \tag{C.8}$$

By multiplying equation C.8 by E_q^* (q=e,o) and integrating it over the cross section of the fibre, A∞, we obtain

$$\frac{dV_e}{dz}+\kappa_{ee}V_e+\kappa_{eo}e^{j(\beta_o-\beta_e)z}V_o=0 \tag{C.9}$$

$$\frac{dV_o}{dz}+\kappa_{oe}e^{j(\beta_e-\beta_o)z}V_e+\kappa_{oo}V_o=0 \tag{C.10}$$

where

$$\kappa_{ee}=\frac{(n_{cl}k)^2}{\beta_e}\frac{\int_{A\infty}(1+\Delta_0)\chi a_e^2dA}{\int_{A\infty}a_e^2dA} \tag{C.11}$$

$$\kappa_{eo}=\frac{(n_{cl}k)^2}{\beta_e}\frac{\int_{A\infty}(1+\Delta_0)\chi a_e a_o dA}{\int_{A\infty}a_e^2dA} \tag{C.12}$$

$$\kappa_{oe}=\frac{(n_{cl}k)^2}{\beta_o}\frac{\int_{A\infty}(1+\Delta_0)\chi a_o a_e dA}{\int_{A\infty}a_o^2dA} \tag{C.13}$$

$$\kappa_{oo}=\frac{(n_{cl}k)^2}{\beta_o}\frac{\int_{A\infty}(1+\Delta_0)\chi a_o^2dA}{\int_{A\infty}a_o^2dA} \tag{C.14}$$

By assuming the solutions take the following form

$$V_e(z)=Ae^{-\kappa_{ee}z}W_e(z) \tag{C.15}$$

$$V_o(z) = Be^{-\kappa_{oo}z}W_o(z) \tag{C.16}$$

where A and B are constants and substituting them into equations C.9 and C.10, we have

$$\frac{dW_e}{dz} + \frac{\kappa_{eo}}{C} e^{(\Delta\kappa - j\Delta\beta)z} W_o = 0 \tag{C.17}$$

$$\frac{dW_o}{dz} + \kappa_{oe} C e^{-(\Delta\kappa - j\Delta\beta)z} W_e = 0 \tag{C.18}$$

where $\Delta\kappa=\kappa_{ee}-\kappa_{oo}$, $\Delta\beta=\beta_e-\beta_o$ and C=A/B. $W_q(z)$ (q=e,o) can be obtained from equations C.17 and C.18.

$$W_e = D_1 e^{r_1 z} + D_2 e^{r_2 z} \tag{C.19}$$

$$W_o = -\frac{C}{\kappa_{eo}} (D_1 r_1 e^{-r_1 z} + D_2 r_2 e^{-r_2 z}) \tag{C.20}$$

where D_1 and D_2 are constants to be determined by the initial conditions, and

$$r_{1,2} = \kappa_x(-jl \pm \sqrt{1-l^2}) \tag{C.21}$$

where

$$\kappa_x = \sqrt{\kappa_{oe}\kappa_{eo}} \tag{C.22}$$

$$l = \frac{j\Delta\kappa + \Delta\beta}{2\sqrt{\kappa_{oe}\kappa_{eo}}} \tag{C.23}$$

From equations C.5, C.15, C.16, C.19, and C,20, we have

$$\begin{aligned} E = e^{\frac{-\kappa_t + j\beta_t}{2}z} [&E_1 (a_e - a_o \frac{r_1}{\kappa_{eo}}) e^{\kappa_x\sqrt{1-l^2}z} + \\ &E_2 (a_o + a_e \frac{r_1}{\kappa_{oe}}) e^{-\kappa_x\sqrt{1-l^2}z}] \end{aligned} \tag{C.24}$$

where E_1 and E_2 are constants to be determined by the initial conditions and

$$\kappa_t = \kappa_{ee}+\kappa_{oo} \tag{C.25}$$

$$\beta_t = \beta_e+\beta_o \tag{C.26}$$

For fibres with gain < 100dB/m, $\chi<10^{-5}$. χ is thus two orders of magnitude smaller than Δ_0, and κ_x is two order of magnitude smaller than $\Delta\beta$ (see equations 2.9, 2.12, 2.33, 2.36, C.12, C.13 and C.22). We can then deduce $|l|>100$ and

$$\sqrt{1-l^2} \approx jl-\frac{j}{2l} \tag{C.27}$$

E can then written as

$$E = E_1\left(a_e+\frac{ja_o}{2l}\sqrt{\frac{\kappa_{oe}}{\kappa_{eo}}}\right)e^{\left(-\kappa_{ee}+j\beta_e-j\frac{\kappa_x}{2l}\right)z}+ E_2\left(a_o-j\frac{a_e}{2l}\sqrt{\frac{\kappa_{eo}}{\kappa_{oe}}}\right)e^{\left(-\kappa_{oo}+j\beta_o+j\frac{\kappa_x}{2l}\right)z} \tag{C.28}$$

The two normal modes of the TC fibre with gain are represented by the first and second terms in equation C.28 respectively.

Appendix D The Table of Relevant Fibres

Fibre Name	Descriptions
TM1	Fe^{3+}-doped fibres with a GeO_2/SiO_2 core and NA=0.21; Fe_2O_3 concentration is about 130ppm(wt).
TM2	Cu^{1+}-doped fibres with a GeO_2/SiO_2 core and NA=0.15.
TM3	Mn^{3+}-doped fibres with a GeO_2/SiO_2 core and NA=0.17; Mn_2O_3 concentration is about 190ppb(wt).
TM4	Mn^{3+}/Fe^{2+}-doped fibres with a GeO_2/SiO_2 core and NA=0.17; Mn_2O_3 and FeO concentrations are 220ppb(wt) and 1100ppb(wt) respectively.
RE1	Ce^{3+}-doped fibres with a $Al_2O_3/P_2O_5/SiO_2$ core and NA=0.13; Ce^{3+} concentration is 11,700ppm.
RE2	Ce^{3+}-doped fibres with a $Al_2O_3/P_2O_5/SiO_2$ core and NA=0.19; Ce^{3+} concentration is 5,800ppm.
RE3	Ce^{3+}-doped fibres with a $Al_2O_3/P_2O_5/SiO_2$ core and NA=0.18; Ce^{3+} concentration is 1,900ppm.
RE4	fibres with a $Al_2O_3/P_2O_5/SiO_2$ core and NA=0.21.
TC1	a twin-core fibre with $\rho_1=\rho_2=1.76\mu m$, $\Delta_1=\Delta_2=0.00233$ and $d=10\mu m$.
TC2	a twin-core fibre with $\rho_1=\rho_2=2.5\mu m$, $\Delta_1=\Delta_2=0.00233$ and $d=14\mu m$.
TC3	a twin-core fibre with $\rho_1=\rho_2=4.22\mu m$, $\Delta_1=\Delta_2=4.22\mu m$ and $d=21\mu m$.
TC4	twin-core fibres with one core composed of P_2O_5/SiO_2 and the other core the same as RE1.
TC5	twin-core fibres with one core composed of P_2O_5/SiO_2 and the other core the same as RE2.
TC6	twin-core fibres with one core composed of P_2O_5/SiO_2 and the other core the same as RE3.

TC7	twin-core fibres with one core composed of P_2O_5/SiO_2 and the other the same as RE4.
TC8	a twin-core fibre with ρ_1=1.1μm, ρ_2=0.91μm, Δ_1=Δ_2=0.144, d=5.5μm and a fibre diameter of 110μm.
TC9	a twin-core fibre with ρ_1=1.93μm, ρ_2=1.66μm, Δ_1=Δ_2=0.00521, d=6.5μm, and a fibre diameter of 90μm.
S1	a Gold-implanted fibre with a NA of 0.12, a core/gold distance of 2μm and a gold diameter of 20μm.
S2	a Gallium-implanted fibre with a GeO_2/SiO_2 core, a NA of 0.3 and a core diameter of 3.0μm.
S3	a rectangular fibre with a NA of 0.15 and an aspect ratio of 2.5:1.
S4	a double-waveguide fibre with a circular inner core of 0.15 NA and with 300ppm Nd^{3+} ions and a rectangular outer core of 0.4 NA and 80μm×30μm dimension; the fibre is coated with silicone rubber.

Appendix E The Table of Acronyms

Acronym	Description
CW	continuous wave
ESR	electron spin resonance
FWHM	full width at half maxima
IR	infrared
LP	linear polarised
MCVD	modified chemical vapour deposition
NA	numerical aperture
RE	rare earth
SH	second harmonic
SHG	second harmonic generation
TC	twin core
TE	transverse electronic (field)
TM	transverse magnetic (field)
TM	transition metal
UV	ultraviolet
WDM	wavelength division multiplexing
YAG	Yttrium Aluminium Garnet

Appendix F The Table of Variable Definitions

Var.	Chap.	Definition
a_p	2	transverse modal distribution of core p (p=1,2).
a_q	2	transverse modal distribution of q mode (q=e,o).
a_v	6	$(\alpha^2+\gamma^2)^{1/2}$.
A_{12}	3	spontaneous emission rate.
b	6	$1-U^2/V^2$.
b_p	2	$V_p e^{j\beta pz}$ for core p.
b_v	6	$a_v^2+k^2(n_{cl}^2-n_{metal}^2)$.
B_{12}	3	stimulated absorption rate.
B_{21}	3	stimulated emission rate.
B_{mn}	6	modal amplitudes in Fourier-Bessel series.
c	2	velocity of light in vacuum
c_{ext}	5	longitudinal acoustic wave velocity.
c_f	5	acoustic wave velocity.
d	2	core separation.
$d^{2\omega}$	6	nonlinear coefficient.
D	5	fibre diameter.
E	2	electric field.
E^{ω}	6	electric field at frequency ω.
$E^{2\omega}$	6	electric field at frequency 2ω.
E_{pm}	2	electric field of m-th mode over core p (p=1,2).
E_q	2	electric field of q mode (q=e,o).
f_a	5	acoustic frequency.
F	2	$1/(1+\beta_b^2/\kappa_a)^{1/2}$.
g	3	absorption line function.
I_s	3	threshold photon flux to bleach a two level system.

F_p	2	$1/(1+\sigma^2/4\kappa^p)^{1/2}$.
I_m	6	Bessel function.
J_m	6	Bessel function.
k	2	vacuum wave number.
k^ω	6	wave vector at angular frequency ω.
$k^{2\omega}$	6	wave vector at angular frequency 2ω.
k_p	2	perturbation vector
K_m	2	Bessel function.
K_i	6	u_i/n_i for TM wave, u_i for TE wave.
l	2	$[(\kappa_{ee}-\kappa_{oo})-j(\beta_e-\beta_o)]/2\kappa_x$.
L	6	fibre length.
n	2	real part of refractive index.
n_{cl}	2	cladding refractive index.
n_{co}	2	core refractive index.
n_{cop}	2	core refractive index of core p (p=1,2).
n_{eff}	6	effective refractive index.
n_i	6	refractive index of layer i.
N^p	3	photon flux.
N_p	3	population of level p.
O_m	6	overlap integral between SH and fundamental waves.
p_c	5	coupled power.
$P_{dc}^{(3)}$	6	$\chi^{(3)}E_\omega^{\,2}E_{2\omega}^{\,*}$.
P_{mn}	6	$2\int_0^\infty R_v\cosh(mg)\cosh(ng)e^{-2\gamma d\cosh(g)}dg$.
p_p	2,6	power in core p (p=1,2) or in polarisation p (p=x,y).
p_ω	6	power at angular frequency ω.
q	5	c_f^2/c_{ext}^2.
r_{ex}	6	extinction ratio.
R_v	6	$(a_v-b_v)/(a_v+b_v)$ for TE wave, $(a_v/n_{cl}^2-b_v/n_{metal}^2)/(a_v/n_{cl}^2+b^v/n_{metal}^2)$ for TM wave.
t	3	time.
t_i	6	thickness of layer i.
u_i	6	$k^2n_i^2-\beta^2$.
U	2	as normally defined in a fibre.
V	2	normalised wavelength in a fibre.

V_p	2	modal amplitude of 0-th mode over core
		p (p=1,2).
		modal amplitude of m-th mode over core
V_{pm}	2	p (p=1,2).
		modal amplitude of q mode (q=o,e).
V_q	2	as normally defined in a fibre.
W	2	beat length.
z_b	2	$(k^2 n_{co}^2-\beta^2)^{1/2}$.
α	6	power in polarisation p (p=x,y).
α_p	6	propagation constant.
β	6	average propagation constant.
β_a	2	$(\beta_1-\beta_2)/2$.
β_b	2	propagation constant of core p (p=1,2).
β_p	2	propagation constant of q mode (q=e,o).
β_q	2	$(\beta^2-k^2 n_{cl})^{1/2}$.
γ	6	gain coefficient.
δ	2	relative refractive index difference of
Δ	2	a TC fibre.
		relative refractive index difference of
Δ_0	2	an unperturbed TC fibre.
		perturbation strength of relative
Δ^p	2	refractive index.
		relative refractive index difference of
Δ_p	2	core p (p=1,2).
		$k^{2\omega}-2k^{\omega}$.
Δk	6	dielectric constant.
ϵ	6	dielectric constant in vacuum.
ϵ_0	6	complex refractive index.
η	2	2.
η_0	6	conversion efficiency in TC mode
η_c	5	coupling.
		1 for m>1.
η_m	6	conversion efficiency for SHG.
η_{shg}	6	$(\kappa_{12}\kappa_{21})^{1/2}$.
κ_a	2	$(\kappa_{oe}\kappa_{eo})^{1/2}/2$.
κ^p	2	coupling coefficient from core m to p
κ_{pm}	2	or from m mode to p mode in case where

		p,m=e,o.
$\kappa_{pm}^{(2)}$	2	higher order coupling coefficient from core m to p.
κ_x	2	$(\kappa_{oe}\kappa_{eo})^{1/2}$.
Λ	6	grating pitch.
λ	5	wavelength.
λ_0	5	central wavelength.
μ	6	magnetic constant.
σ	2	$\beta_e-\beta_o-\omega_p$.
ρ_p	2	core radius of core p.
υ	5	$(2\pi/z_b)(1-\lambda_0/\lambda)$.
χ	2	$n\chi$ is the imaginary part of the refractive index.
$\chi^{(2)}$	6	second order nonlinear susceptibility.
$\chi^{(3)}$	6	third order nonlinear susceptibility.
ω	6	angular frequency.

Appendix G The List of Publications

1. M.E. Fermann, L. Li, M.C. Farries, L.J. Poyntz-Wright, and L. Dong: ''Second-harmonic generation using gratings optically written by mode interference in poled optical fibres'', Optics Letters, **14**, 1989, pp.784-750.

2. C.D. Hussey, T.A. Birks, A.M. Wingfield, A. Niu, R. Kenny and L. Dong: ''Rectangular mode transformers in tapered single-mode fibres'', Electronic Letters, **25**, 1989, pp.1419-1420.

3. M.E. Fermann, P.J. Wells, L. Li and L. Dong: ''Phase-matched three-wave mixing in poled optical fibres'', OSA Topical Meeting on Photorefractive Material, effect and devices 2, Aussois, 1990.

4. H. Sabert, L. Dong and P.St.J Russell: ''In-line flexural wave optical modulator, filter and frequency shifter in dual-core fibre'', Topical Meeting on Integrated Photonic Research, Hilton Head, March, 1990.

5. H. Sabert, L. Dong and P.St.J. Russell: ''Versatile acousto-optical flexural wave modulator, filter and frequency shifter in dual-core fibre'', accepted by International Journal of Optoelectronics.

6. L. Dong, P.J. Wells, D.H. Hand and D.N. Payne: ''UV-induced refractive index change in Ce^{3+}-doped fibres'', Baltimore, May, 1991.

7. J.T. Lin, J. Kanka, L. Dong, D. McStay and A.J. Rogers: ''A simultaneously Q-switched and mode-locked fibre laser'', EQEC, Edinburgh, August, 1991.

8. L. Dong, M.H. Ober and P.St.J. Russell: "Dual-core fibre intermodal coupler by mechanically induced periodic microbending", submitted to Applied Optics and Opto-electronics Conference, Leeds, September 92.

9. L. Dong, P.J. Wells, D.P. Hand and D.N. Payne: "Photosensitivity in Ce^{3+}-doped optical fibres", submitted to Applied Optics.